

https://dspace.org/

Mine X (Portal C) jointed pillar numerical analysis

Chindedza, Tafadzwa

2018

https://hdl.handle.net/10539/25718

Chindedza, Tafadzwa (2018) Mine X (Portal C) jointed pillar numerical analysis, University of the Witwatersrand, Johannesburg, <http://hdl.handle.net/10539/25718>

Downloaded from a DSpace repository. https://dspace.org/



MSc (Eng.) RESEARCH REPORT

Mine X (Portal C) Jointed pillar numerical analysis

Name: Tafadzwa Chindedza

Student No: 582169

A research report submitted to the Faculty of Engineering and the Built Environment, University of the Witwatersrand, Johannesburg, in partial fulfilment of the requirements for the degree of Master of Science in Engineering.

Johannesburg, 2018

Declaration

I declare that this research report is my own unaided work. Where use has been made of work of others, it has been duly acknowledged. It is being submitted to the Degree of Masters of Science at the University of the Witwatersrand, Johannesburg. It has not been submitted before for any degree or examination in any other University.

……

(Signature)

…….. day of ……..., ……

at ……..

Abstract

Mine X is a platinum mine in Southern Africa, mining Platinum Group Elements using the room and pillar mining method. Mine X is currently mining four portals that were named Portal A, Portal B, Portal C and Portal D. A pillar run was experienced at Portal B and it was found necessary to revise the original pillar design for all of Mine X's portals. All portals at Mine X were originally designed using the Hedley and Grant (1972) pillar design formula. This research focuses on the numerical analysis on Mine X Portal C pillar design. The main objectives being to evaluate the effects of joints and pillar size on pillar strength and to evaluate the appropriateness of the original pillar design.

The Universal Distinct Element Code (UDEC) software was chosen to conduct the analysis as it allows for a relatively large number of joints to be incorporated, and also permits to model tensile fractures. Propagation of tensile fractures is a key aspect of the pillar failure process in the model and reality alike. Therefore, significant effort has gone towards reproducing and calibrating this process based primarily on results of laboratory tests conducted on actual rock specimens collated at Portal C.

Since the type of modelling carried out in this project is relatively new in rock engineering, a review of the literature was deemed important. A study of existing approaches towards room and pillar designs was conducted so as to understand the mine's expectation from its original pillar design. Similar work previously done by others was studied and an optimum approach to follow was decided upon.

Data was collected from the mine that included test results on specimens, mapping data and pictures showing existing underground conditions. Previous work done on Mine X was also reviewed from which core logging data was obtained. All the collected raw data was processed to come up with information that could be used as inputs into the numerical models. It was decided to model the micro particles of the rock as voronoi tessellation and the cementation between these particles were modelled as voronoi contacts. Voronoi tessellation was essential to model tensile fracturing. Calibration against laboratory results was carried out for the purpose of obtaining voronoi properties that could be used in the model. It was decided to represent the joint network using Discrete Fracture Network (DFN - a statistical description of fractures where a set of statistical parameters are defined and a joint set is generated based on those statistics) instead of explicitly modelling the mapped structures. The modelling

process conducted in UDEC required some sensitivity analyses to be done to evaluate the effect of parameters such as velocity and mechanical damping.

Three sets of models were run, each set run on three different pillar sizes (2 m, 4 m and 6 m pillar widths). The first set was modelled as an intact pillar and the other two sets were modelled as jointed pillars. Each of the last two sets had a jointing network representing one of the two different geotechnical domains at the portal. The results from these models were compared.

The modelling results showed that pillar strength increases with increase in pillar size. Stiffness also increase as pillar width increases. However, a discrepancy was observed on the intact pillars where the 2 m pillar proved to be stiffer than the 4 m pillar. The existence of joints reduces intact pillar strength by 70% to 80%. The existence of the low angle joint sets translates into less stiff, more flexible and more ductile pillars.

Mine X is currently mining 4 m square pillars. According to the numerical modelling carried out, these pillars are too small with strengths ranging between 55 and 65 MPa. From the Hedley and Grant (1972) fomula used for the original pillar design, the mine is expecting pillars with average pillar strength of at least 95 MPa from the 4 m pillars. There is need for revising the design criteria and adjusting the mined pillar sizes to about 8 m wide pillars.

Dedications

This project is dedicated to my daughter Zoey. I wish she could be here to celebrate the results with me.

Acknowledgements

I would like to recognize and thank the following people and institutions for their valuable guidance and contributions towards this research:

Professor Halil Yilmaz for the expert supervision and guidance.

Mr Joseph Mbenza Muaka from SRK Consulting for his mentoring and guidance throughout the research.

Ms Jeanne Walls from SRK Consulting for her support and facilitation of the project.

The rock engineering personnel and management of the mine for allowing the use of the mine data for the completion of the project.

My family and friends for the support and encouragement throughout the research.

Table of Contents

Contents **Page**

List of Figures viii

List of tables x

Chapter 1 : Introduction 1

1.1. Project background 1

1.2. Mine background 1

1.3. Project justification 3

1.4. Aim 3

1.5. Modelling approach 3

1.6. Methodology 4

1.7. Report structure 6

Chapter 2 : Literature Review 8

2.1. General hard rock pillar behaviour 8

2.2. Empirical pillar design 11

2.2.1. Confinement formula 15

2.2.2. Hedley and Grant pillar formula 16

2.2.3. Pillar strength expected for Mine X pillar design 17

2.2.4. Limitations of the empirical formulae 17

2.3. Distinct Element Method (DEM) and Universal Distinct Element Code (UDEC) 18

2.4. Jointed pillar modelling using DEM 18

Chapter 3 : Data collection and UDEC Modelling 21

3.1. Data collection 21

3.1.1. Structural mapping 21

3.1.2. Core logging 22

3.1.3. Laboratory testing results 28

3.1.4. Previous reports 31
3.1.5. Underground observations 31
3.2. DFN model construction 34
3.2.1. Fracture orientation 35
3.2.2. Fracture size distribution 36
3.2.3. Fracture position distribution 38
3.2.4. Migration from 3 dimension DFN to 2 dimension DFN 39
3.3. UDEC Modelling 39
3.3.1. Pillar model Geometry 39
3.3.2. Loading rate 42
3.3.3. Mechanical Damping 44
3.4. Input material parameters 47
3.4.1. Intact rock calibration 47
3.4.2. Joint material properties 48
3.5. Summary 49
Chapter 4 : Results and analysis 50
4.1. Results 50
4.1.1. Intact pillar models 50
4.1.2. Jointed pillar model DFN 1 59
4.1.3. Jointed pillar model DFN 2 66
4.2. Results analysis 71
4.3. Summary 76
Chapter 5 : Conclusions and recommendations 77
Chapter 6 : References 81

List of Figures

Figure 1: Schematic diagram showing room and pillar mining at Mine X.....2

Figure 2: UDEC 4m pillar model.....6

Figure 3: Principal modes of deformation behaviour of mine pillars (Brady and Brown 2004). 9

Figure 4: Schematic illustration of the evolution of fracture and failure in a pillar in massive rock (Lunder & Pakalnis, 1997).....10

Figure 5: Pillar rating system (Roberts, et al., 1998).....10

Figure 6: Empirical pillar strength formulas normalized to UCS (after Martin and Maybee, 2000).....14

Figure 7: Empirical pillar strength formulae 17

Figure 8: Fracture orientation in domain 1 and domain 2 (Mine X, 2016) 22

Figure 9: Cumulative frequency curve of Q values.....24

Figure 10: Cumulative frequency curve for RMR values.....26

Figure 11: Summary of rock testing programs.....29

Figure 12: Distribution of peak friction angle in BFA and SHJO tests.....30

Figure 13: Existing low angle joints with infilling.....32

Figure 14: Fall of ground at the top of switchback 1 33

Figure 15: Shotcrete failure against the sidewalls.....33

Figure 16: Pillar sidewall conditions with stress induced tensile fractures and joint mobilization with the pillar.....34

Figure 17: Stereonet plot of fractures mapped at Portal C (DIPS software) 35

Figure 18: DFN 1 and DFN 2 models.....36

Figure 19: Effect of α on fracture size distribution for a=2.5.....38

Figure 20: the 3D DFN model in 3DEC.....38

Figure 21: DFN domain and pillar region settings for P_C model in 3DEC, isometric view on the left and plane view on the right.....39

Figure 22: Typical Mine X jointed pillar model geometry – Dimensions and boundary conditions.....40

Figure 23: UDEC model of Mine X jointed pillar. (a) Pre-existing fractures and voronoi tessellation, (b) Typical mesh/grid.....42

Figure 24: Loading velocity sensitivity: Average pillar stress vs. pillar strain curve.....43

Figure 25: Loading velocity sensitivity: Unbalanced force.....44

Figure 26: Damping sensitivity analysis: Average pillar stress vs. pillar strain curve.....46

Figure 27: Average pillar stress versus axial displacement curve for the intact 4 m pillar.....51

Figure 28: Average pillar stress versus axial displacement curve and failure mode for the intact 4 m pillar.....51

Figure 29: Average pillar stress versus axial displacement curve and displacement contours for the intact 4 m pillar.....52

Figure 30: Average pillar stress versus axial displacement curve for the intact 2 m pillar.....54

Figure 31: Average pillar stress versus axial displacement curve and failure mode for a 2 m intact pillar.....54

Figure 32: Average pillar stress versus axial displacement curve and displacement contours for the intact 2 m pillar.....55

Figure 33: Average pillar stress versus axial displacement curve progression of stress for the intact 2 m pillar.....56

Figure 34: Average pillar stress versus axial displacement curve for the intact 6 m pillar.....57

Figure 35: Average pillar stress versus axial displacement curve and failure mode for the intact 6 m pillar.....58

Figure 36: Average pillar stress versus axial displacement curve and displacement contours for the intact 6 m pillar.....58

Figure 37: Average pillar stress versus axial displacement curve and displacement contours for the intact 6 m pillar.....59

Figure 38: Average pillar stress versus axial displacement curve and associated failure mechanism for 2m wide pillar model for DFN 1.....60

Figure 39: Progression of stress for 2m wide jointed pillar model for DFN 1.....60

Figure 40: Progression of total displacement for 2m wide jointed pillar model for DFN 1....61

Figure 41: Average pillar stress versus axial displacement curve and associated failure mechanism for 4 m pillar for DFN 1.....62

Figure 42: Progression of stresses for 4 m wide jointed pillar model for DFN 1.....63

Figure 43: Progression of total displacement for 4 m wide jointed pillar model for DFN 1...63

Figure 44: Average pillar stress versus axial displacement curve and associated failure mechanism for 6 m pillar for DFN 1 64

Figure 45: Progression of stresses for 6 m wide jointed pillar model for DFN 1.....65

Figure 46: Progression of total displacement for 6 m wide jointed pillar model for DFN 1...65

Figure 47: Average pillar stress versus axial displacement curve and associated failure mechanism for 2 m pillar for DFN 2 66

Figure 48: Progression of stresses for 2 m wide jointed pillar model for DFN 2.....67

Figure 49: Progression of total displacement for 2 m wide jointed pillar model for DFN 2...67

Figure 50: Average pillar stress versus axial displacement curve and associated failure mechanism for 4 m pillar for DFN 2 68

Figure 51: Progression of stresses for 4 m wide jointed pillar model for DFN 2.....69

Figure 52: Progression of total displacement for 4 m wide jointed pillar model for DFN 2...69

Figure 53: Average pillar stress versus axial displacement curve and associated failure mechanism for 6 m pillar for DFN 2 70

Figure 54: Progression of stresses for 6 m wide jointed pillar model for DFN 2.....71

Figure 55: Progression of total displacement for 6 m wide jointed pillar model for DFN 2...71

Figure 56: Average pillar stress versus axial displacement curve for intact pillars and jointed pillars results in the background 72

Figure 57: Average pillar stress versus axial displacement for DFN 1 and DFN 2 results in the background.....73

Figure 58: Pillar stress vs. axial displacement graphs of 2 m pillar models for DFN 1 with DFN 2 results in the background 74

Figure 59: Pillar stress vs. axial displacement graphs of 4 m pillar models for DFN 1 with DFN 2 results in the background 75

Figure 60: Pillar stress vs. axial displacement graphs of 6 m pillar model for DFN 1 with DFN 2 results in the background 76

List of tables

Table 1: Intact rock material parameters, pre-mining stress state and joint properties (SRK Report No. 480443, 2015) 2

Table 2: Summary of empirical strength formula for hard rock pillars (Martin & Maybee, 2000) 13

Table 3: Hedley and Grant (1972) constants. 16

Table 4: Rock mass quality (RMR converted from Q) 24

Table 5: Rock mass quality (Q) 25

Table 6: Composited Rock Mass Quality (Laubscher (1990)'s RMR values) 27

Table 7: GSI Results 28

Table 8: Summary of BFA and SHJO test results 30

Table 9: Summary of identified joint sets in terms of dip, dip direction and Fisher's coefficient K 36

Table 10: Voronoi contact parameters 48

Table 11: Steel ring platens and voronoi block material parameters 48

Table 12: Joint mean strength properties 49

Table 13: Failure mechanisms 53

Table 14: The average pillar strengths for DFN 1 and DFN 2 relative to the intact pillar 79

Chapter 1 : Introduction

1.1. Project background

A platinum mine in Southern Africa that will here be referred to as Mine X experienced a pillar run at one of its portals (Portal B (P_B). Following this event, an investigation was conducted on the effect of local geotechnical conditions, in particular a clay filled shear zone on the stability of pillars as these effects were not taken into account in the original pillar design. It was recognized that the presence of the shear structure had a complex effect on the stability of the pillars hence non-linear numerical modelling was essential to carry out the investigation.

The work done by SRK Consulting in the numerical analysis of P_B involves the use of sophisticated numerical modelling. This work triggered the need to do a similar analysis on the Portal C (P_C) pillar design improving on some areas that could not be thoroughly investigated when the P_B project was carried out. However, at P_C, there is no evidence of the clay filled shear intersecting the orebody, hanging-wall or footwall hence analysis was just carried out to investigate the effect of the joints on pillar stability. There is still room for further investigation on how best this numerical analysis approach can be optimally used.

1.2. Mine background

The ore body mined at Mine X is an elongated saucer shaped lapolith, which is a flat and synclinal structure. The main lithology of the ore body is gabronorite, websterite and bronzitite. A mafic pegmatite invariably occurs at the transitional zone between websterite and gabronorite. Mineralization of the deposit consists of Base metals and Platinum Group Elements (PGEs). The region of economic concentration of PGE is known as the Base of Main Sulphide Zone (BMSZ) located just below the Websterite-Bronzitite contact (SRK Report No. 482668, 2014). The BMSZ is used as the reference zone for determining the cut-off grade giving an average mining height of 2.5 m.

Table 1 summarizes the intact rock material properties, pre-mining stress gradient and joint properties at P_C. The intact material properties were obtained from laboratory tests carried out by a commercial rock testing laboratory. The virgin state of stress was determined using the overburden rock density of 3200 kg/m^3 and a horizontal to vertical stress (k) ratio of one. Joint

properties were derived from fitting a curve to a Barton-Bandis joint model, which includes the core logging joint information and scaling of the Joint Wall Compressive Strength (JCS) and Joint Roughness Coefficient (JRC). This resulted in equivalent Mohr-Coulomb properties for the joint of 2.5 MPa and 26° for the apparent joint cohesion and friction angle, respectively.

Table 1: Intact rock material parameters, pre-mining stress state and joint properties (SRK Report No. 480443, 2015)

Intact rock properties			Virgin state of stress			Joint properties	
Young's modulus E (GPa)	**Poisson's ratio**	**UCS (MPa)**	**S_{xx} (MPa/m)**	**S_{yy} (MPa/m)**	**S_{zz} (MPa/m)**	**Cohesion (MPa)**	**Friction angle (°)**
150	0.23	200	0.032	0.032	0.032	2.5	26

Mine X underground mine is a fully mechanized trackless operation employing the room and pillar mining method with full face slicing as shown in Figure 1. The mine is at a relatively shallow depth ranging between 200m and 260m below surface with an average mining height of 2.5m for the production panels and 3.2m for the development panels. The ore is mined in one slice on the face with an extraction ratio of 85%. The mine practices 100% on-reef mining using trackless machinery for drilling, support, loading, hauling and transportation. The mining method involves the establishment of several production areas hence high utilization of both men and machinery.

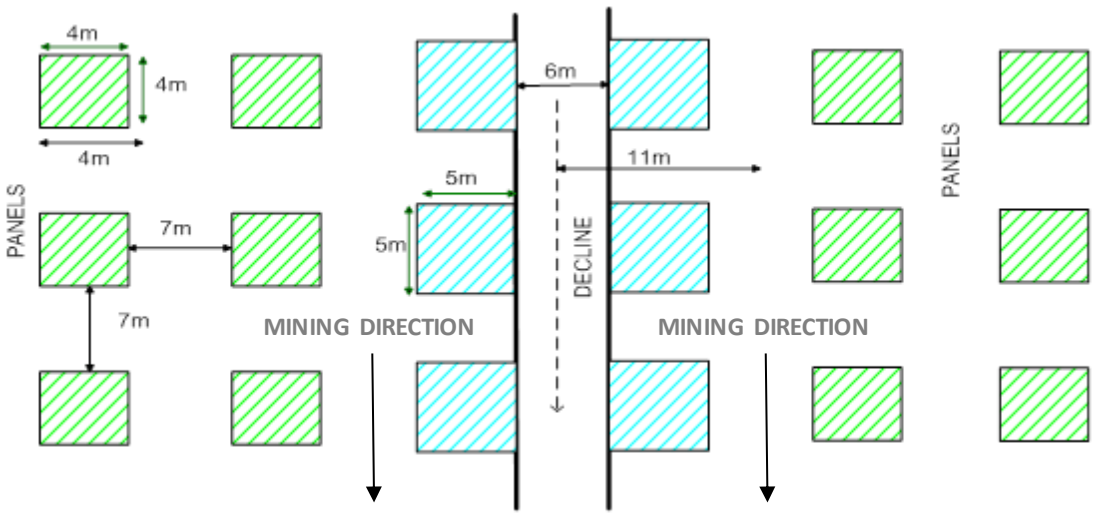


Figure 1: Schematic diagram showing room and pillar mining at Mine X

1.3. Project justification

In July 2014, sections of P_B collapsed affecting the access on the decline and lower levels. The Falls of Ground (FoG) were interpreted as resulting from overloading and inherent structural defects in the rock mass (SRK Report 482668). The failure started on the lower levels and progressed passing through the decline to the upper levels and cracks were observed on the surface above the failed region. This pillar failure suggests a shortfall in the original pillar design and hence the need for this research on the P_C pillar design. The original pillar design could have shortfalls because of the following reasons:

a. The estimation of pillar strength has been a subject of much research in the mining industry (Esterhuizen, 1998, Esterhuizen, 2014, Martin and Maybee, 2000, Lunder, 1994, Roberts, et al. 2005) and there is still room for further research in this regard. The statistical methods for the estimation of the pillar strength were considered for the estimation of the strength factor *K* and the constants α and β. Very few mines where pillar failures have occurred have been documented on the mines along the location of Mine X and the data is inadequate to develop a statistically based pillar strength equation reliably.
b. Mine X is at a relatively shallow depth hence pillar strength is expected to be affected by geological structures (Hoek, et al., 2002). The geological structures, especially the presence of the shear fracture was not exclusively considered in the original pillar design.

1.4. Aim

The main aim of the project is to do a non-linear numerical analysis on Mine X P_C pillar design using UDEC in order to:

- Analyse the effects of joints on pillar strength.
- Evaluate the effect of pillar size in a particular geotechnical domain.
- Evaluate the appropriateness of the original pillar design for Mine X P_C.

1.5. Modelling approach

The rock mass jointing network was simulated using discrete fracture network (DFN). DFNs are a stochastic representation of the jointing network where a set of statistical parameters are

defined and a joint set is generated based on the input statistical distributions. The input statistical distributions are calculated from the structural data obtained from a mapping exercise conducted on the mine. The concept of DFN requires use of multiple DFNs to obtain reliable results. However due to time constraints and the required run time of up to 48 hours for each model, a limited number of DFNs are analysed.

Two-dimensional modelling was carried out with the Universal Distinct Element Code (UDEC). The three dimensional version of the code (3DEC) was used only to generate DFNs that were subsequently imported into the 2D code. Both software programs are based on the numerical method known as distinct element method (DEM).

For improving the quality of the numerical model results, the intact rock in the pillars was represented as an assemblage of smaller irregular cells referred to as voronoi tessellation. Voronoi tessellation is a form of numerical analysis called bonded particle modelling (BPM) where material is modelled as an assemblage of irregular particles connected by contacts (Kazerani and Zhao, 2010), which enables realistic modelling of cracking and the effects of fractures on pillar strength.

UDEC models each of the intact rock blocks as separate discrete elements. The elements are then further divided into a number of triangular finite difference zones (Itasca Consulting Group, Inc., 2006). The mechanical response of the rock mass is simulated as a combination of intact rock deformations and slip along joints using the voronoi tessellations.

1.6. Methodology

The research project followed the following stages

1. Desktop study

   Since the use of DFNs in modelling jointed pillars combined with the use of bonded particle modelling is relatively new in the field of Rock Engineering, an extensive desktop study was carried out to identify key areas that need significant attention.

2. Collection of data

   The information that was put together in preparation for the numerical modelling includes the structural mapping data, joint and rock material properties, laboratory

testing results and the underground observations. Where necessary, reasonable assumptions were made based on the information available for PB.

3. Processing of mapped data

   Mapped data was processed using the DIPS software. The processed information from DIPS was used for the construction of the three dimensional DFNs in 3DEC.

4. UDEC Model calibration

   As the microscopic properties of the rock was modelled using voronoi tessellation, the microscopic properties (strength and deformation) assigned to the contacts of the voronoi cells were calibrated against the macroscopic responses of the rock measured in the lab. The parameters that required calibrated at the contacts are as follows:

   - Normal stiffness
   - Normal to shear stiffness ratio
   - Peak cohesion
   - Residual cohesion
   - Peak tensile strength
   - Residual tensile strength
   - Peak friction angle
   - Residual friction angle

5. UDEC model construction and analysis

   A two dimensional model was created and analysed using UDEC. The model was constructed similar to the uniaxial compressive test in the lab with two steel platens at the top and bottom of the specimen as illustrated in Figure 2. The load was applied as constant velocity of 0.01 m/s at the top platen and the bottom platen being fixed in the x and y direction.

   The calibrated properties were assigned to the voronoi contacts. The voronoi blocks were modelled as elastic. Therefore, only the density, Young's modulus and Poisson's ratio, directly measured in the lab were specified. The three dimensional DFN created in 3DEC was imported into UDEC as a "slice" cut through the three-dimensional solid. The joint properties obtained from processing the geotechnical logging data was assigned to the joints.

The obtained results are then analysed.

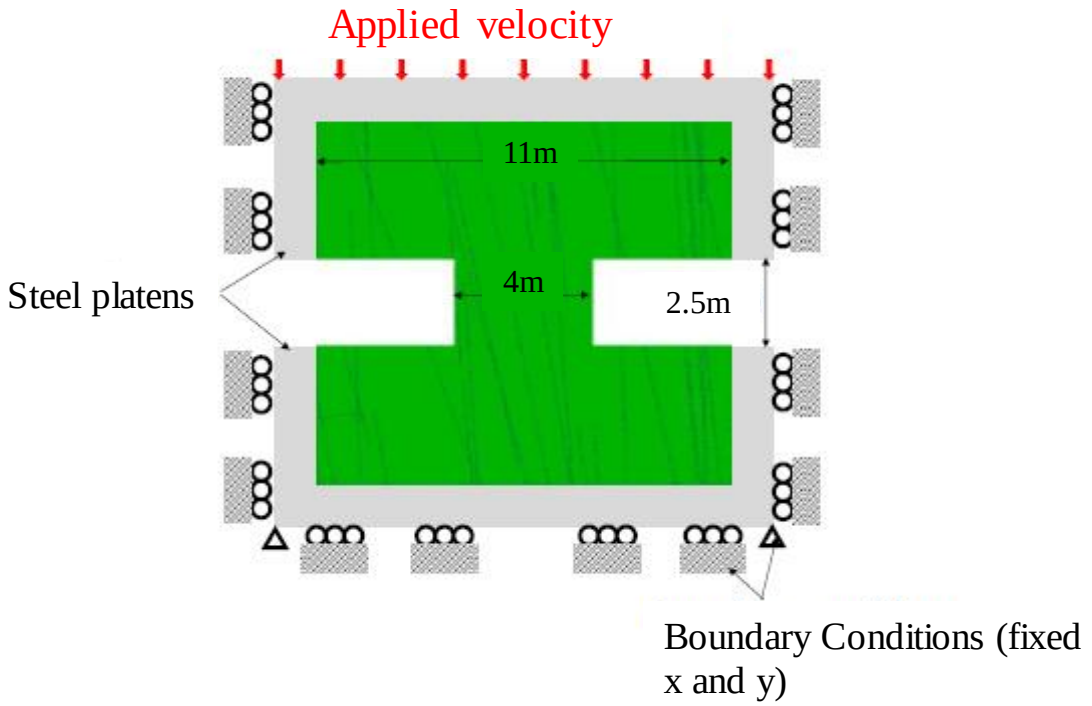


Figure 2: UDEC 4m pillar model

1.7. Report structure

This report follows the following structure

Chapter 1: Introduction

Here the project is introduced with the following outlined:

- Project background
- Mine background
- Project justification
- Main aim of the project
- Modelling approach and,
- Methodology used

Chapter 2: Literature review

A desktop study was conducted for the purpose of understanding the previous work done by scholars on similar subjects and firming up on the principles to be used in the numerical modelling approach.

Chapter 3: Data collection and UDEC modelling

Data was collected from the mine, processed and used as inputs into the UDEC model. The modelling process is also explained in this chapter.

Chapter 4: Results and analysis

The results obtained from the modelling exercise are outlined and analysed.

Chapter 5: Conclusions and recommendations

Chapter 5 concludes the report and summaries appropriate recommendations for further work.

Chapter 6: References

Chapter 2: Literature Review

2.1. General hard rock pillar behaviour

Several factors that include, rock formation, geological structures, pillar size and in situ stress conditions control failure mode of hard rock pillars (Brady & Brown, 2004). Hoek, et al. (2002) suggests failure modes for underground tunnels that can be considered suitable for hard rock pillar failure. At relatively low in situ stress, failure is controlled by pre-existing fractures that form unstable blocks that fail by sliding along the discontinuities. However, as in situ stress increases with increase in mining depth, failure becomes less controlled by structures and more and more stress controlled with fractures oriented in the direction of the major horizontal stress (Hoek, et al., 2002). Pillars under stress exhibit five main behaviour modes described by Brady and Brown (2004) as, “

a) In massive rock, excessive spalling leading to necking of the pillar is the most obvious sign that the ultimate pillar strength is almost reached (Figure 3 (a)).
b) In highly jointed orebody, pillars with low width to height ratio, one shear fracture may split the entire pillar at an angle. Pillar failure is dictated by this fracture consequently dictating the overall strength of the pillar (Figure 3(b)).
c) When soft partings are present at the contacts of the pillar and the surrounding strata, internal splitting can be promoted by yielding which manifest by bulging without necessarily leading to spalling. (Figure 3 (c)).
d) In a geological environment where an inclined joint is persistent, the yielding of the pillar is dependent on the angle of inclination of the persistent joint. If the persistent joint is at an angle of inclination greater than the angle of friction of the rock, the pillar may yield (Figure 3 (d)). The amount of slip on the discontinuities necessary to produce yield and subsequent relaxation of the elastic state of stress within the pillar, needs only to be of elastic orders of magnitude resulting in a non-destructive form of yielding. The pillar can appear stable as long as the hanging-wall is competent although it is unable to carry extra load.
e) Figure 3 (e) shows a situation where a well-defined foliation or schistosity parallel to the principal orientation of loading exist. In such cases, the pillars can fail in buckling or kink band mode with the spacing of the joint set and height being the key factors allowing buckling to take place.”

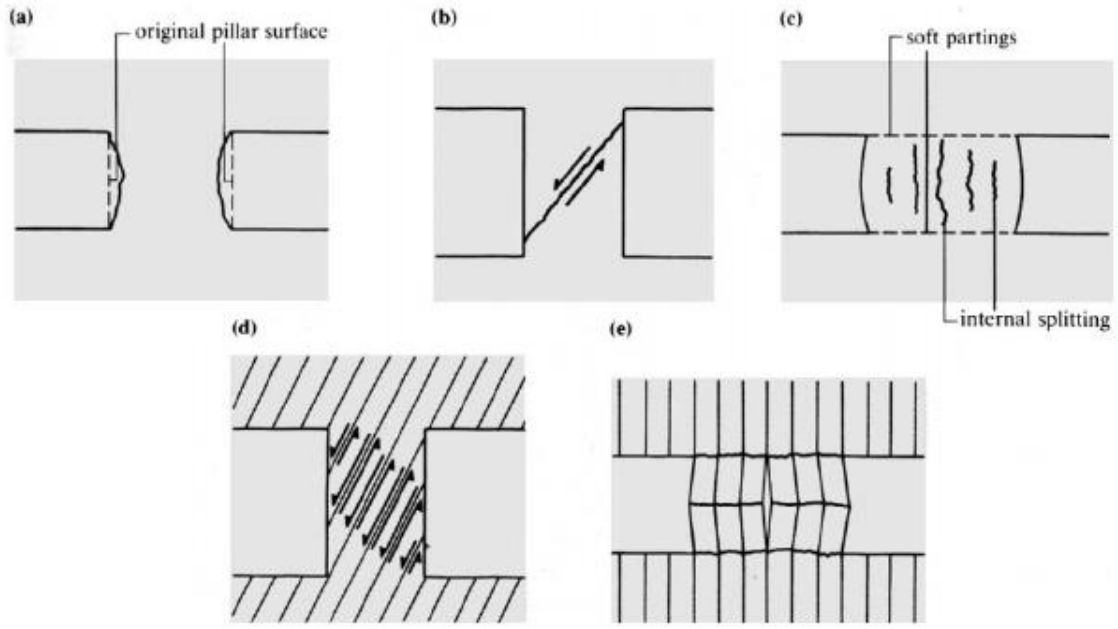


Figure 3: Principal modes of deformation behaviour of mine pillars (Brady and Brown 2004).

Considering Brady and Brown (2004) pillar failure behavior mode and the current geotechnical conditions at P_C, if any failure is to happen, it is expected to be as in Figure 3 a), b) or d). The obtained results from the numerical models in this study are compared to Brady and Brown (2004)'s theory for correlation.

Lunder and Pakalnis (1997) describe degradation of pillars in a massive rock as illustrated in Figure 4. From a stable pillar to its failure, the progression is as follows:

a) Stable pillar
b) Local shear failure evidenced by cracking at the pillar corners.
c) With increased load, surfaces begin to spall indicating crack initiation stage. At this point, the pillar is partially failed but is still capable of carrying additional load.
d) Higher stress state lead to damage accumulation through internal crack initiation and growth and interaction of the networks of cracks.
e) When friction between newly developed cracks is fully mobilized, the pillar is most probably at peak strength.

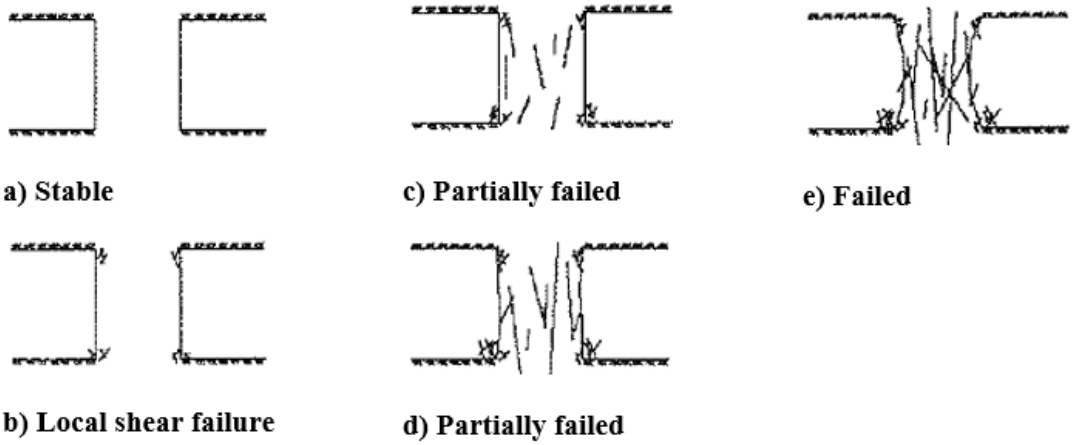


Figure 4: Schematic illustration of the evolution of fracture and failure in a pillar in massive rock (Lunder & Pakalnis, 1997)

Roberts, et al. (1998) developed a 6-stage pillar rating system to describe progressive stress-induced pillar failures as illustrated in Figure 5.

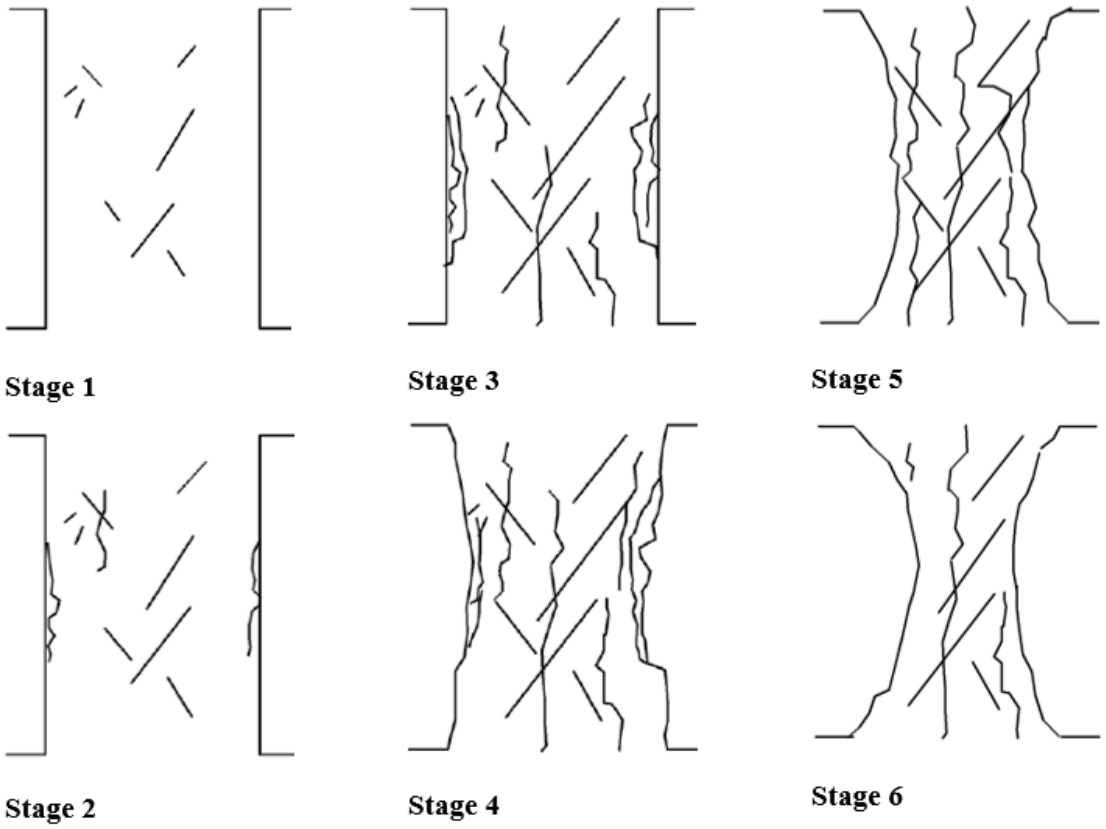


Figure 5: Pillar rating system (Roberts, et al., 1998)

The pillar failure under stress propagates through the following stages until an hourglass form of shape is formed (Roberts, et al., 1998):

- Stage 1 - Intact pillar
- Stage 2 - Minor spalling and short axial fractures
- Stage 3 - Substantial spalling, axial fracture length shorter than the half pillar height
- Stage 4 - Continuous open fractures cutting towards pillar core. Beginning of formation of the hourglass shape.
- Stage 5 - Large continuous open fractures, well developed hour-glass shape.
- Stage 6 - Failed pillar by either extreme hour-glass shape or necking

Theories by Lunder and Pakalnis (1997) and Roberts, et al. (1998) follow similar failure progression modes. However, Roberts, et al. (1998) go further to indicate the hour glass shape failure that is not explicitly shown by Lunder and Pakalnis (1997). Roberts, et al. (1998) commend on the progression of spalling as failure progresses whilst Lunder and Pakalnis (1997) mention spalling as an indicator of the crack initiation stage.

Mine X is a relatively shallow mine hence rock failure is expected to be structurally oriented. Underground observations indicate stress induced tensile fractures similar to Figure 4 c) and Figure 5 stage 3 failure modes.

2.2. Empirical pillar design

Room and pillar mining layouts in underground mining are usually designed using the Factor of Safety (FoS) approach. The FoS is defined as the ratio of the pillar strength to the pillar stress as in equation 1. Pillar strength should be higher than the load being exerted on the pillar to maintain stability therefore FoS is usually designed to be greater than one except in cases where the pillars are designed to yield.

$$FoS = \frac{Pillar\ Strength}{Average\ Pillar\ Stress\ (APS)} \quad \textbf{(1)}$$

Where:

$$APS = \frac{\rho g h}{1 - e} \quad \textbf{(2)}$$

Where:

ρ is the density of the rock mass

g is gravitational acceleration

h is the floor depth of excavation below ground

e is the extraction ratio

Following Salamon and Munro (1967) coal-pillar strength formula, there have been several attempts to establish hard-rock pillar strength formulae using the back analysis approach. The back analysis approach involves the analysis of failed and stable pillars to come up with pillar strength formulae. The analysis conditions for each empirical method in terms of number of pillars analysed and rock mass type and strength differ from one method to the next. The pillar strength formulae obtained by different researchers are tabulated in Table 2, where (W) is the width and (H) is the height of the pillar in metres.

Table 2: Summary of empirical strength formula for hard rock pillars (Martin & Maybee, 2000)

Researcher	Pillar strength formulas	UCS (MPa)	Rock Mass	No of pillars
Hedley and Grant	$133\frac{{W_{eff}}^{0.5}}{H^{0.75}}$	230	Quartzite	28
Von Kimmelmann	$65\frac{W_{eff}^{0.46}}{H^{0.66}}$	94	Metasediments	57
Krauland and Soder	$35.4\left(0.78+0.222\frac{W_{eff}}{H}\right)$	100	Limestone	14
Potvin, et al.	$0.42\partial_c\frac{W}{H}$	-	Canadian Shield	23
Sjoberg	$74\left(0.778+0.222\frac{W}{H}\right)$	240	Limestone/Skarn	9
Lunder and Pakalnis	$0.44\partial_c(0.68+0.52K)$	-	Hard rocks	178

The formulae in Table 2 all show the dependency of pillar strength on the geometry of the pillar i.e. its width (W) to height (H) ratio.

Where:

W is pillar width

H is pillar height

∂_c is laboratory UCS of the rock

K is the Lunder and Palkanis pillar friction term (defined by equation (6))

For non-square pillars the width is taken to be the effective width (W_{eff}) calculated from the formula:

$$W_{eff}(m) = 4\left(\frac{Area\ (m^2)}{Circumference\ (m)}\right) \quad \textbf{(3)}$$

Figure 6 shows the predicted pillar strength from the various formulae in Table 2 using a pillar height of 2.5m. The pillar strengths in Figure 6 have been normalised to the laboratory UCS

to enable use in various rock strength conditions. The pillar strength normalisation was calculated using the equation:

$$\frac{Pillar\ strength\ (MPa)}{UCS\ (MPa)} \quad \textbf{(4)}$$

Where UCS is the laboratory rock strength where the specific analysis was carried out.

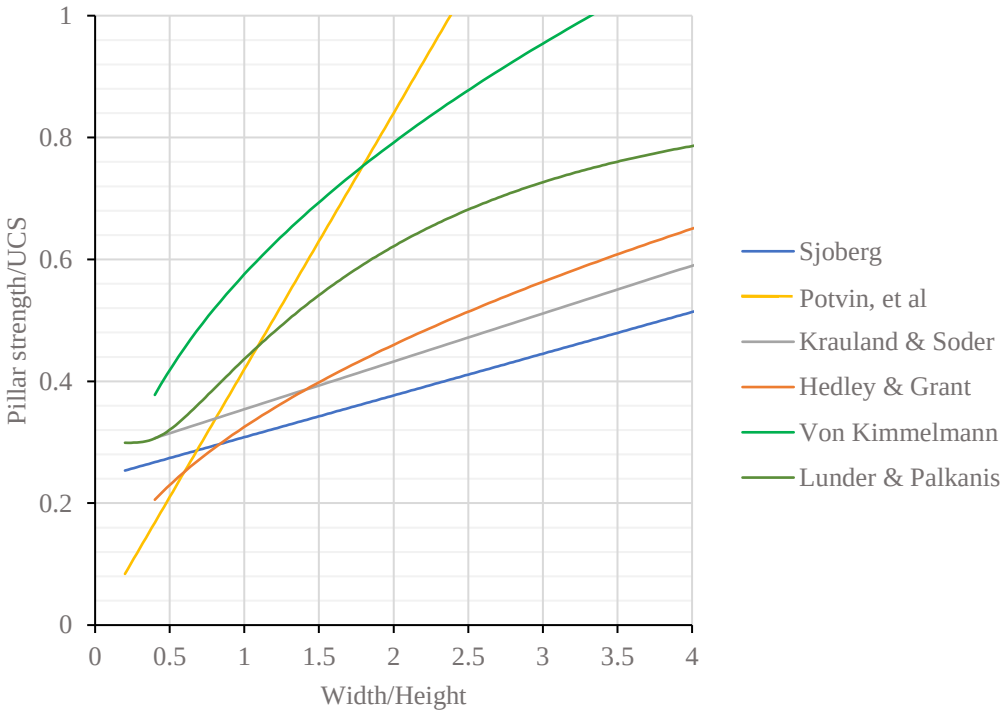


Figure 6: Empirical pillar strength formulas normalized to UCS (after Martin and Maybee, 2000)

Hedley and Grant and Von Kimmelmann's formulae follow Salamon and Munro (1967) that suggests the coal pillar strength could be determined using the power fomula:

$$\sigma_p = K\frac{W^{\alpha}}{H^{\beta}} \quad \textbf{(5)}$$

Where:

σ_p (MPa) is the pillar strength,

K (MPa) is the strength of a unit volume of coal,

α and β are constants calibrated in relation to the geomechanical conditions of the rock mass,

W and H are the pillar width and height in metres, respectively.

Krauland and Soder and Sjoberg add a constant to the power formula keeping both α and β equal to one. Potvin, et al. multiply the power formula with a factor and keep α and β equal to one. Potvin, et al's approach result in a relatively steep gradient of the pillar strength formula graph.

In all cases except by that by Lunder and Pakalnis (1997), the effect of the minor principle stress is ignored and the pillar strength fomulae rely on the stress to strength ratio based on the maximum pillar stress and the UCS. Although Lunder and Pakalnis (1997) attempt to include the effect of the minor principle stress through the use of their parameter K, their fomula predicts similar strengths as all other formulae in Table 2.

2.2.1. Confinement formula

Lunder and Pakalnis (1997) did an analysis on published pillar case histories to come up with the pillar strength formula which they termed the confinement formula. The confinement formula utilised a database of different cases of stable, unstable and failed pillars in different environments. Not all other formulas except that by Lunder and Pakalnis (1997) take into account the effect of the confining stress on pillar strength. The confinement formula attempts to take into account the effect of confining stress on the strength of the pillar using the K factor. K is the pillar friction term, calculated as

$$K = tan\left(\cos^{-1}\frac{1 - C_{pav}}{1 + C_{pav}}\right) \quad \textbf{(6)}$$

Where C_{pav} is the average pillar confinement given by

$$C_{pav} = 0.46\left[log\left(\frac{W}{H} + 0.75\right)\right]^{\frac{1.4}{(W/H)}} \quad \textbf{(7)}$$

The average pillar confinement was derived after a two dimensional boundary element method was conducted to determine the relationship between pillar width to height ratio and the average pillar confinement. The pillar width and height can be acquired readily where pillars are rectangular or square. However, when pillars are irregular or confined in one or more sides the effective pillar dimensions are difficult to access. Using the average pillar confinement allows for a correct assessment of the shape term in the pillar strength (Lunder & Pakalnis, 1997).

2.2.2. Hedley and Grant pillar formula

The Hedley and Grant (1972) power formula was used to estimate pillar strength for all mines at Mine X. As mentioned earlier, the Hedley and Grant (1972) power formula was developed following Salamon and Munro (1967) recommendation. Hedley and Grant (1972) back analysed the behaviour of some uranium pillars in Canada and came up with the values tabulated in Table 3 to fit into the Salamon and Munro (1967)'s power formula

Table 3: Hedley and Grant (1972) constants.

K (MPa)	α	β
133	0.5	0.75

The Hedley and Grant (1972) formula has been used for many years in the design of South African platinum and chrome mines. Few collapses have been reported for layouts designed using this formula (Malan & Napier, 2011) suggesting that in some cases it yields estimates that are desirable even if it was developed in a different geotechnical environment.

When doing a pillar design, it should always be taken into consideration that the Hedley and Grant (1972) constants were derived for a different setting and geotechnical environment. Malan and Napier (2011) conclude that neither the empirical formula nor numerical analysis can be used solely for pillar design. It is therefore recommended that both techniques be used to come up with a conclusive design. Some researchers have however suggested that following an engineering design approach to come up with a pillar design is more appropriate instead of depending entirely on just the numerical or empirical design results (Swart, et al., 2005).

2.2.3. Pillar strength expected for Mine X pillar design

The UCS of the rock mass multiplies the normalized pillar formulae to determine the pillar strengths expected for that particular case. Figure 7 is a graph showing the projected pillar strengths for given width to height ratios at a UCS of 237 MPa (Mine X rock UCS). From these empirical formulae, a 4 m wide, 2.5 m in height pillar is expected to have a strength between 80 MPa and 170 MPa. However, in view of the confining stress formula which takes into account the confining stress and is generalised for multiple hard rock mining environments, the Mine X pillar strength is expected to be about 130 MPa. Considering the Hedley and Grant pillar formula that was used for pillar design at the mine, the Mine X pillar is expected to have a pillar strength of about 95 to 100 MPa. A deduction can be made to say that since the Hedley and Grant pillar formula was used, for the factor of safety required at Mine X, mined pillars should have a strength of at least 95 MPa.

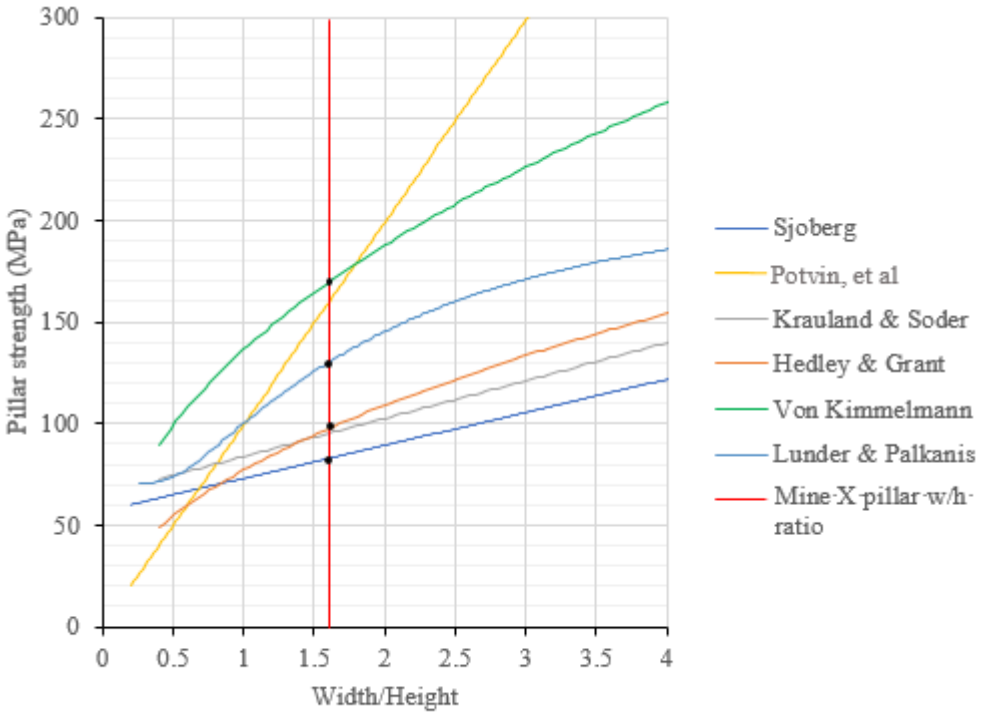


Figure 7: Empirical pillar strength formulae

2.2.4. Limitations of the empirical formulae

It should be noted that, although empirical methods are useful in pillar design, they work effectively under the specific conditions they were created. Even if the confining stress

formula take into account multiple historical cases involving a wide range of mining environments, calibration still have to be done to get the mine pillar friction term specific for a particular mine. For this reason, empirical formulae cannot be used as a basis for design but rather just as a guidance tool. As such, the empirical pillar strength formulae have been used as guidance to the pillar strengths expected for the Mine X pillars.

2.3. Distinct Element Method (DEM) and Universal Distinct Element Code (UDEC)

DEM based computer programs (UDEC and 3DEC) were found suitable to model the Mine X jointed rock mass due to their capability to handle a large number of discontinuities. The key concept of DEM is that the intact rock is treated as an assemblage of rigid or deformable blocks that can displace and rotate about the contacts or completely detach and recognize new contacts (Potyondy & Cundall, 2004). As a result, the DEM approach can be used with ease to incorporate joints in modelling highly jointed pillars and in bonded particle modelling where the microscopic nature of the intact rock is modelled as an assemblage of particles (grains) cemented together by contacts.

The DEM approach was chosen over the continuum approach mainly because of the following reasons

- The joints in a continuum model can only be incorporated by downgrading the laboratory rock strength by some factor to give a rock mass strength (Hoek, et al., 2002).
- Modelling behaviours of jointed rock such as breaking of the rock bridges, detachment, sliding and rotation of blocks resulting from the interaction of newly formed cracks with pre-existing non-persistent joints in a continuum model may be difficult.
- Continuum models cannot explicitly simulate initiation and growth of fractures. Although strain softening may be applied where strength properties are smeared to simulate effectively opening up of cracks in the rock, the displacements that can be tolerated along these fictitious cracks are often limited.

2.4. Jointed pillar modelling using DEM

Esterhuizen (2000) conducted a study to investigate the effect of jointing on pillar strength. He realized that as pillar width to height ratio increases, the effect of jointing on pillars

decreases. As a result, it is not true to represent the effect of joints on pillar strength by only using the rock mass strength without taking into consideration the pillar width to height ratio. In a separate study, Esterhuizen, et al. (2011) developed a revised pillar strength equation for designing pillars in stone mines in the USA. The pillar strength equation takes into account the effect of the pillar width to height ratio and is given as:

$$S = 0.65 \times UCS \times LDF \times \frac{W^{0.5}}{\mathrm{H}^{0.59}} \quad \textbf{(8)}$$

Where:
S is the pillar strength in MPa
UCS is the uniaxial compressive strength of the intact rock in MPa
W and H are the pillar width and height, respectively, in meters
LDF is the large discontinuity factor which estimates the average impact of large discontinuities on the strength of the pillars. LDF is dependent on the fracture frequency and the dip of the discontuities.

A number of studies have been carried out that involve the modelling of jointing network in various software. These studies include the modelling of jointed pillars in the hybrid finite element/distinct element method (FEM/DEM) code ELFEN by Elmo (2006). Elmo (2006)'s approach involved the study of ELFEN pillar models' response with respect to mechanical parameters of discontinuities, loading rate and damping. Following this study, it was concluded that a lower joint stiffness is required to obtain a more realistic mechanical response of the modelled pillars.

Preston (2014) used the same approach to model pillars in UDEC. However, DFNs used in UDEC were created from fracture mapping carried out using photogrammetry. Although the use of photogrammetry required significant effort to calibrate, the obtained results compared well with the underground observations. It should however be noted that the actual mapping data was simplified to a certain degree hence there is a relatively low degree of certainty in the results obtained.

Zhang (2014) conducted a study in Particle Flow Code (PFC) to analyse the effects of jointing on hard rock pillars. The study found that orientation and size of the joint sets significantly influence the peak strength, post-peak residual strength, deformation modulus and lateral

stiffness ratio of the jointed pillars. The stress at which cracks initiate in the pillar was found to range between 30% and 45% of the peak strength and this percentage is not dramatically affected by the joint set characteristics. The damage stress threshold was found to vary between 70% and 98% of the peak strength depending on the joint set characteristics.

Chapter 3: Data collection and UDEC Modelling

Chapter 3 of this report discusses the data collection and UDEC modelling processes. The data collected was used as inputs into the model. The modelling process involved the use of 3DEC to create the three dimensional DFN that represents the jointing network underground. Intact rock between fractures was modelled as voronoi tessellation. Voronoi tessellation represent the intact rock micro particles with its contacts representing the cementation between them. The DFN and other data collected from the mine are used as inputs into the pillar model created in UDEC.

3.1. Data collection

The information gathering for the completion of the research included:

- Core logging data
- Structural mapping data
- Laboratory testing results
- Information from previous reports

3.1.1. Structural mapping

The mine did structural mapping and presented the acquired data. The information obtained was presented as a database with dip and dip directions of the joints. Mapping was conducted at the northern and southern sections of the mine at (Mine X, 2016):

- 5 N 148
- 26 N 117
- 30 N roadway
- 31 S strike
- 31 S dip
- 44 S to 52 S

Joint sets and their respective orientations were determined using the DIPS software. Figure 8 summarizes fracture orientation in the south and north sections of the mine. The north and south sections will be regarded as two separate domains, Domain 1 and Domain 2 respectively. More details are provided in Section 3.2.1 of this report.

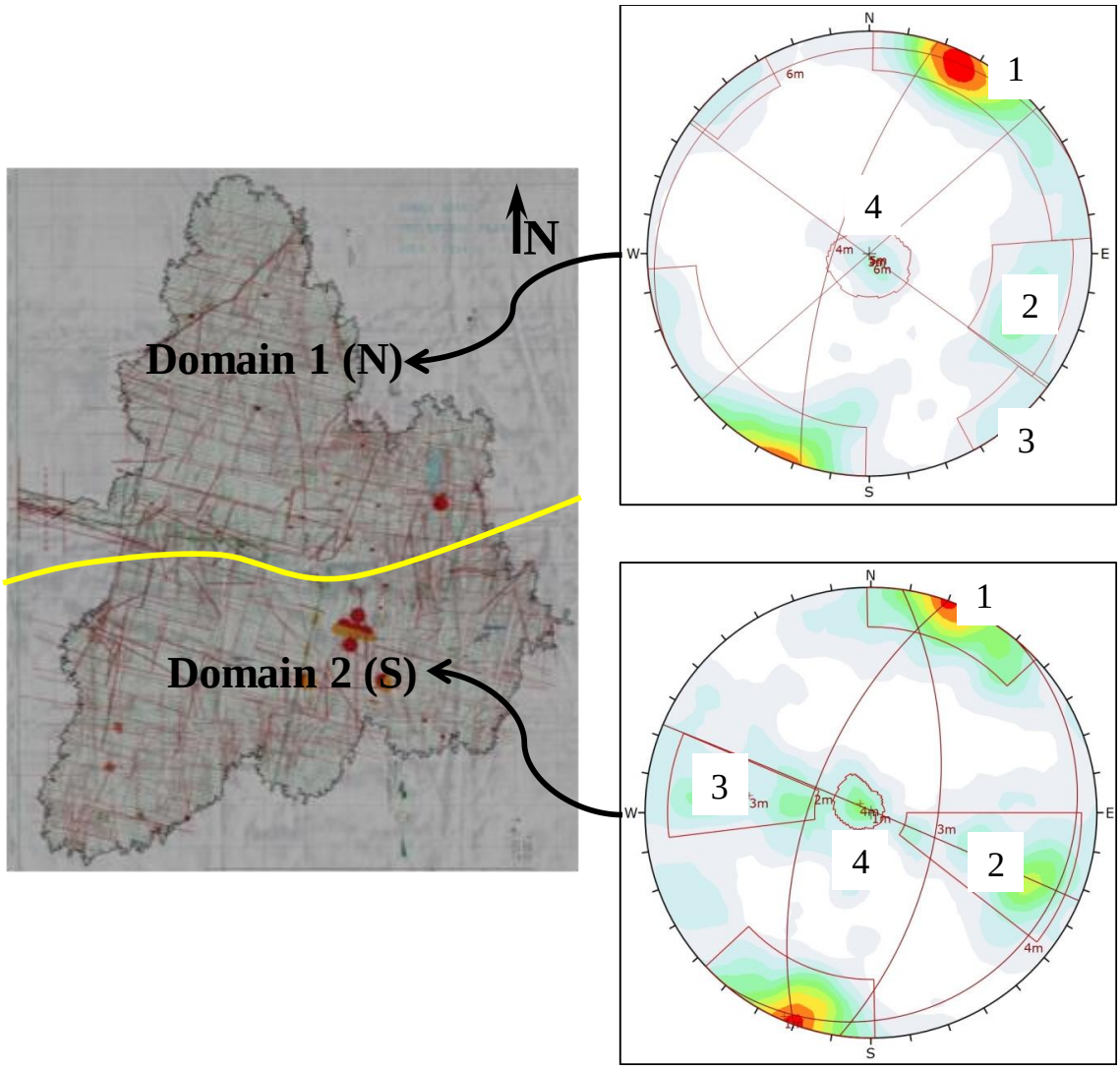


Figure 8: Fracture orientation in domain 1 and domain 2 (Mine X, 2016)

3.1.2. Core logging

P_C core logs could not be obtained from the mine because of political reasons. It was assumed that the geological conditions between P_B and P_C do not vary significantly. Core logging data from P_B was used for the purposes of this research.

A total of about 3300 m of core from 130 holes were logged by SRK as part of a mining geotechnical study. The scope of the study was to characterize the rock mass, identify prominent and/or unusual geological structural aspects and produce a high quality set of consistent geotechnical logs representing the rock mass in the immediate vicinity of the ore zone (SRK Report No. 480443, 2015). The rock mass was classified using the Barton, et al.

(1974)'s Q and Laubscher (1990)'s RMRL90 systems and Geological Strength Index (GSI) values were derived using Hoek (2012) approach.

The value of Q was determined for each geotechnical interval in each borehole. To obtain an indication of the distribution of rock mass conditions in the hanging-wall, orebody and footwall zones, it was necessary to use weighted averages of the logging intervals representing hanging-wall, orebody and footwall respectively, and contouring the results. However, Q values are expressed on a log scale such that linear statistical analysis and contouring are not possible. Therefore, the Q values were converted to Bieniawski (1989)'s Rock Mass Rating (RMR) for the purpose of statistical analysis and contouring. Mean values were then back-calculated to obtain representative Q-value distributions. The relationship between Bieniawski (1989)'s RMR and Q is as follows:

$$RMR = 9lnQ + 44 \quad \textbf{(9)}$$

The range of RMR is largely between 65 and 75 (fair to good quality), with a standard deviation between 10% and 12% of the mean. In all the boreholes, the representative RMR values for the hanging-wall, orebody and foot wall zones, were determined by conducting a weighted average of the RMR values of the individual geotechnical intervals included in each zone. This operation was performed using the software package, GEMS. The 20th percentile of the weighted average RMR values, calculated per borehole, per zone (hanging-wall, footwall and orebody), is presented in Figure 9 and Table 4. Representative Q values calculated back from statistical RMR results are presented in Table 5. The 20th percentile means that 80% of the resulting rock mass conditions are accounted for in the design parameters according to Portvin and Hadjigeorgiou (2001)'s approach for stability analysis in massive open stope design

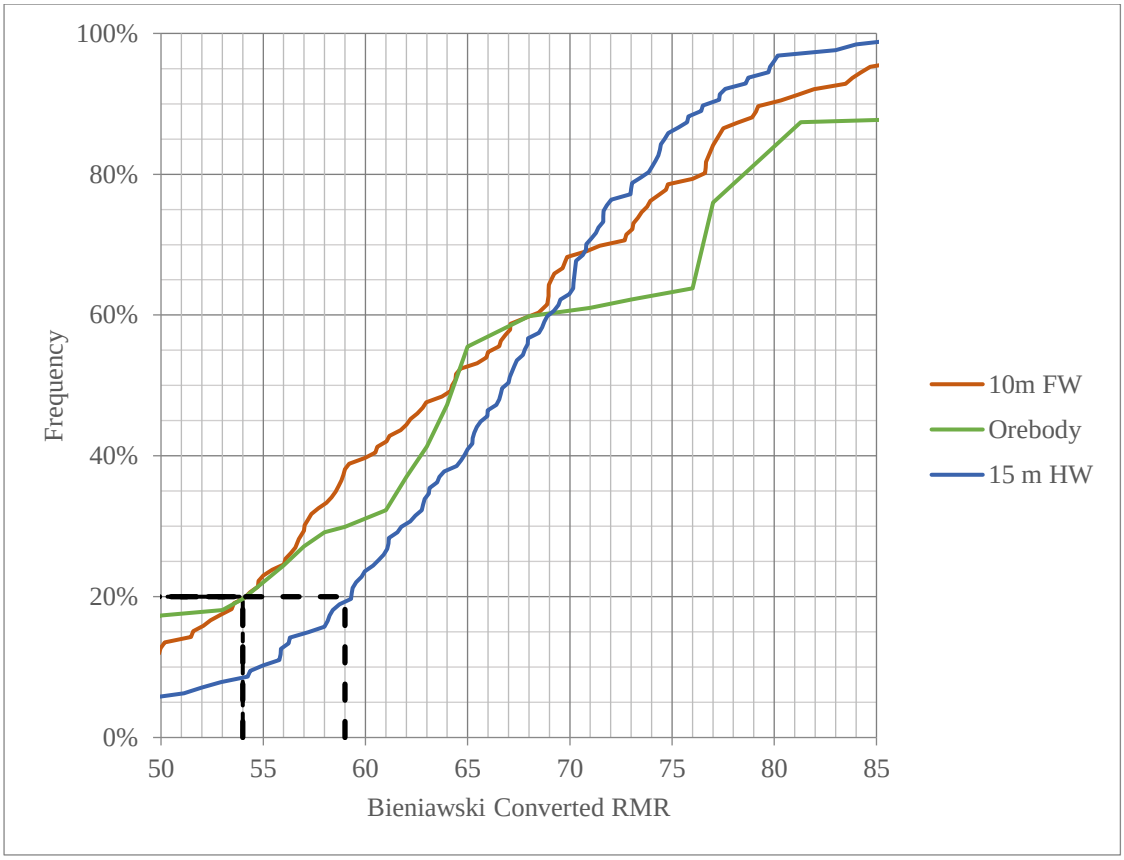


Figure 9: Cumulative frequency curve of Q values

Table 4: Rock mass quality (RMR converted from Q)

Stats	**Hanging-wall**	**Orebody**	**Footwall**
Mean (mean of the weighted means)	66	66	65
Std. Deviation	11	16	12
Min (min of all weighted composites)	21	19	40
Max (max of all weighted composites)	87	92	92
Mean + Std. Deviation	76	82	77
Mean – Std. Deviation	55	50	53
20 percentile	59	54	54
No. of boreholes	127	127	126

Table 5: Rock mass quality (Q)

Stats	Hanging-wall	Orebody	Footwall
Mean	11.1	11.5	9.5
Std. Deviation	- (n/a)	- (n/a)	- (n/a)
Min	0.01	0.01	0.2
Max	304.3	631	631
Mean + Std. Deviation	- (n/a)	- (n/a)	- (n/a)
Mean – Std. Deviation	- (n/a)	- (n/a)	- (n/a)
20 percentile	4.2	1.9	2
No. of boreholes	127	127	126

Laubscher (1990)'s Mining Rock Mass Rating Classification System evaluates discrete geotechnical domains based on strength i.e. Intact Rock Strength (IRS), fracture frequency, joint condition and weathering characteristics. Each of the resultant domains is evaluated separately, through the allocation of rating values, within a specific range, for each parameter. The calculation used to determine RMR values is expressed as follows:

$$RMR = IRS + FF + \left(J_{Cmicro} \times J_{Cmacro} \times J_{infill} \times J_a \times 40\right) \quad \textbf{(10)}$$

Where:

IRS is the intact rock strength

FF is the fracture frequency per meter

J_{Cmicro} is the joint condition number representing small scale joint expression

J_{Cmacro} is the joint condition number representing large scale joint conditions

J_{infill} is the joint filling rating

J_a is the joint wall alteration number

The value of RMR was further determined for each geotechnical interval in each borehole using the compositing method. To obtain an indication of the distribution of rock mass conditions in the hanging-wall, orebody and footwall zones, it was necessary to use weighted

averages and contouring. In all the boreholes, the RMR values for the hanging-wall, orebody and footwall zones, were determined by conducting a weighted average of the RMR values of the individual geotechnical intervals included in each zone. Since the rock quality was found to be generally good, it was considered unnecessary to define geotechnical domains based on rock mass quality.

The cumulative frequency curve for the rock units located 15 m above the orebody, within the orebody and 10 m below the orebody are presented in terms of RMR in Figure 10. The 20th percentile is indicated on the graphs. The summaries of the composited RMR values for the orebody, footwall and hanging-wall are presented in Table 6. The 20th percentile RMR is in between "fair", i.e. RMR = 56 for the orebody and footwall and RMR = 63 for the hanging-wall.

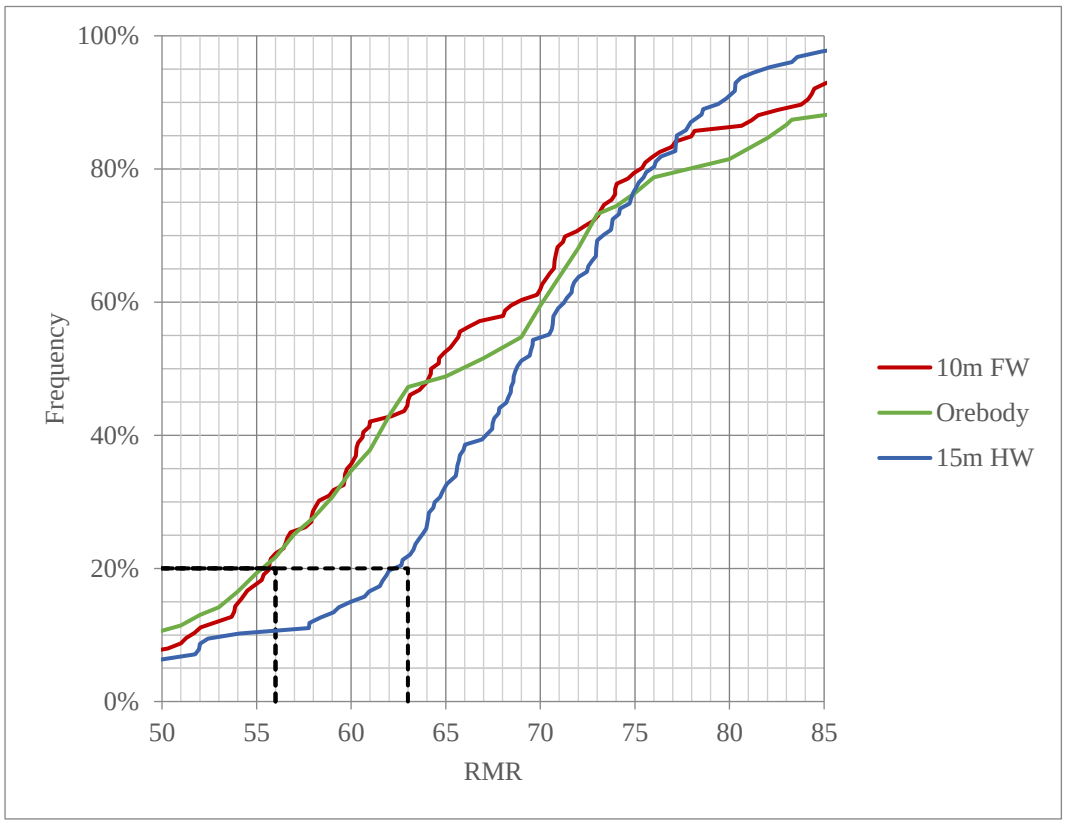


Figure 10: Cumulative frequency curve for RMR values

Table 6: Composited Rock Mass Quality (Laubscher (1990)'s RMR values)

Stats	Hanging-wall	Orebody	Footwall
Mean	68	67	66
Std. Deviation	12	18	13
Min	15	14	30
Max	92	100	100
Mean + Std. Deviation	79	85	79
Mean – Std. Deviation	56	49	53
20 percentile	63	56	56
No. of boreholes	127	127	126

GSI values for the respective hanging-wall, orebody and footwall zones were calculated to determine rock mass properties for non-linear modelling to be conducted. The following expression was used to calculate GSI after Hoek (2012) from the raw Q input parameters:

$$GSI = \left(\frac{52\frac{J_r}{J_a}}{1 + \frac{J_r}{J_a}} \right) + \frac{RQD}{2} \quad \textbf{(11)}$$

Where:

J_r is the joint roughness coefficient

J_a is the joint alteration number

RQD is the rock quality designation

GSI was calculated for each geotechnical interval. Table 7 presents a summary of GSI values for the ore zone and the immediate hanging-wall and footwall.

Table 7: GSI Results

Stats	Hanging-wall	Orebody	Footwall
Mean	78	78	77
Std. Dev	15	15	14
Min	18	22	19
Max	92	92	92
Mean + Std. Dev	93	93	91
Mean – Std. Dev	63	64	63

The fracture intensity obtained from the boreholes was hereinafter utilized to generate the DFNs in section 3.2 of this report.

The Laubscher (1990)'s RMR, RMR from Q and GSI are different methods of rock mass qualification and are used for different purposes which accounts for some variability in the results. In particular, the GSI returns a significantly higher mean value ("good" to "very good" ground). However, the premise on which GSI is calculated excludes factors such as the rock strength and rock stress parameters by Laubscher and Barton respectively (Hoek, 2012). These methods are therefore not directly comparable.

3.1.3. Laboratory testing results

SRK received a database of previous rock testing campaigns at P_A, P_B and P_C from the mine. As part of the study that was carried out on P_B by SRK, additional samples were collected at P_B and were sent to a commercial laboratory for testing.

Intact rock laboratory testing results

Figure 11 presents all the Uniaxial Compressive Strength (UCS), Triaxial Compressive Strength (TCS) and Uniaxial Tensile Brazilian (UTB) test results combined in a minor and major principal stress plane. The locations of the samples are also included in the plot. From a rock properties perspective, it is evident that there is minor difference in strength between the reef, the footwall and the hanging-wall and a single value can be used to represent rock strength for all (reef, footwall and hanging-wall). Although the reef has a wider spread of UCS values ranging from 200MPa to 450MPa, a UCS of 200 MPa was considered conservative and therefore preferred for the modelling.

Three Hoek-Brown envelopes were fitted to the data. One representing the mean UCS value and the two others representing the mean UCS + 1 x standard deviation and UCS – 1 x standard deviation respectively. The distance between the three curves gives an insight into the scattering of the data and possibly, the rock strength variability.

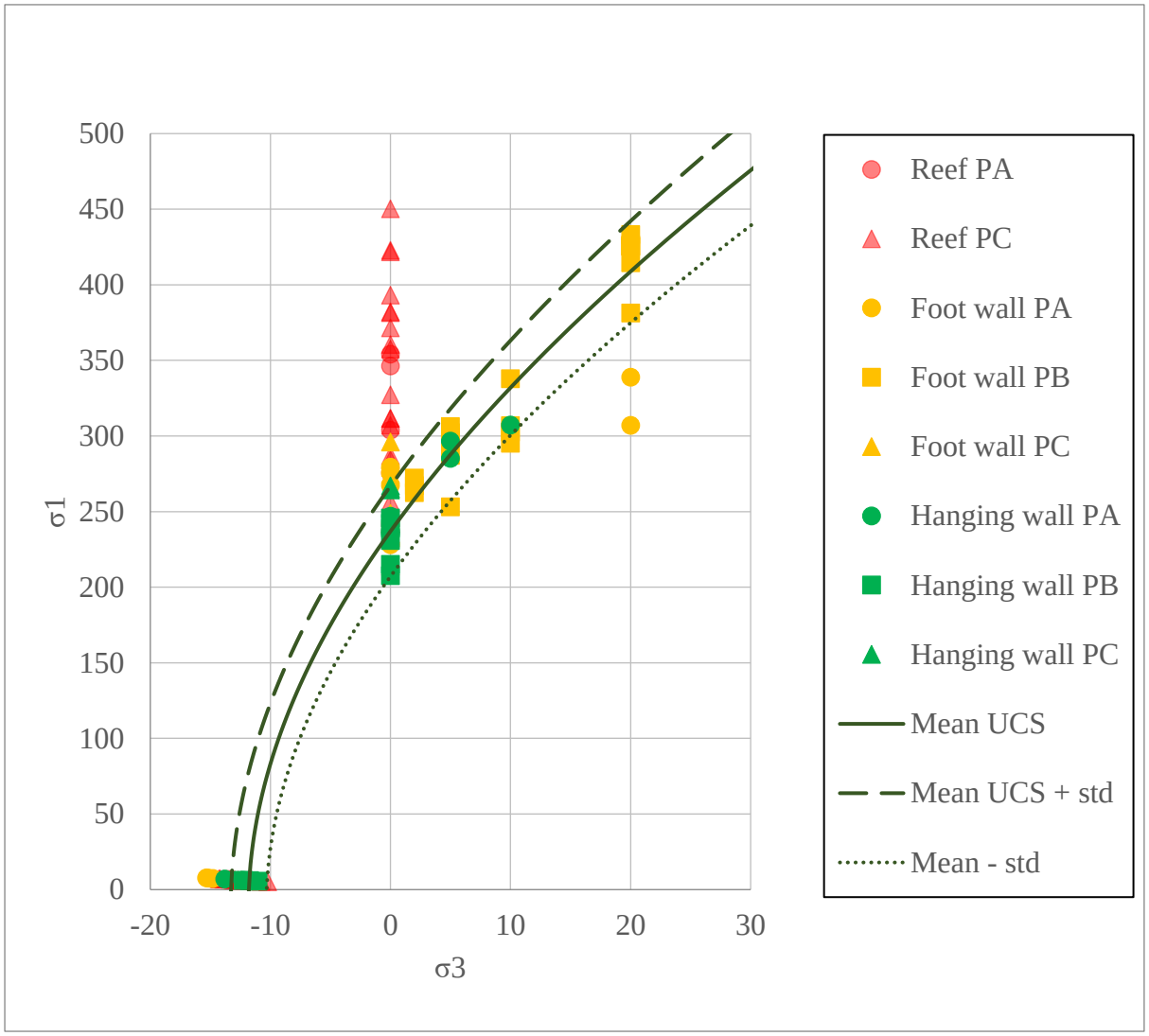


Figure 11: Summary of rock testing programs

Joint laboratory tests

Joint samples were collected for base friction angle (BFA) and direct shear on open joint (SHJO) test. A commercial laboratory did sample testing. Table 8 and Figure 12 show both BFA and SHJO tests results.

Table 8: Summary of BFA and SHJO test results

		SHJO: Friction angle (º)		SHJO: Cohesion (MPa)	
Parameter	**BFA**	**Peak**	**Residual**	**Peak**	**Residual**
No of samples	16	12			
Minimum	30º	17º	19º	0.1	0
Maximum	41º	34º	34º	0.3	0.4
Mean	37º	23º	26º	0.2	0.1
Stdev	3º	5º	4º	0.08	0.09
CoV (%)	8%	21%	15%	40%	90%

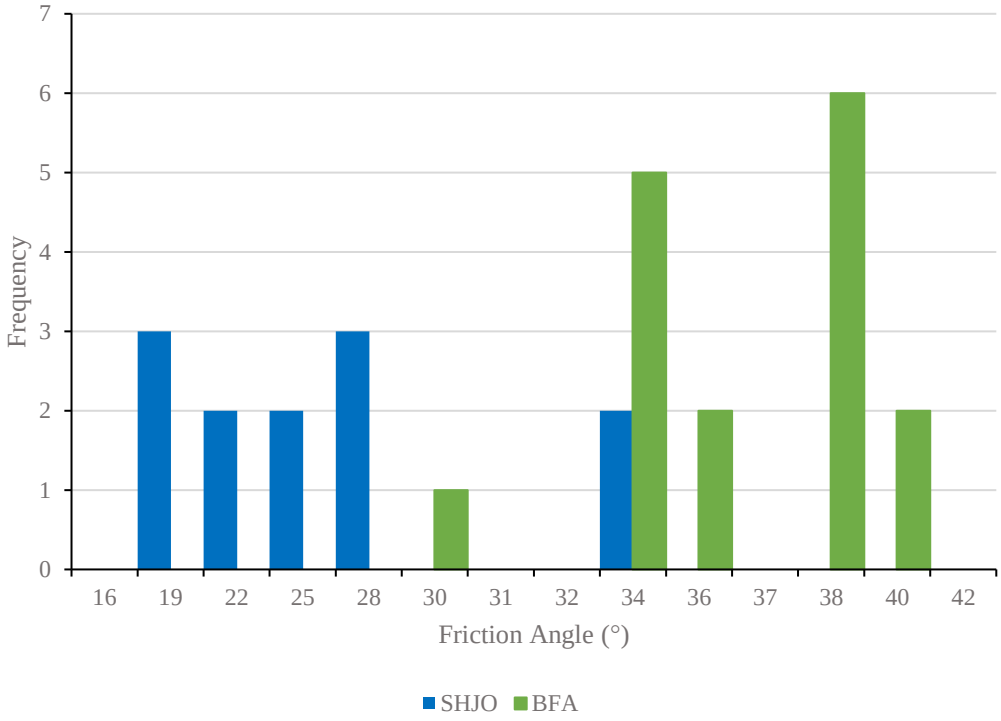


Figure 12: Distribution of peak friction angle in BFA and SHJO tests

Contrary to expectation, BFA results were consistently higher than peak friction angles obtained in the SHJO tests. The reason for this discrepancy would need to be further investigated. For conservative purposes, the SHJO testing results were used for the modelling.

3.1.4. Previous reports

Reports on work previously done by SRK at Mine X were also used as source of valuable information for the nonlinear modelling. These include inter alia:

- SRK Site visit report – Mine X (P_B), (SRK Report No. 482668, 2014)
- Mine X Portal B – Geotechnical Logging Report, (SRK Report No. 480443, 2015)

SRK Report No. 482668 (2014) describes underground observations made during the site visit undertaken by SRK at Mine X (P_B) in the context of a geotechnical study following the failure at P_B. The visit focused on information pertaining to Falls of Ground (FoG) and associated geotechnical conditions. This investigation gave valuable insight into the actual mechanism of failure for hanging-wall, pillar sidewalls and footwall. The pillar failure mechanism was observed to be dependent on the position of the shear. Where shear was in the footwall, footwall heave was observed. Pillar buckling and hanging-wall failure was observed where shear is in the orebody and hanging-wall respectively.

SRK Report No. 480443 (2015) summarizes a mining geotechnical study comprising logging of drill core and rock mass classification. The scope of the study was to characterize the rock mass, identify prominent and/or unusual geological structural aspects and produce a high quality set of consistent geotechnical logs representing the rock mass in the immediate vicinity of the ore zone. The core logging was performed on 130 holes, or a total of 3300 m. The rock mass classification was conducted based on Barton, et al. (1974) Q-system and Laubscher, (1990) Rock Mass Rating (RMR). The findings from this report are summarised in section 3.1.2 of this report.

3.1.5. Underground observations

Photographs from previous site visits have tremendously assisted the calibration of numerical models with the necessary visualization of failure mechanisms and actual rock mass conditions. Figure 13 shows the existence of low angle joints with infilling.



Figure 13: Existing low angle joints with infilling

Figure 14 shows a FoG associated with unravelling of joint-bound blocks and wedges in the hanging-wall towards the top entrance of switchback 1. Figure 15 shows tensile failure in the shotcrete against the sidewall of a pillar in the immediate proximity of a FoG. Evidence of stress-induced tensile fractures and joint mobilisation within a pillar were seen in Figure 16. Most of these mechanisms are in good agreement with the descriptions provided in Figure 3.



Figure 14: Fall of ground at the top of switchback 1



Figure 15: Shotcrete failure against the sidewalls

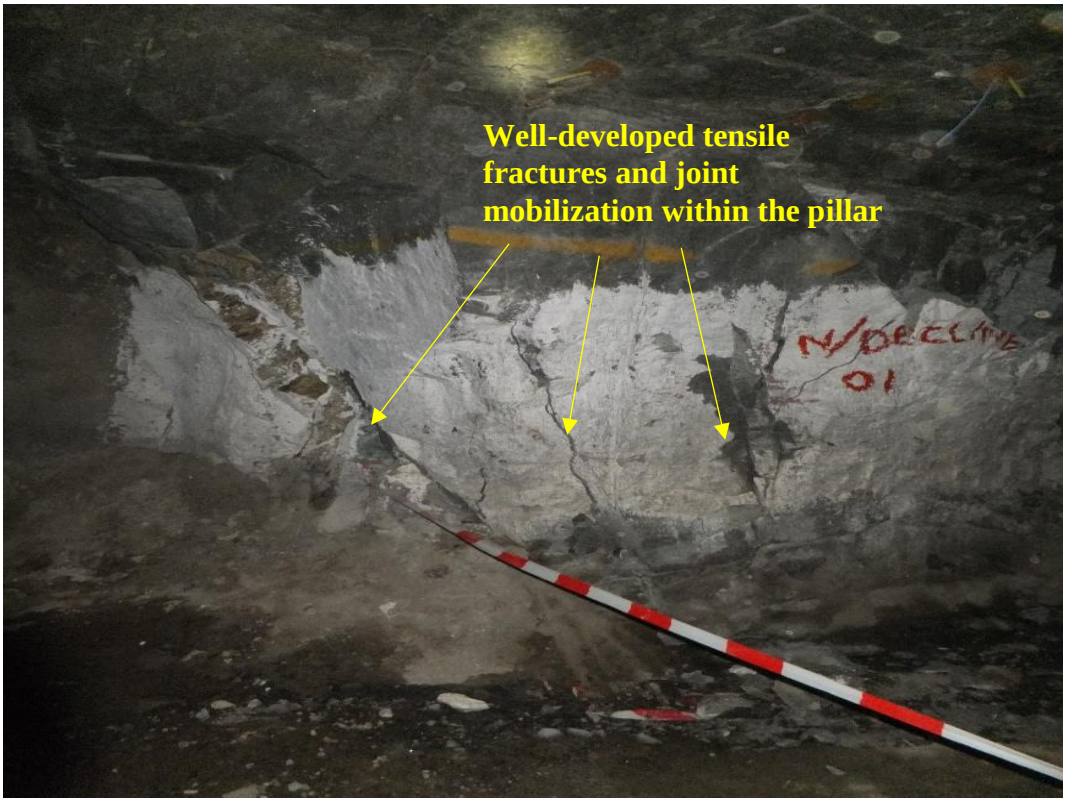


Figure 16: Pillar sidewall conditions with stress induced tensile fractures and joint mobilization with the pillar

3.2. DFN model construction

DFNs are a statistical description of fractures (Preston, 2014). Fractures are often represented deterministically, where faults that were mapped are represented explicitly in the model by specifying their real location, orientation and direction. Only a few fractures can be represented in this manner. Hundreds and thousands of joints may be difficult if not impossible to represent.

With the DFN approach, individual fractures are not modelled explicitly. Instead, a set of statistical parameters are defined and a joint set is generated based on the input statistical distributions (Preston, 2014). In doing so, the joints represented in the model do not directly represent mapped fractures and is not unique, but statistically represents the jointing criteria.

The built-in DFN generator within 3DEC was used in this study to create several DFNs. The DFN model takes into consideration the following:

- Fracture orientation distribution

- Fracture shape and size distribution
- Fracture position distribution

This section describes the selection of each input distribution and the derivation of associated parameters.

3.2.1. Fracture orientation

Joint sets and their respective orientations were determined using the code DIPS software. Figure 17 shows stereonet plots with concentration contours and poles of the fractures mapped at P_C. There are three main sub-vertical sets in both domains (Set 1, Set 2 and Set 3). Set 4 is a flat dipping set which is dominant in domain 2.

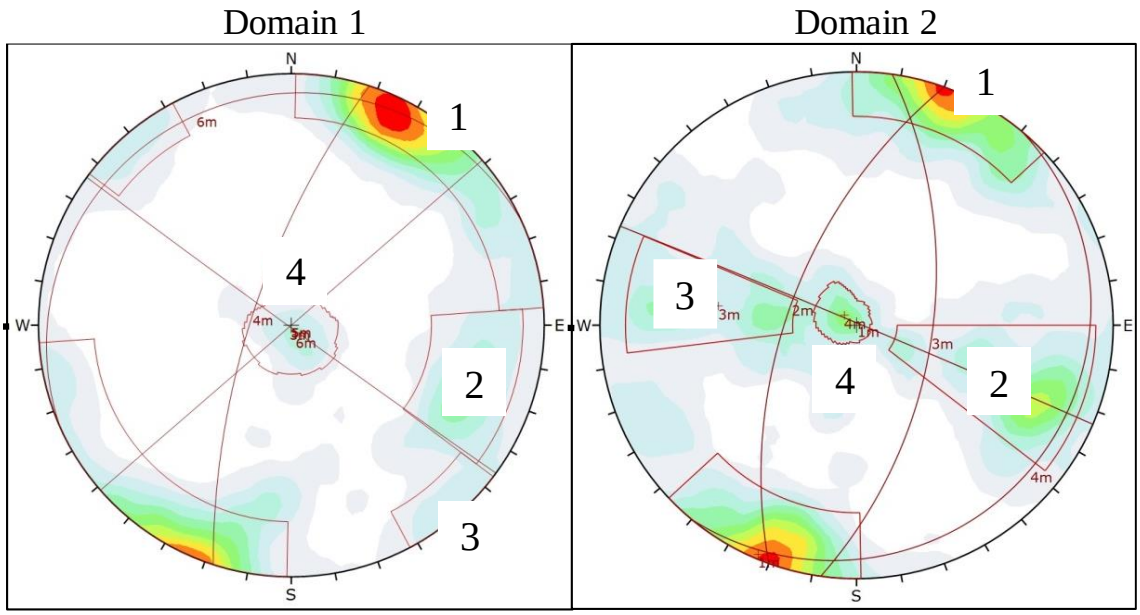


Figure 17: Stereonet plot of fractures mapped at Portal C (DIPS software)

Amongst the orientation distributions currently available in 3DEC, the Fisher distribution was deemed more appropriate to fit fracture orientation data. The mean dip and dip-direction of the joint set and a coefficient of dispersion K (Fisher coefficient) describe the Fisher distribution. A high K value implies more clustered data and less variability (Elmo, 2006). The K values were determined directly from the code DIPS based on actual mapping data (Section 3.1.1). Table 9 summarizes the identified joint sets.

Table 9: Summary of identified joint sets in terms of dip, dip direction and Fisher's coefficient K

Joint set	Domain 1 (N)			Domain 2 (S)		
	Dip (°)	Dip dir (°)	Fisher's K	Dip (°)	Dip dir (°)	Fisher's K
1	88	215	14	89	23	33
2	72	287	40	60	290	14
3	90	318	88	57	98	20
4	5	336	13	7	130	93

DFN 1 and DFN 2 were created to represent joint orientations in Domain 2 and Domain 1 respectively. Shallow dipping joints are significantly observed in DFN 1 as shown in Figure 18.

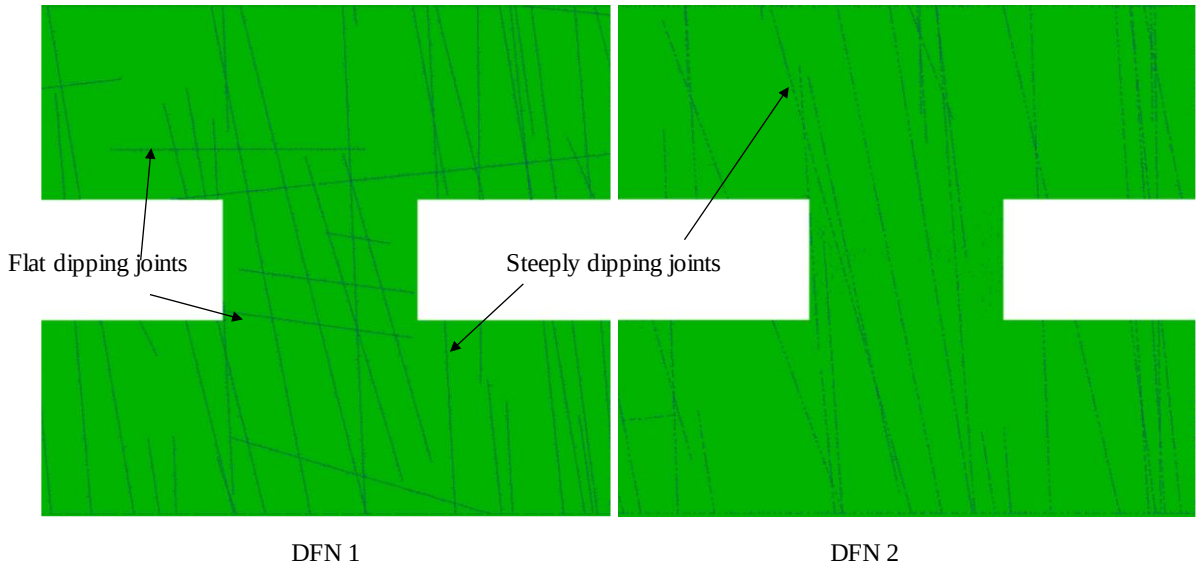


Figure 18: DFN 1 and DFN 2 models

3.2.2. Fracture size distribution

The current version of the DFN facility in 3DEC only supports circular fractures (Itasca Consulting, 2015). The power law distribution was selected. The reason being that, in rocks, the lengths of discontinuities tend to follow a similar distribution. The power law is defined by the following equation:

$$n(l) = \alpha l^{-a}$$ (Itasca Consulting, 2015) **(12)**

Where:

n(l): number of fracture whose size equal to l

l is the fracture size

a: positive scaling exponent. It sets up the ratio between fracture size (smaller and larger) and is commonly defined in a range [3;4]. If "a" approaches infinity, a model of constant fracture size is obtained, while a model of infinite fracture size is obtained when a < 2.

α represents the number of fractures with a length equal to unity. It is a density factor whose effect on the fracture size distribution is illustrated in Figure 19.

3DEC requires the minimum fracture size to be assigned. The minimum and mean fracture sizes ($\bar{l}$ and l_{min} respectively) are related by the following equation:

$$\bar{l} = \frac{\alpha - 1}{\alpha - 2} l_{min} \quad \textbf{(13)}$$

The mine advised that 14m and 5m be used as mean and minimum fracture lengths, respectively. Using this information, the parameter "a" was derived to be 2.5.

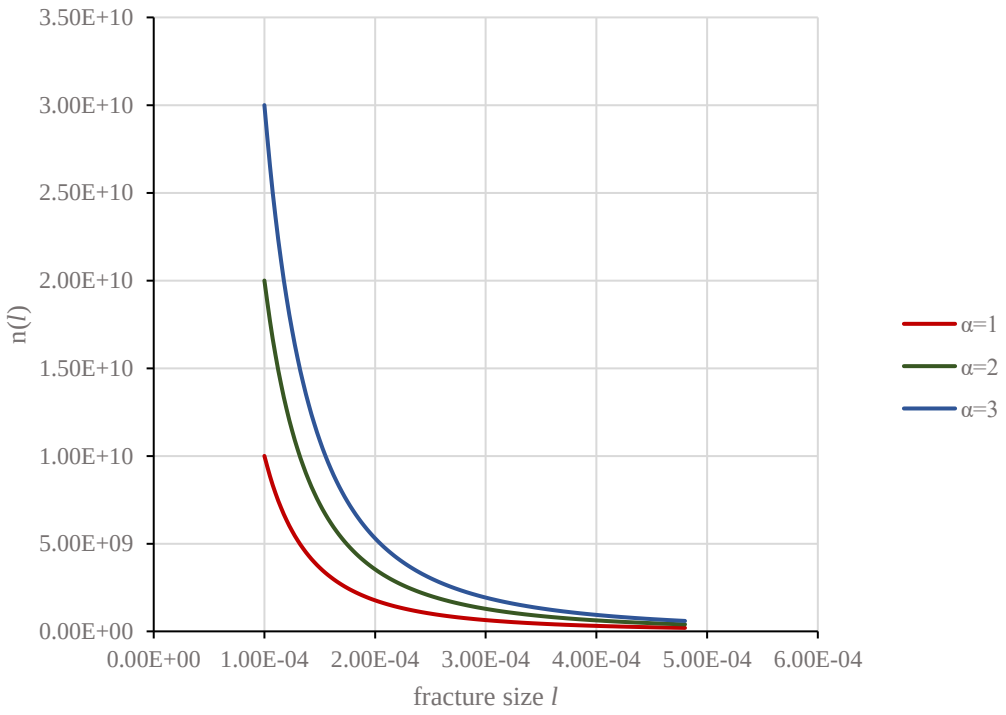


Figure 19: Effect of α on fracture size distribution for a=2.5

3.2.3. Fracture position distribution

A uniform, Gaussian, bootstrapped or FISH defined distribution can define the positions of the centres of discontinuities in 3DEC (Itasca Consulting, 2015). A uniform distribution was used in this study for simplicity. In case of a uniform distribution, 3DEC does not require it to be explicitly defined in the DFN model. Figure 20 shows the 3D DFN model created in 3DEC

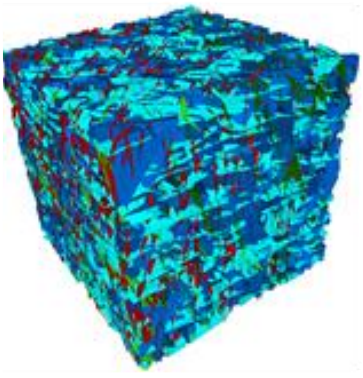


Figure 20: the 3D DFN model in 3DEC

3.2.4. Migration from 3 dimension DFN to 2 dimension DFN

To account for boundary effects, the DFN model representative of a pillar was generated within a larger domain whose dimensions are 100 m x 100 m x 100 m. In addition, it was important for the DFN domain to be of comparable dimensions as the areas actually mapped to account for the scale dependency of the mapping parameters. Figure 21 shows how the pillar region compares to the surrounding DFN domain.

The pillar region was rotated to align the axis of the pillar with the dip direction of the orebody as per the current mining orientation. Slices through the 3D DFN had to be made for input into the 2D analysis in UDEC. For each joint set, two slices were cut, on dip and strike. However, only sections along dip were used in the analysis as sections on dip were found to have higher fracture intensity than those on strike and therefore were considered more representative of the actual pillar strength conservatively.

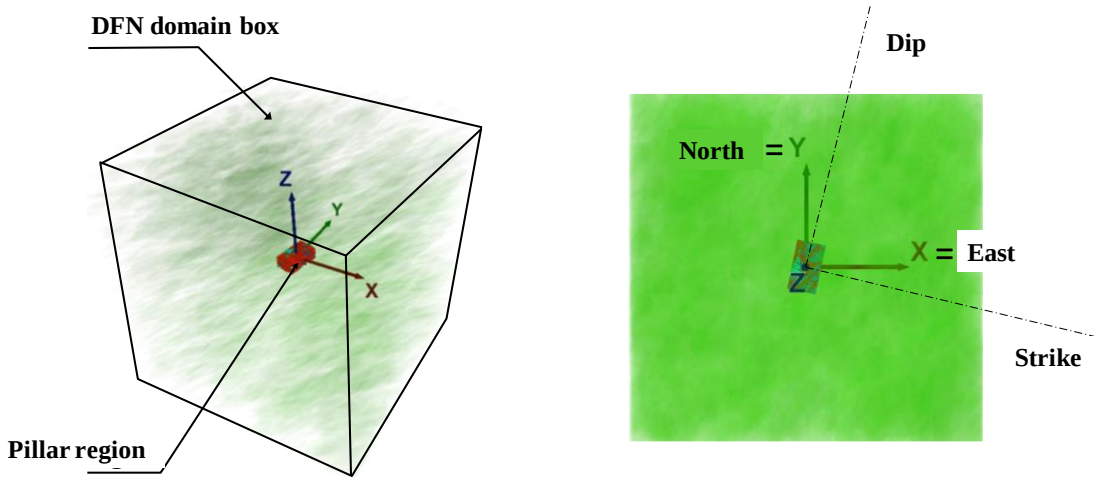


Figure 21: DFN domain and pillar region settings for P_C model in 3DEC, isometric view on the left and plane view on the right

3.3. UDEC Modelling

3.3.1. Pillar model Geometry

Rock specimens with their ends constrained by steel rings were first used for in situ tests on large-scale rock specimen prior to be adopted in numerical modelling (Elmo, 2006; Preston 2014). Babcock (1968) observed that experimental models of pillars with their ends constrained by steel rings were better for predicting the strength of mine pillars than either

cylindrical or prismatic specimens. Similarly, (Bieniawski & Van Heerden, 1975) argued that the constraining effects produced by the roof and floor on a coal pillar could be simulated by the introduction of wood/steel shuttering on the top and bottom of the specimen.

The "baseline" model consisted of a 4 m intact rock pillar, which was subjected to a constant velocity as in a conventional UCS laboratory test. Figure 22 shows the baseline model. The rigid steel equivalent platens on both ends are intended to produce a uniform lateral constraint. Since the strength of the pillar also depends on the way the pillar interacts with the surrounding strata, it was deemed important to include parts of the hanging and footwalls on either side of the pillar over a distance corresponding to half the width of the bords.

The fractured pillar was modelled with its jointing extending into the footwall and hanging-wall as observed in reality The jointing was extended up to the contacts with the steel platens as shown in Figure 22.

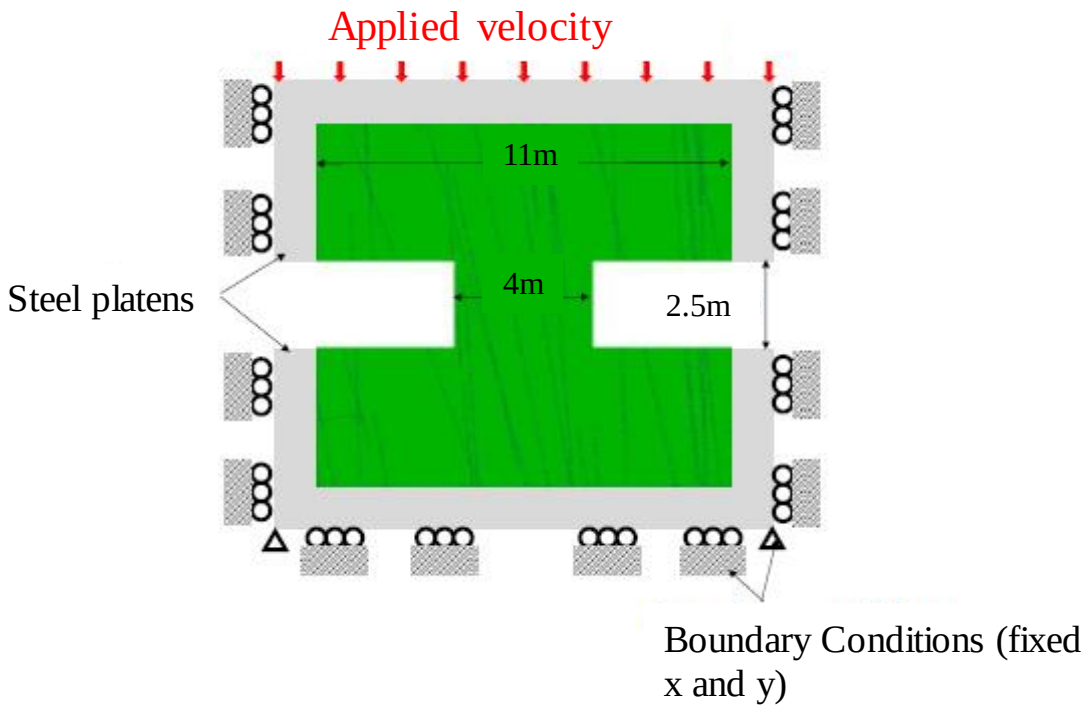


Figure 22: Typical Mine X jointed pillar model geometry – Dimensions and boundary conditions

Figure 22 and Figure 23 show a specific P_C DFN model incorporated in the UDEC model to represent a particular jointed geometry. The fracture geometry data from the P_C DFN model

were exported from 3DEC in a data file defining fractures as 2D traces, with coordinates associated with both ends of the trace and the dip angle of the trace line.

The intact rock between pre-existing joints was simulated as an assemblage of voronoi tessellation cells. The joint tresses exported from 3DEC terminated at the nearest contact (voronoi contact, joint tress or boundary). The presence of voronoi particles enabled a close approximation of joint tresses defined by the DFN. The micro-properties of the interfaces along the voronoi tessellation cells were calibrated to replicate macro-properties of the rock on the scale of the laboratory samples or rock mass in situ. Further details regarding the calibration of the intact rock are provided in Section 3.4.1.

The edge length for the voronoi tessellation cells used in the models was kept at 8 cm, which seemed to be the smallest length that UDEC could generate. UDEC also requires for minimum edge and rounding lengths to be specified as part of the analysis. The minimum edge length should be small enough that the voronoi tessellation can adjust and create smaller blocks to fill spaces at the boundaries of the tessellation regions (Itasca Consulting, 2014). In this analysis, a minimum edge length of 10 cm was selected. The rounding length was taken as one tenth of the minimum edge length as recommended in UDEC supporting documentations.

Deformable blocks were used in the analysis. This implies that the entire UDEC model was meshed as shown in Figure 23. The minimum mesh element size was taken as the same as the voronoi tessellation edge length and was kept the same for all pillar sizes. The top and bottom platens were modelled using a larger element size of 0.5 m.

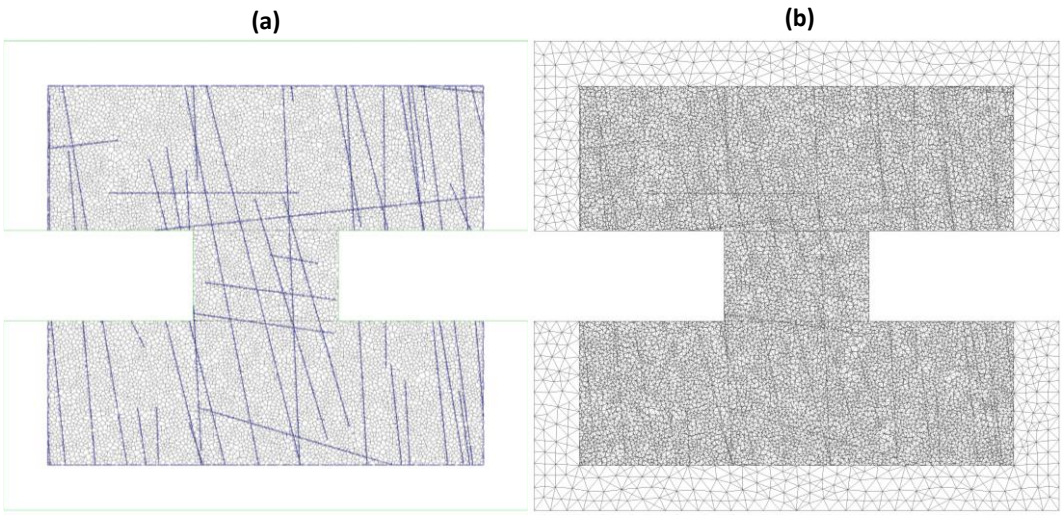


Figure 23: UDEC model of Mine X jointed pillar. (a) Pre-existing fractures and voronoi tessellation, (b) Typical mesh/grid

An initial state of stress corresponding to the weight of the pillar under gravity loading was initiated within the mesh prior to activating the gravity field stress. The model was brought to equilibrium under these conditions and then the drives on either side of the pillar were excavated and the model brought to a new state of equilibrium. The gravity field stress was then initiated and the pillar loaded with constant velocity until it failed. History points were put along the pillar centre line and average pillar stress calculated as the average of the zones along this line.

3.3.2. Loading rate

The load was assigned as a constant applied velocity at the top platen, the bottom platen being fixed in the x and y directions as indicated in Figure 22. To assess the effect of the loading rate, a sensitivity analysis was carried out. Ideally, the loading rate should have been reduced until the difference between results obtained are negligible. However, due to the lengthy runtimes involved, it was decided to carry out the sensitivity analysis at three different velocities, 0.01 m/s, 0.05 m/s and 0.1 m/s, representing a slow, moderate and fast loading rate, respectively. The fast loading rate is representative of conditions where the hanging-wall collapses violently onto the pillar, whereas the slow rate would represent normal loading conditions due to gravity and mining. A relatively low local damping coefficient of 0.3 was used in the analyses.

Figure 24 shows the average pillar stress versus axial displacement curves corresponding to each loading velocity. There is no difference between the three curves over the pre-peak part of the average pillar stress versus axial displacement curve. The peak pillar strength in the model with velocity of 0.01 m/s is lower than that of the model with faster loading rates (150 MPa vs. 175 MPa). Both faster models with 0.05 m/s and 0.1 m/s exhibited very similar peak pillar strength. The model with 0.1 m/s velocity was run further and exhibited strain hardening up to a second peak strength of about 250 MPa. Afterwards, a brittle (sudden) loss in strength occurred. The sudden loss in strength corresponds with the massive explosion of the pillar.

The 0.01 m/s velocity model exhibited the most expected behaviour characterized by a staircase post-peak pillar strength behaviour with successive rock bridges failure. In addition, this particular model exhibited a much greater residual pillar strength over a larger strain range. This could be due to some degree of confinement provided by the broken rocks, which, instead of being ejected, in this case remained attached to the pillar walls.

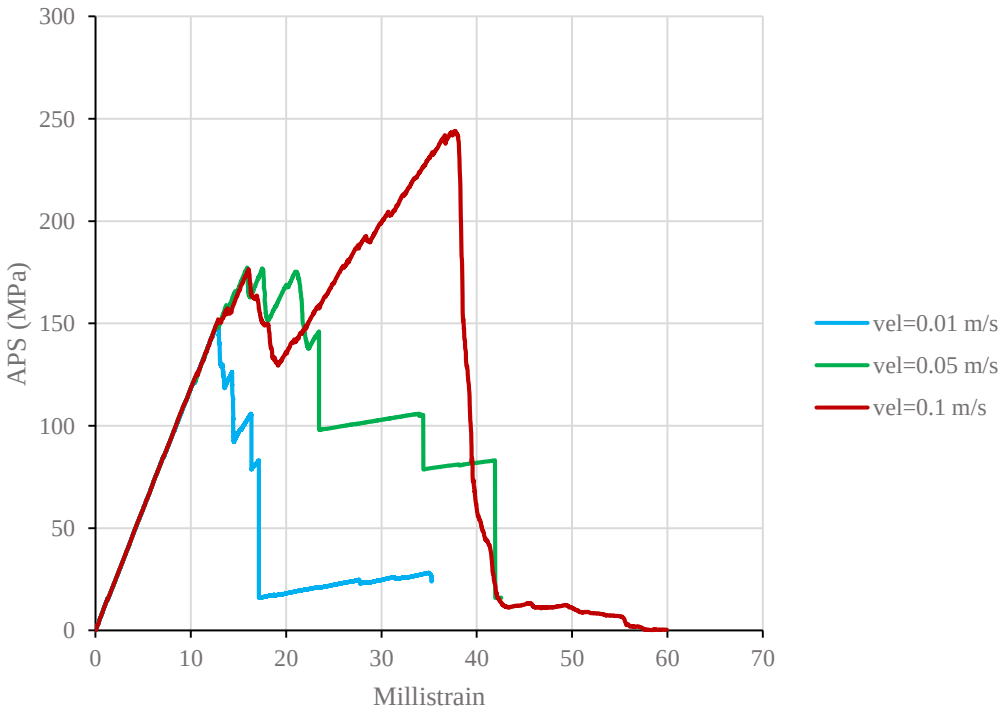


Figure 24: Loading velocity sensitivity: Average pillar stress vs. pillar strain curve

It is important to monitor the total kinetic energy dissipated during a simulation. The unbalanced force is a measure of the free kinetic energy in the model at any given time. The

higher the unbalanced force the less desirable the situation. High unbalanced forces indicate violent failure which might not be realistic but may be induced by the high loading rate.

Figure 25 shows the unbalanced force in kN monitored within the model during the simulations. For the 0.01 m/s velocity model, it can be seen that the kinetic energy was kept consistently low over the entire simulation. Conversely, for the faster simulation with velocity=0.1 m/s, there is a rapid increase in kinetic energy, which corresponds with the massive explosion of the pillar observed earlier.

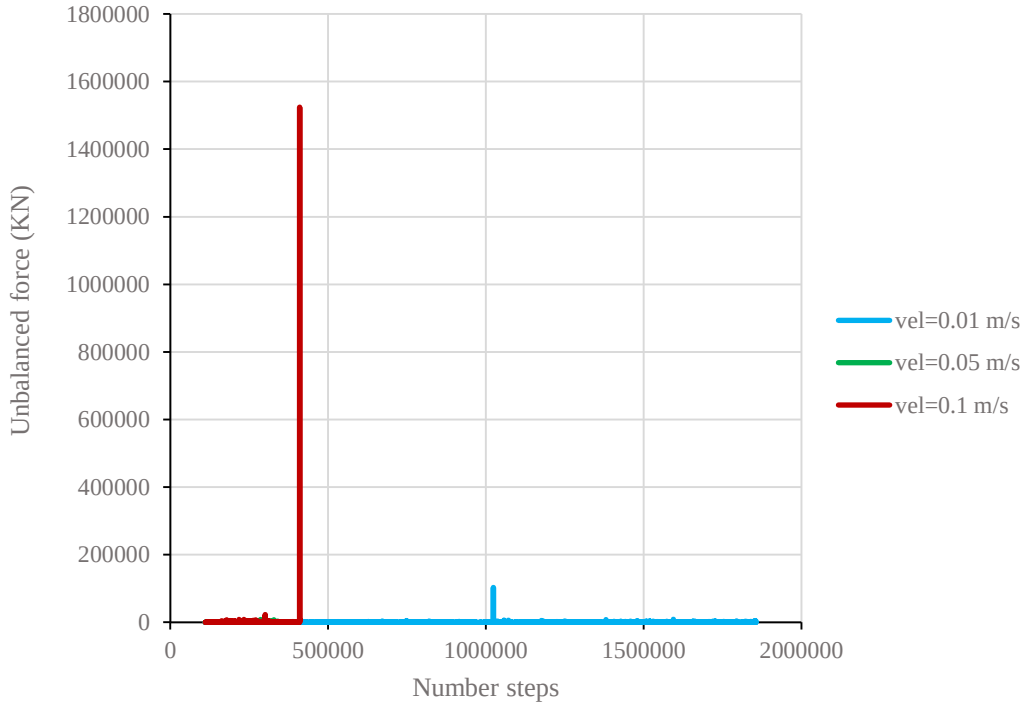


Figure 25: Loading velocity sensitivity: Unbalanced force

The loading rate sensitivity analysis indicated that the velocity had to be kept as low as possible. However, lengthy runtime of more than 24 hours per run could not be avoided.

3.3.3. Mechanical Damping

Mechanical damping in a numerical model is designed to simulate the natural energy dissipation in the rock mass. For dynamic problems, to obtain an accurate solution it is important that the damping used in the model reflect the magnitude and nature of the actual damping in the rock. The Rayleigh damping is commonly used to obtain a frequency

independent response over a certain frequency range by scaling simultaneously mass and stiffness of the system (Itasca Consulting, 2014).

However, for static problems damping is used for a different purpose and is only needed because UDEC solve equations of motion using an explicit dynamic scheme even for quasi-static problems. If it had not been for that, damping would not be required to solve static problems. For static problems, the role of damping is just to remove the energy due to unbalanced forces and bring the system to a state of equilibrium as fast as possible (Itasca Consulting, 2014). Hysteresis based damping is often avoided due to the numerous associated problems such as path dependence of the solution. The UDEC user's manual proposed two alternative forms of velocity proportional damping (Itasca Consulting, 2014):

- Adaptive global damping (auto damping); and
- Local damping

In local damping, the viscous damping coefficient applied at a node of the mesh/grid is defined as a linear function of the sum of unbalanced forces at that node. With this form of damping, the body forces due to damping vanishes as the model approaches equilibrium. Body forces associated with conventional damping were found to have an effect on failure pattern. However, that effect is significantly reduced with local damping (Itasca Consulting, 2014).

Without damping, rocks would oscillate indefinitely when subjected to dynamic or seismic events. These events can have several causes such as slip on natural faults or mining induced failure of brittle rocks. The material damping in rocks and soils is known to be hysteresis based and frequency independent. The amount of damping necessary to remove all oscillations in the system is known as critical damping. Damping in geological system material is usually 2% and 5% (Raffaldi, 2015)

A sensitivity analysis was carried out to determine the appropriate value of damping to be used. In the damping sensitivity analysis, the following permutations were examined:

- Damping D=0.3 and velocity=0.01 m/s (base case)
- Damping D=0.3 and velocity=0.05 m/s
- Damping D=0.8 and velocity=0.05 m/s

The results of the damping sensitivity analysis are presented in form of average pillar stress versus axial strain in Figure 26. The key results are:

- The peak pillar strength of the model with high damping and high velocity is slightly higher than the base case but lower than that of the model with similar loading velocity but lower damping.
- All the three graphs are very similar over the pre-peak parts of the curves. However, the post peak behaviour differs remarkably
- The model with D=0.8 and velocity=0.05 m/s exhibits significant strain hardening beyond the peak pillar strength compared to the model loaded with a similar velocity but lower damping.

Based on these findings, in order to obtain optimum results a low damping value of 0.3 was proposed and will be used in the analyses that follow.

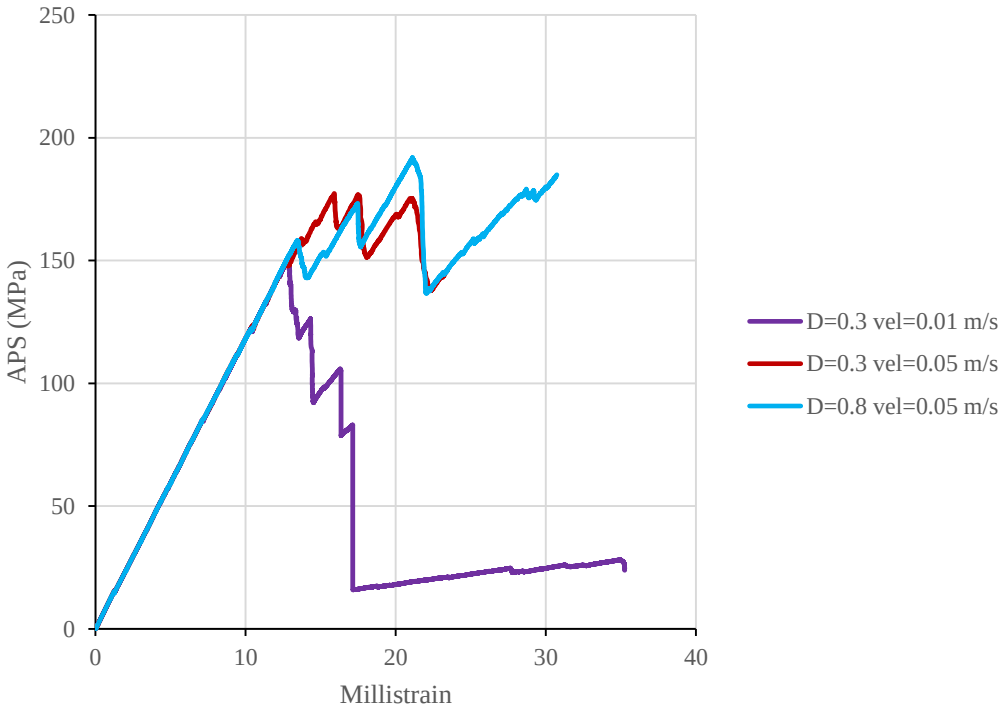


Figure 26: Damping sensitivity analysis: Average pillar stress vs. pillar strain curve

3.4. Input material parameters

3.4.1. Intact rock calibration

The intact rock in this analysis was modelled as a voronoi tessellation. The micro-properties (strength and deformation) assigned to the contacts of the voronoi cells were calibrated against macroscopic responses of the rock measured in the laboratory. The joint stiffness used in UDEC is expressed in stress-per-distance-units (Itasca Consulting, 2014) therefore all stiffness value were converted to and are quoted in these units. The contact parameters that were calibrated are as follows:

- Normal stiffness (kn) (GPa/m)
- Normal to shear stiffness ratio (kn/ks)
- Peak cohesion (cp) (MPa)
- Residual cohesion (cr) (MPa)
- Peak tensile strength (Tp) (MPa)
- Residual tensile strength (Tr) (MPa)
- Peak friction angle (ϕp) (^{o})
- Residual friction angle (ϕr) (^{o})

For simplicity, the residual cohesion and tensile strength are often considered to be zero (Kazerani and Zhao, 2010; Gao, 2013; Ghazvinian, et al. 2014). Table 10 shows the calibrated voronoi contact properties.

Table 11 lists the voronoi block properties. The voronoi blocks were modelled as elastic and therefore only the density, Young's modulus and poisson's ratio, directly measured in the lab, were specified. Likewise, the steel ring platens around the pillar were also modelled as an elastic continuum. General steel properties after Preston (2014) were assigned. The assigned values are also listed in Table 11.

Table 10: Voronoi contact parameters

Parameter	Value
Cohesion (MPa)	50
Residual Cohesion (MPa)	0
Friction (°)	0
Residual Friction Angle (°)	25
Tensile Strength (MPa)	5
Residual tensile strength (MPa)	0
Normal Stiffness (GPa/m)	1500
Shear Stiffness (GPa/m)	600

Table 11: Steel ring platens and voronoi block material parameters

Parameter	Steel ring platens	Voronoi block
Density (kg/m^3)	7600	3300
Elastic Modulus (GPa)	200	150
Poisson's Ratio	0.25	0.23

3.4.2. Joint material properties

The Mohr-Coulomb constitutive model was used since the version 5.0 of UDEC used in this study does not support more sophisticated constitutive models such as Barton-Bandis. However, an apparent cohesion and friction angle were derived from fitting a curve to a Barton-Bandis joint model, which includes the core logging joint information data and scaling of the Joint Wall Compressive Strength (JCS) and Joint Roughness Coefficient (JRC). The maximum confinement was taken equal to a typical peak average pillar strength of 160 MPa and the scaling length was assumed equal to the average joint length of 14 m. This resulted in equivalent Mohr-Coulomb properties for the joint of 0.5 MPa and 26° for the apparent joint cohesion and friction angle, respectively. These results are close to the results obtained from the lab tests with a cohesion and frictional angle of 0.2 MPa and 23° respectively.

The normal and shear stiffness of the joints proved more complicated to assign because UDEC tends to use the stiffness as both material property and numerical parameter. For instance, the stiffness is also used to calculate modelling parameters such as the time step. Large contrasts

in stiffness often results in much longer time step, hence longer simulations. Therefore, although the normal stiffness of pre-existing joints is known to be in the order of a GPa and the shear stiffness roughly one fifth of the normal stiffness, applying these values in the model proved simply impractical as it led to lengthy runtimes. Instead, recommendations in the UDEC user's manual (Itasca Consulting, 2014) were followed to arrive at an optimum stiffness for the modelled joints without compromising the overall behaviour. The joint mean shear strength properties used in the simulation are summarized in Table 12

Table 12: Joint mean strength properties

Pre-existing joint material properties	**value**
Cohesion (MPa)	0.2
Friction angle (°)	23
Normal stiffness (GPa/m)	1000
Shear stiffness (GPa/m)	100

3.5. Summary

Data collected from the mine and obtained from previous work done at Mine X by SRK Consulting proved useful towards the process of the numerical modelling of pillars at P_C. Data processing was done and obtained information was used as inputs into the numerical models. The process of UDEC modelling was carried out after conducting sensitivity analysis on loading rate and mechanical damping that have an effect on results. The results obtained from the numerical analysis are outlined in Chapter 4.

Chapter 4: Results and analysis

Three sets of models with intact rock modelled using the voronoi tessellation were run. These include the intact pillars, jointed pillars with joints from DFN 1 and jointed pillars with joints from DFN 2. To understand the effect of joints on pillars, the results from the jointed and intact pillar models will be compared.

Each set of models comprised of pillars of different widths that is 2 m, 4 m and 6 m pillars. Pillars of different sizes are expected to behave differently when subjected to the same stress conditions and similar jointing networks. Results from models of different pillar sizes will be evaluated to understand different characteristics exhibited.

The use of voronoi is still a subject of research. A 4 m pillar modelled as an intact rock was run. An understanding of the effect of voronoi will be obtained from comparing results of the model with and without voronoi.

4.1. Results

4.1.1. Intact pillar models

Intact 4 m pillar models were considered the base case scenario as P_C is mining 4 m pillars. Here the validity of the voronoi will be accessed in the absence of the complexity of the pre-existing joints.

Four-meter pillars

Figure 27 shows the average pillar stress versus axial displacement curve for the 4 m intact pillar. The intact pillar model indicated a peak strength of about 450 MPa. According to Hoek and Brown (1980), the UCS of a specimen decreases with increase in specimen size. The decrease in strength is mainly due to the increase in existing micro-fractures as specimen size increases. However, as pillar width to height ratio increases, pillar strength increases (Mathey, 2015). As expected, the peak strength of the pillar is considerably higher than the UCS recorded in the lab for an intact rock specimen. The high confinement in the 4 m pillar and the absence of micro fractures in the model could have contributed to the 450 MPa peak strength recorded. Figure 28 shows the failure mode of the intact pillar at the indicated stress/displacement levels. The corresponding displacement contours are shown in Figure 29.

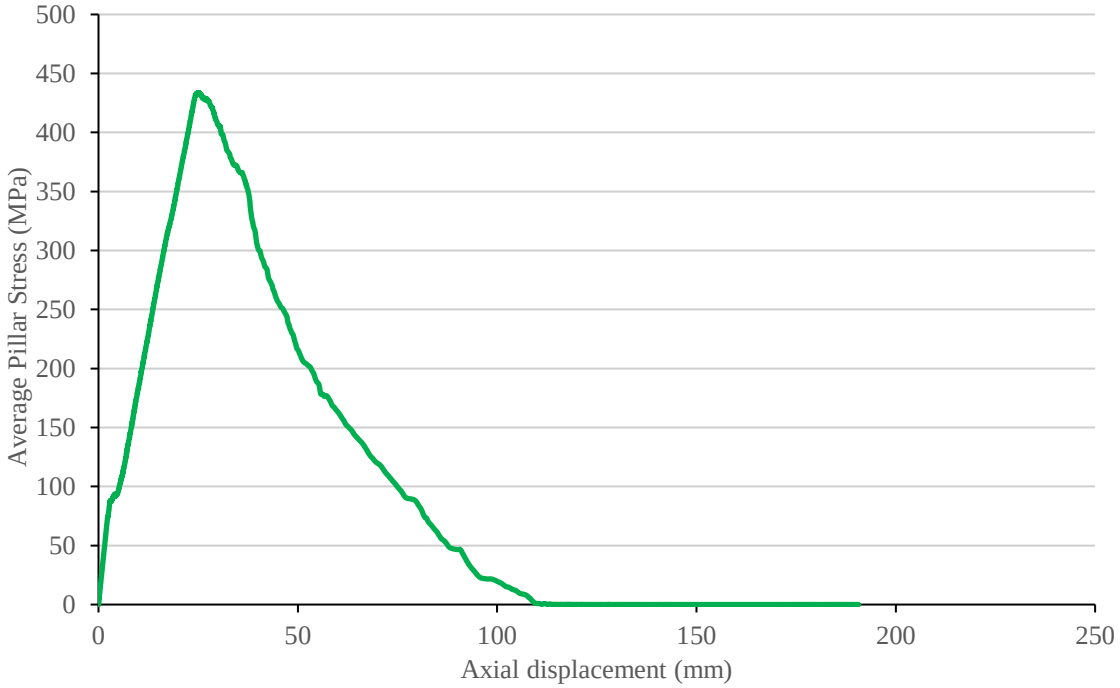


Figure 27: Average pillar stress versus axial displacement curve for the intact 4 m pillar

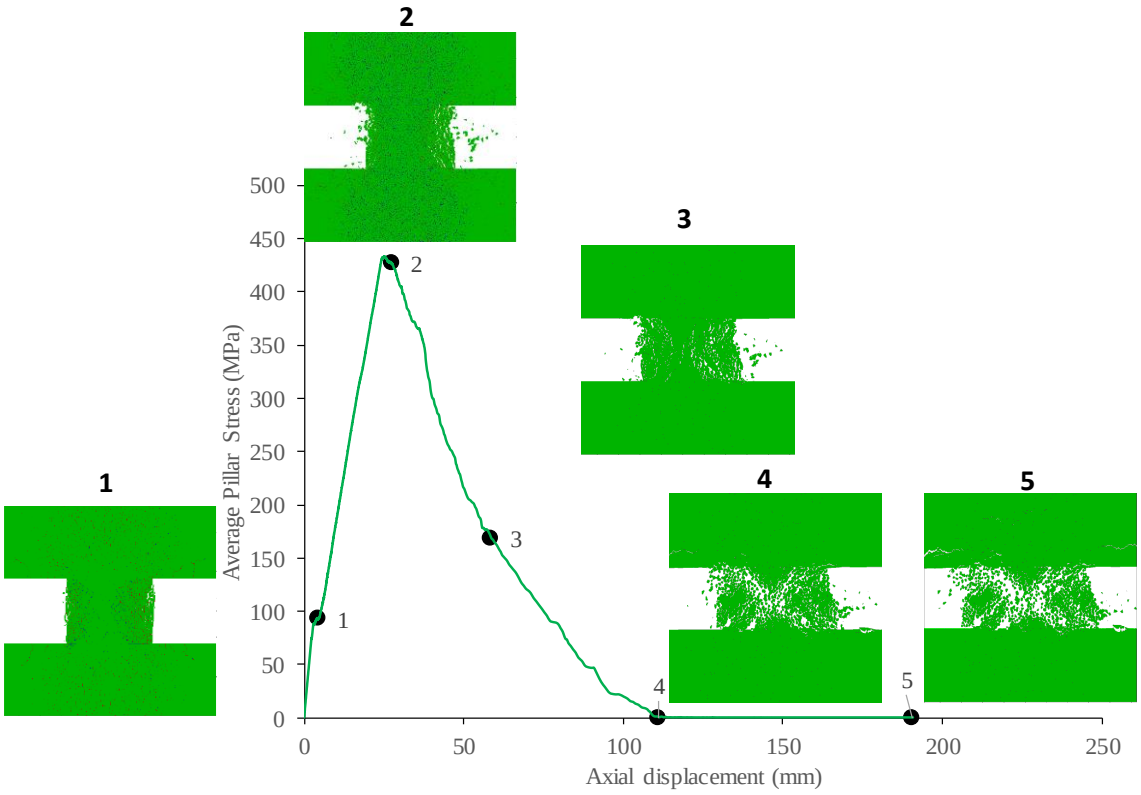


Figure 28: Average pillar stress versus axial displacement curve and failure mode for the intact 4 m pillar

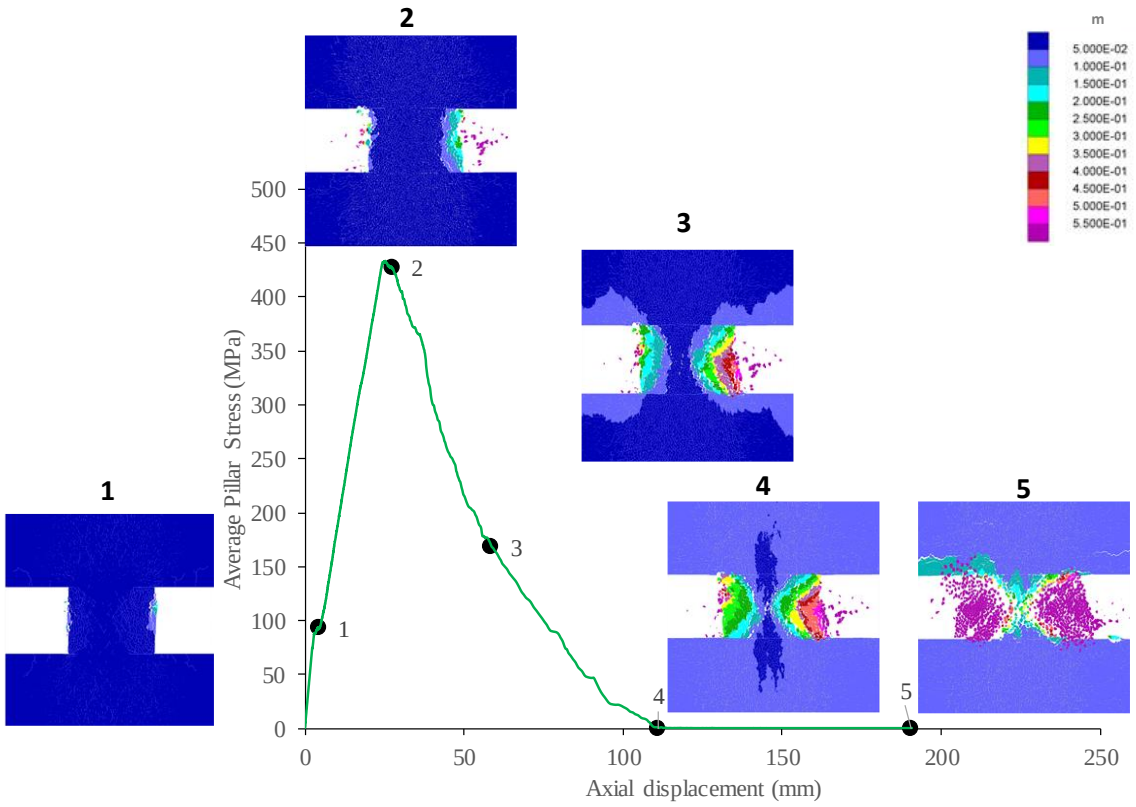


Figure 29: Average pillar stress versus axial displacement curve and displacement contours for the intact 4 m pillar.

Stage 1 of the curve shows the initial stages of spalling which resulted in a sudden drop in pillar strength. Pillar strength was regained as loading increased. The obtained results show a failure mechanism that is in line with the pillar failure stages developed by Roberts, et al. (1998). The model pillar failure modes can be related to Roberts, et al. (1998) theory in the way shown in Table 13.

Table 13: Failure mechanisms

Model stage	Description	Roberts' stage	Roberts, et al. (1998) description
1	Spalling in the sidewalls with little bulging	2	Minor spalling and short axial fractures
2	Creation of micro structures extends towards the pillar center.	3 - 4	Substantial spalling, axial fracture length shorter than the half pillar height
3	Hour glass shape forms, drop in pillar strength	4	Continuous open fractures cutting towards pillar core. Beginning of formation of the hourglass shape
4	Drop in pillr strength continues, hour glass shape significantly defined	5 - 6	Large continuous open fractures, well developed hour-glass shape
5	Pillar collapses	6	Failed pillar by either extreme hour-glass shape or necking

Two-meter pillars

Figure 30 shows an average pillar stress versus axial displacement curve for an intact 2 m pillar model. The results show a peak strength of 270 MPa, which is just above half the strength of the 4 m intact pillar. Strain hardening is indicated which is expected for a slender pillar with no fractures. Figure 31 and Figure 32 show the failure mechanism and displacement contours at every selected point along the average pillar stress versus axial displacement curve respectively. The progression of the stresses is shown in Figure 33.

At stage 2, the 2 m pillar lost its strength when the open fractures extended toward the pillar centre. Spalling continued as the pillar continued to harden forming an hourglass shape. The pillar centre remains highly stressed as the pillar is strain hardening. The final model was obtained after a contact overlap distance of 0.2 m was reached.

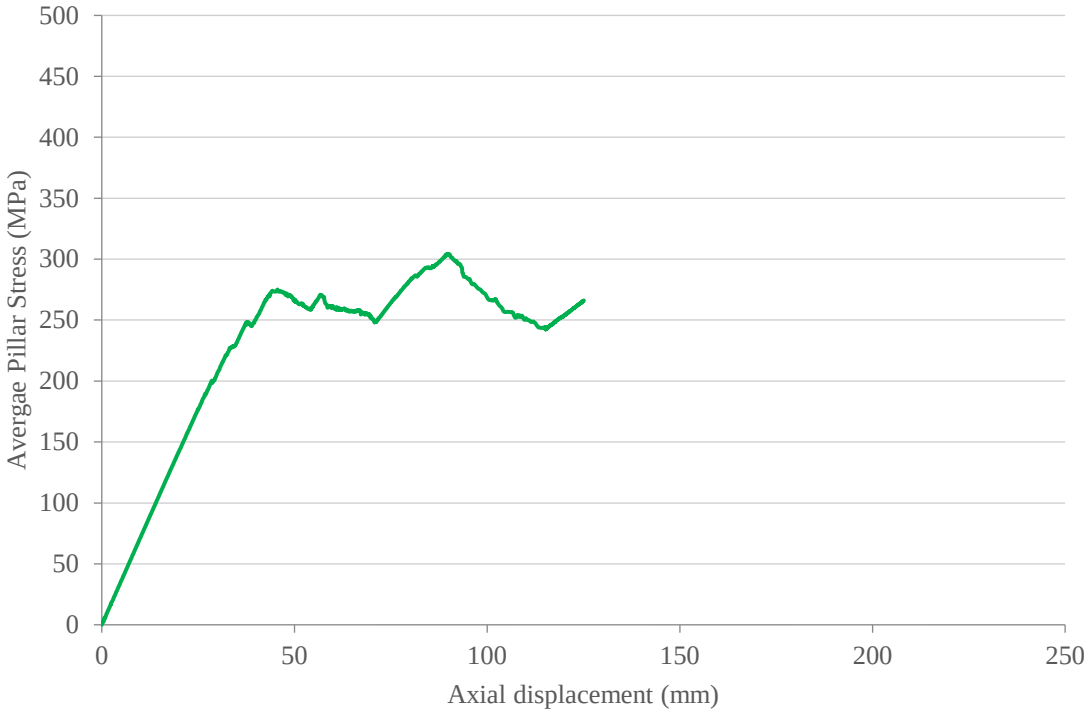


Figure 30: Average pillar stress versus axial displacement curve for the intact 2 m pillar

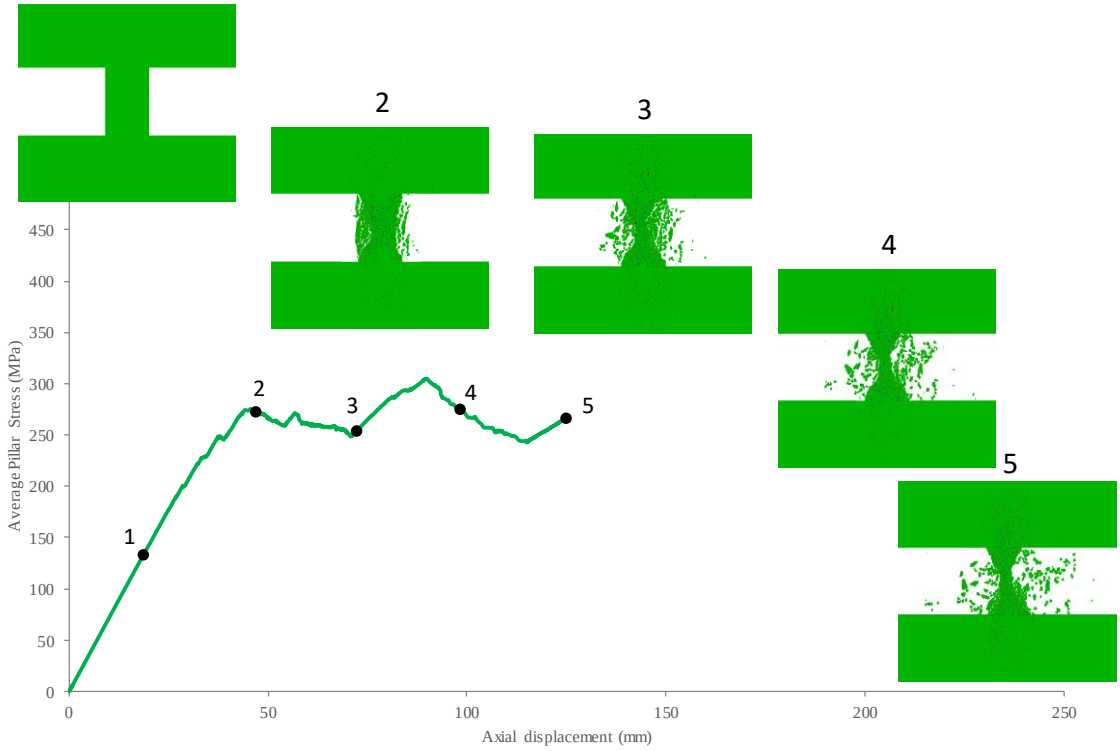


Figure 31: Average pillar stress versus axial displacement curve and failure mode for a 2 m intact pillar

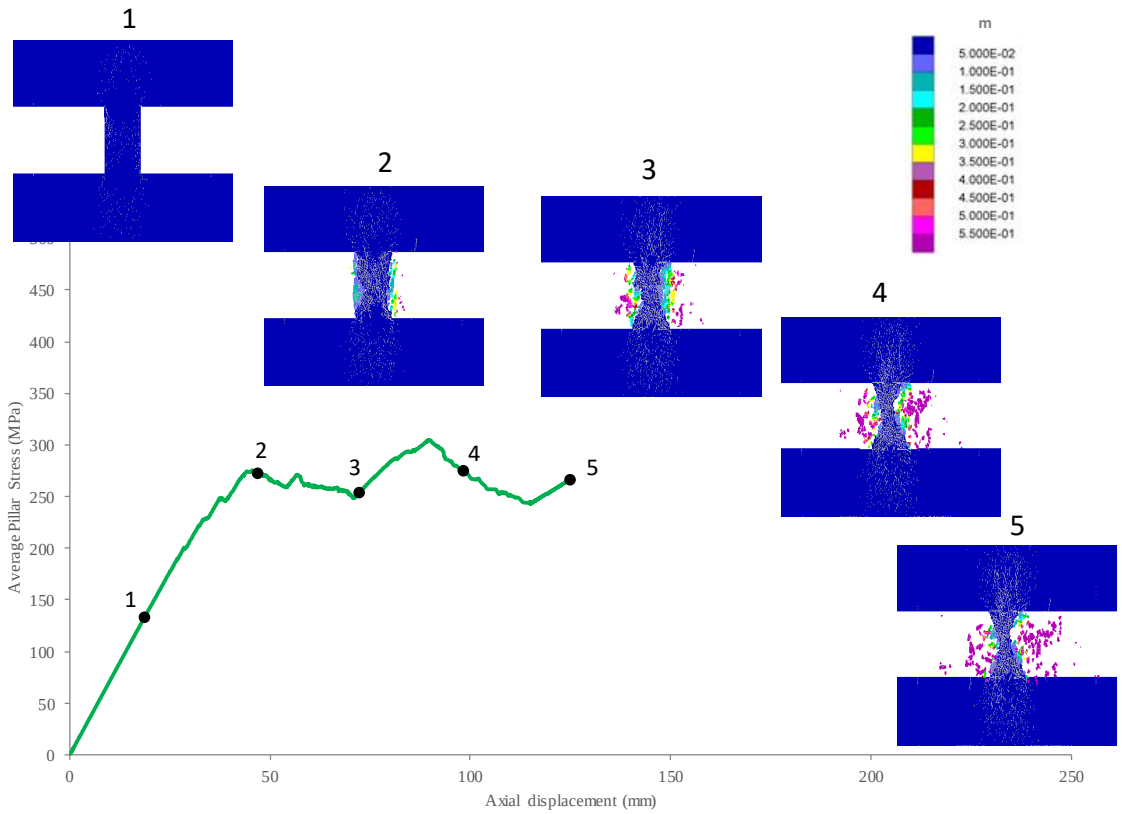


Figure 32: Average pillar stress versus axial displacement curve and displacement contours for the intact 2 m pillar

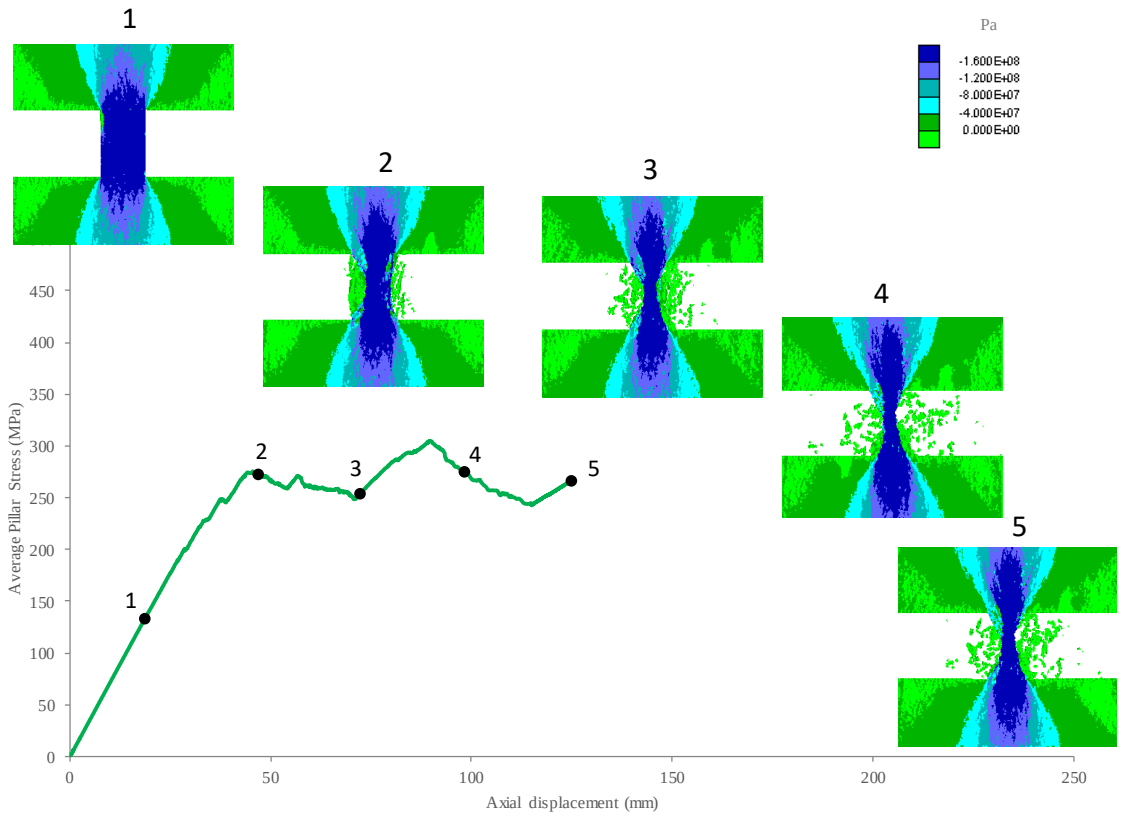


Figure 33: Average pillar stress versus axial displacement curve progression of stress for the intact 2 m pillar

Six-meter pillars

The average pillar stress versus axial displacement curve for a 6 m intact pillar is shown in Figure 34. The 6 m pillar model ran up to a point where the contact overlap was too great for it to continue running. Although the pillar peak strength had not been reached yet at this point, the model running had to be stopped. Figure 34 does not show the peak strength of the pillar but gives an indication that the pillar strength of the 6 m pillar is greater than 750 MPa. The post peak behaviour of the 6 m pillar could not be determined from this model.

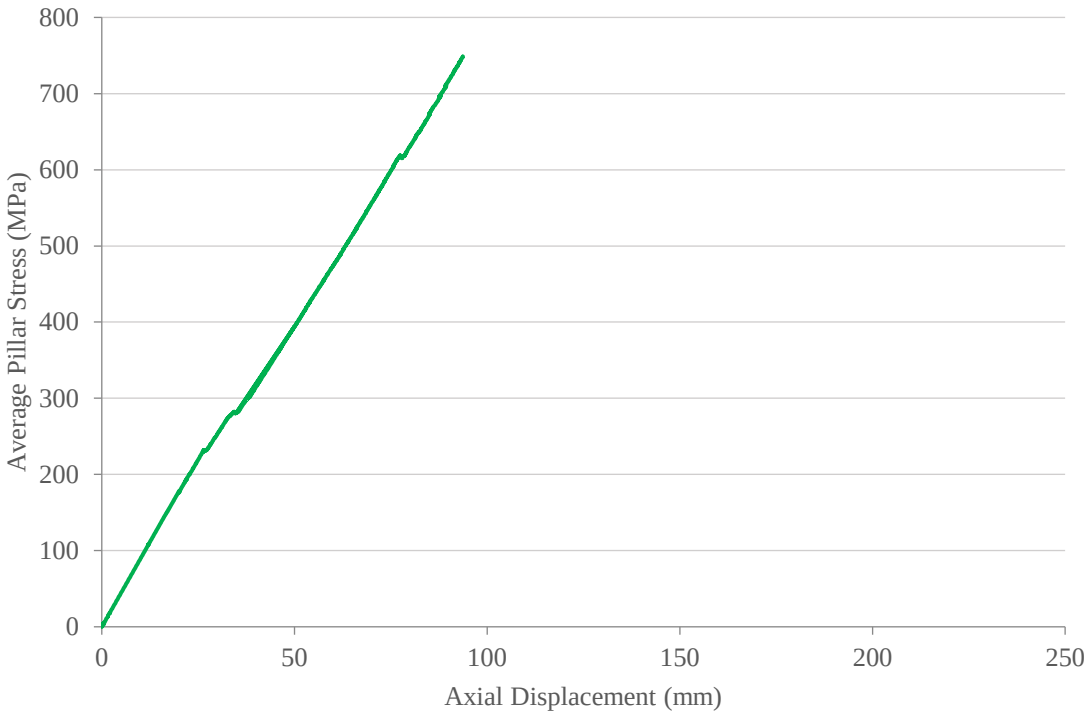


Figure 34: Average pillar stress versus axial displacement curve for the intact 6 m pillar

Figure 35 shows the progression of cracks on the 6 m pillar. Figure 36 and Figure 37 show the displacement contours and progression of stresses respectively.

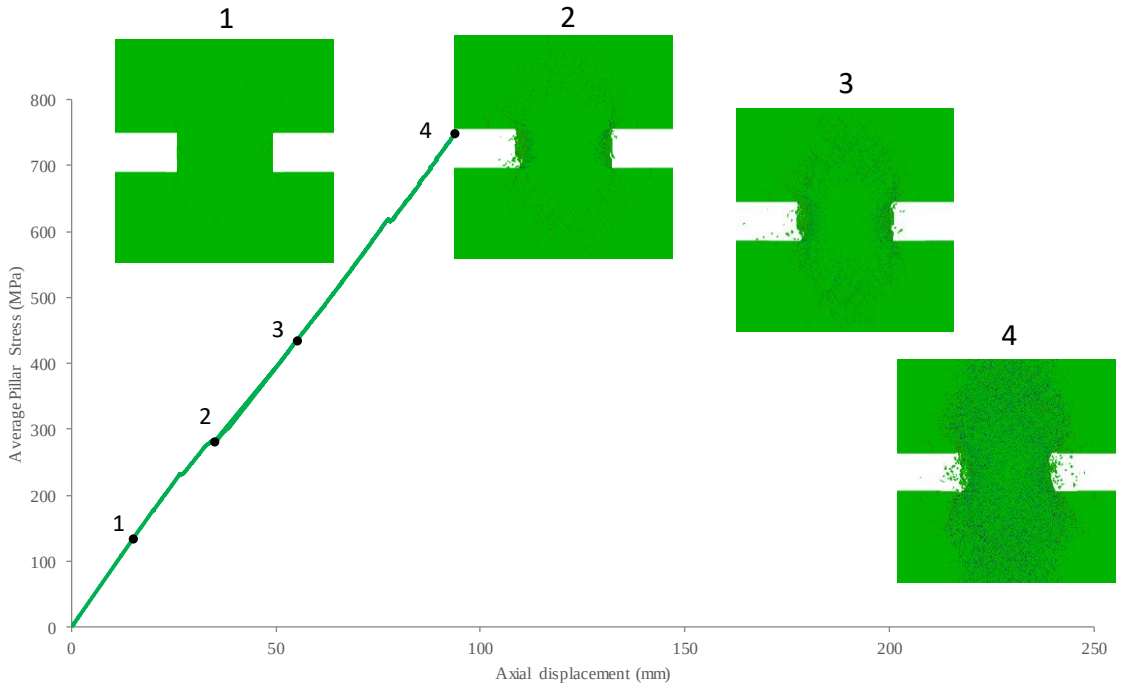


Figure 35: Average pillar stress versus axial displacement curve and failure mode for the intact 6 m pillar

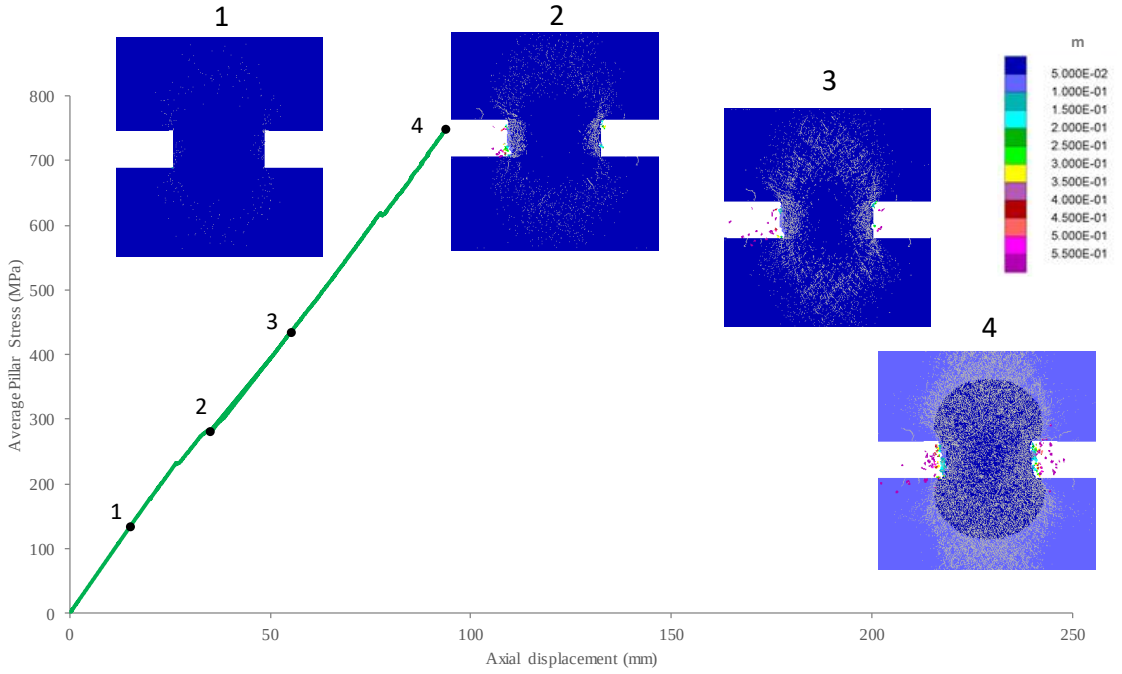


Figure 36: Average pillar stress versus axial displacement curve and displacement contours for the intact 6 m pillar

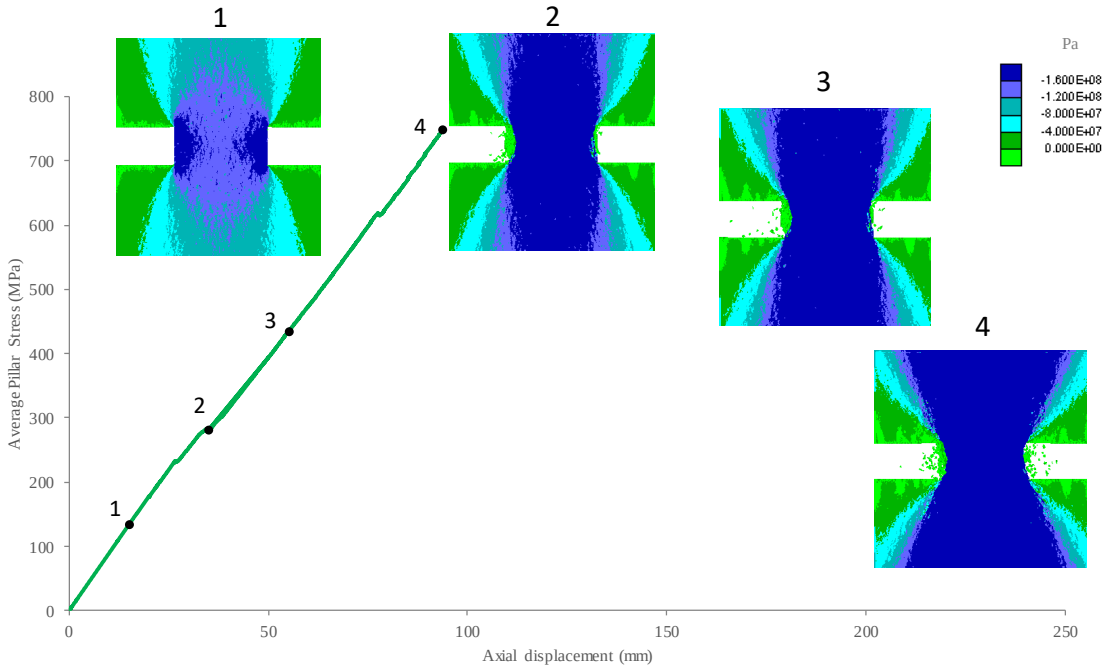


Figure 37: Average pillar stress versus axial displacement curve and displacement contours for the intact 6 m pillar

4.1.2. Jointed pillar model DFN 1

Two meter pillars

Figure 38 shows the average pillar stress versus axial displacement curve for a 2 m pillar with joints from DFN1 indicating a peak strength of 55 MPa. The corresponding failure mechanism and cracking due to the jointing is also shown. The stress and displacement contours at different positions along the average pillar stress versus axial displacement curve are presented in Figure 39 and Figure 40 respectively.

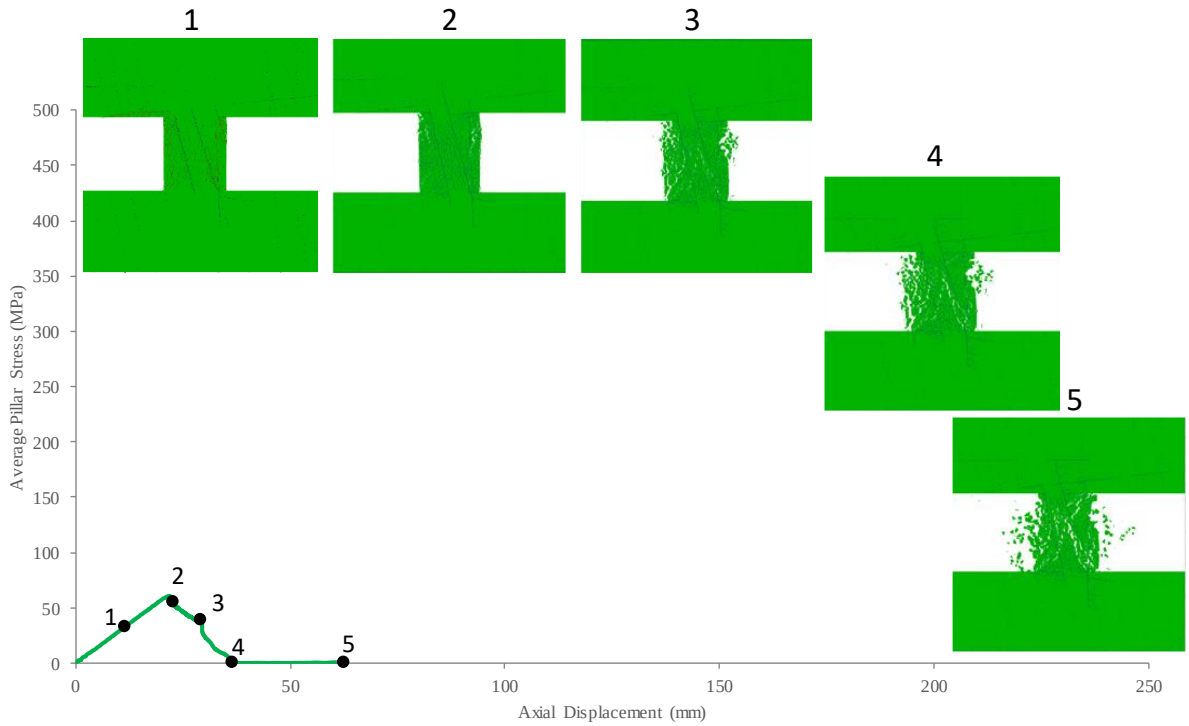


Figure 38: Average pillar stress versus axial displacement curve and associated failure mechanism for 2m wide pillar model for DFN 1

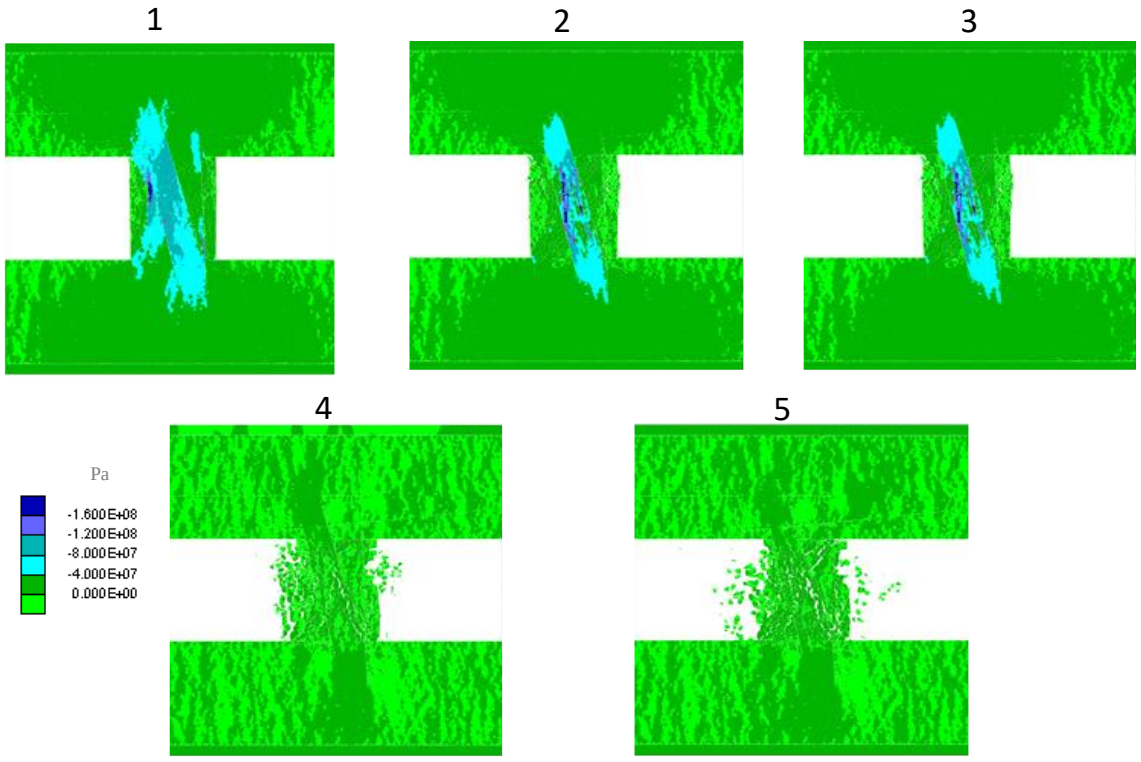


Figure 39: Progression of stress for 2m wide jointed pillar model for DFN 1

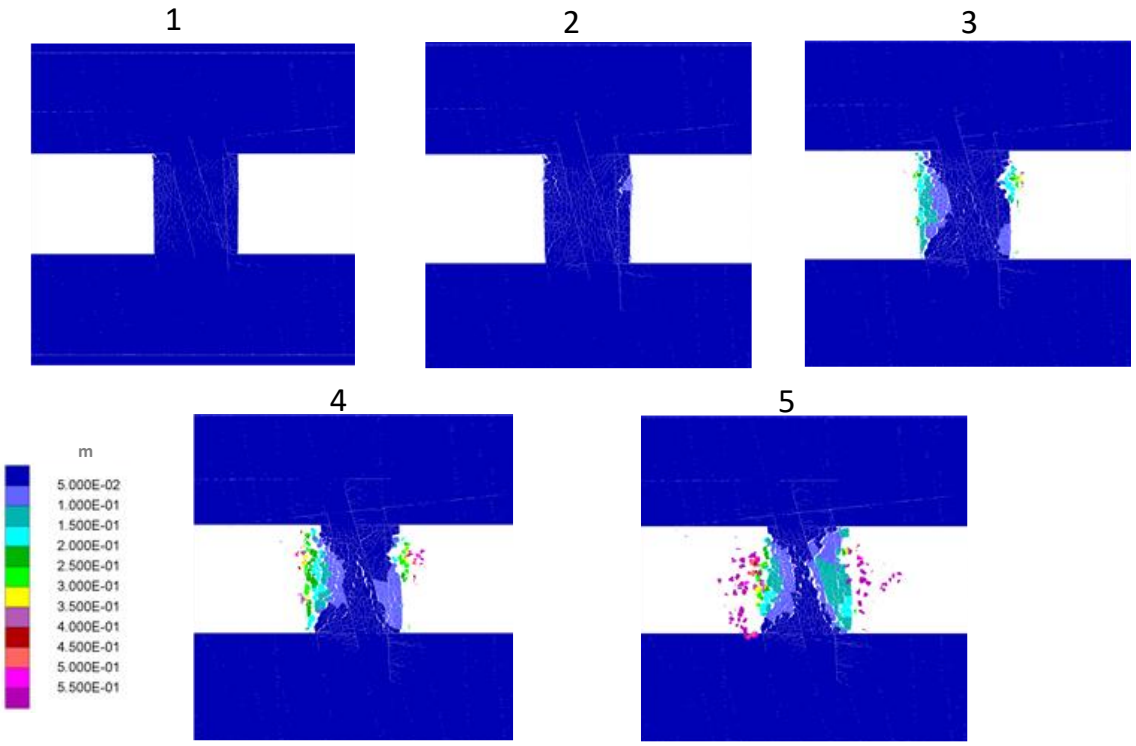


Figure 40: Progression of total displacement for 2m wide jointed pillar model for DFN 1

For slender pillars, spalling on the pillar walls and displacement on the joints within the pillar indicate that the peak strength has been reached even though no significant bulging occurs.

As displacement increases, so does spalling on the pillar sides. If unsupported, slabs and rock blocks can be released from the pillar walls. The stress concentrates in the pillar centre as a result of pillar sidewall spalling. This stress concentration causes splitting and development of tensile fractures oriented almost in the direction of loading. The pillar has then lost all strength when tensile fracturing in the pillar centre become visible.

Four meter pillars

Figure 41 shows the stress displacement curve for a 4 m pillar with DFN 1. Fracturing within the pillar at the position indicated on the curve is also presented. Figure 42 and Figure 43 show stress and displacement contours respectively.

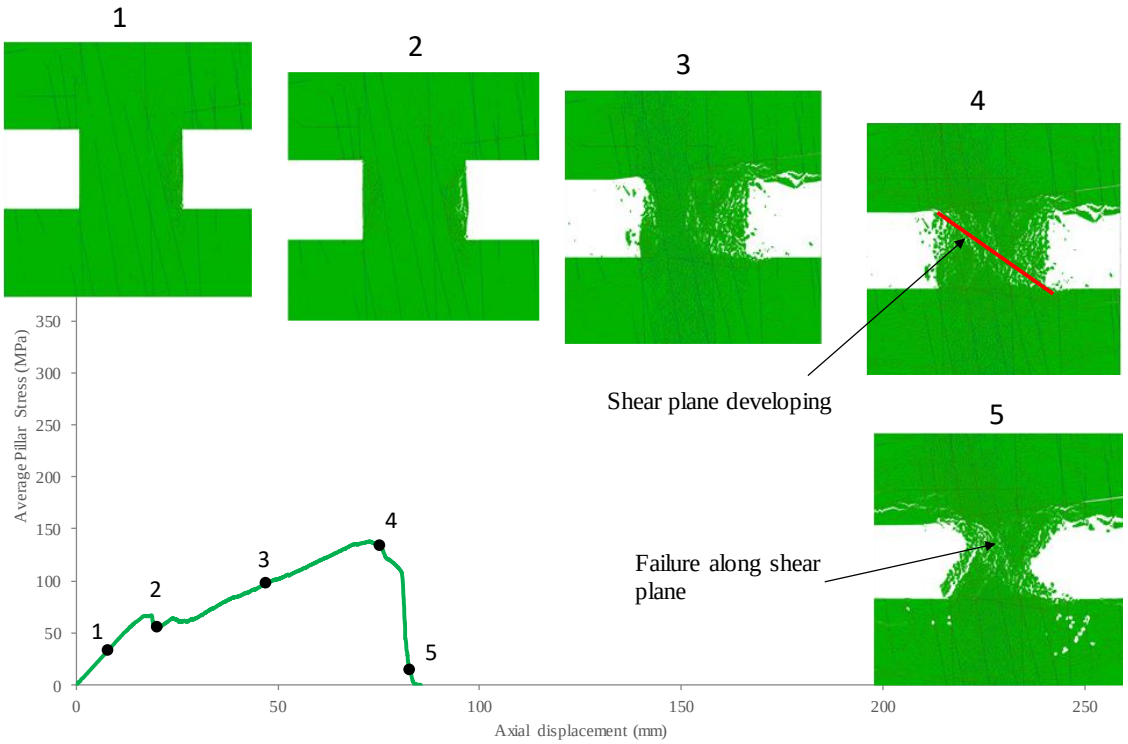


Figure 41: Average pillar stress versus axial displacement curve and associated failure mechanism for 4 m pillar for DFN 1

The response of the 4 m wide jointed pillars is characterized by strain hardening. Intensive spalling and opening up of tensile cracks on the pillar walls occurs at an average pillar stress of 65 MPa. This resulted in the sudden drop of confinement within the pillar corresponding with a drop in pillar strength.

Spalling and release of rock blocks on the pillar walls continues with further displacements. However due to the relatively large pillar size, confinement is regained and strain hardening occurs. The continual spalling and tensile fracturing cause a gradual release of confinement and the activation of more joints.

Ultimately, the tensile fractures connect to form a shear plane. At that stage, the pillar has already failed and has lost its strength.

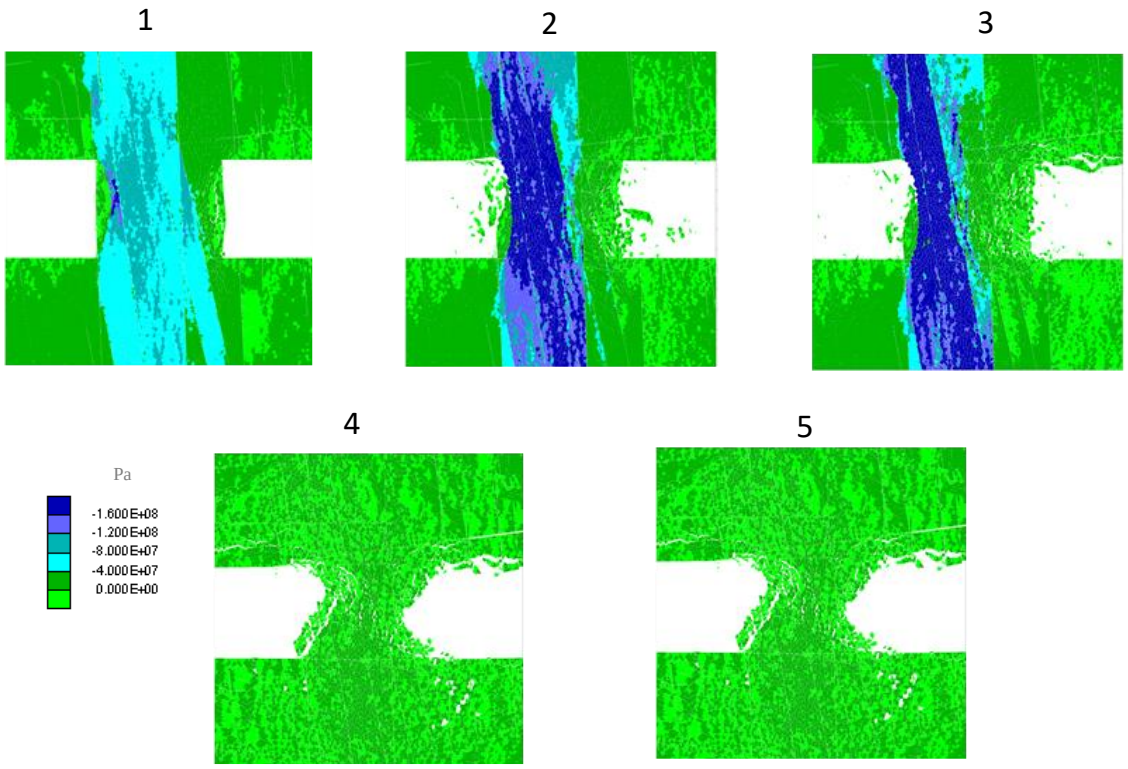


Figure 42: Progression of stresses for 4 m wide jointed pillar model for DFN 1

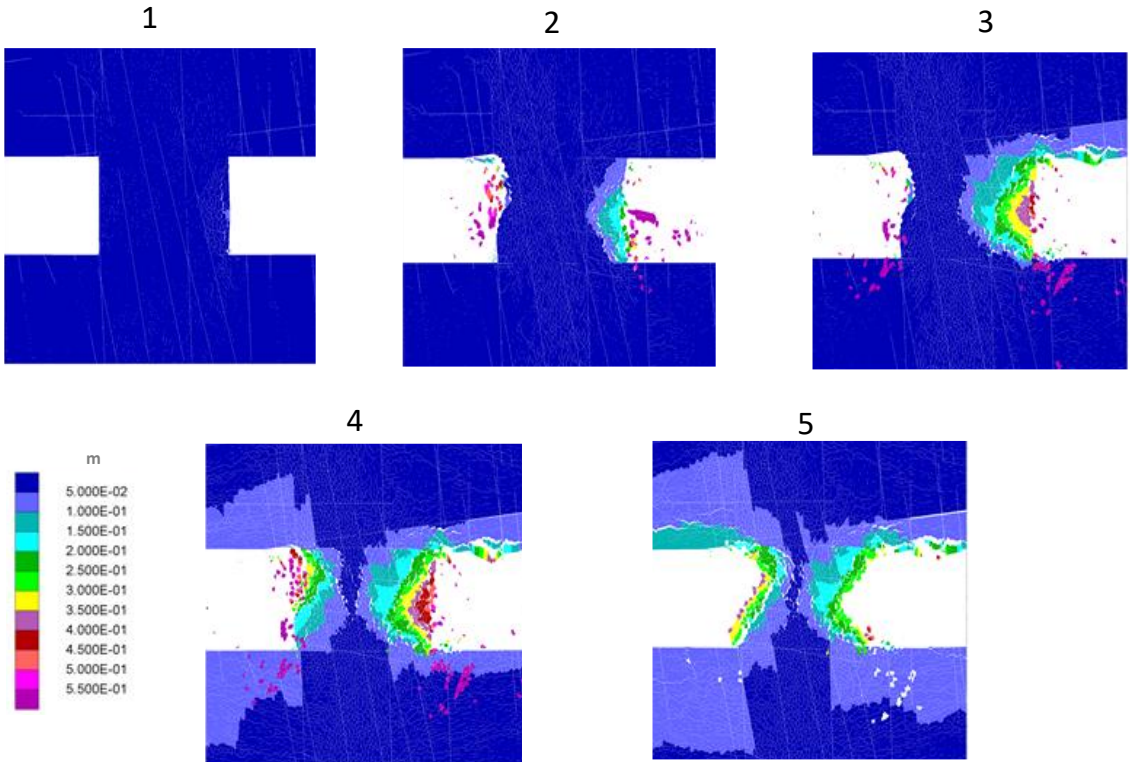


Figure 43: Progression of total displacement for 4 m wide jointed pillar model for DFN 1

Six meter pillars

Figure 44 shows the average pillar stress versus axial displacement curve for a jointed 6 m pillar together with the corresponding fracture propagation at each point. Figure 45 and Figure 46 show the stresses and total displacement contours at each point respectively.

Spalling and slabbing of the 6 m pillar starts at about the same average pillar strength of 65 MPa as with the 2 m and 4 m jointed pillars. However, in the case of the 6 m pillar there is no drop in pillar strength. As pillar width increases axial displacement also increase.

As the vertical displacements increase, the pillar strength increases up to a peak strength of about 265 MPa. The shape of the stress/displacement curve between stage 2 and 3 suggests that the pillar might have punched through the hanging-wall at peak strength causing damage above the pillar in the hanging-wall that can be seen in stage 4. However, no massive hanging-wall failure was recorded. The stepwise pillar failure from stage 3 to 4 suggest continual pillar weakening through slip along the joints.

Ultimately, complete failure of the pillar occurs in form of a shear plane as a result of intense spalling on the pillar walls and failure along pre-existing joints.

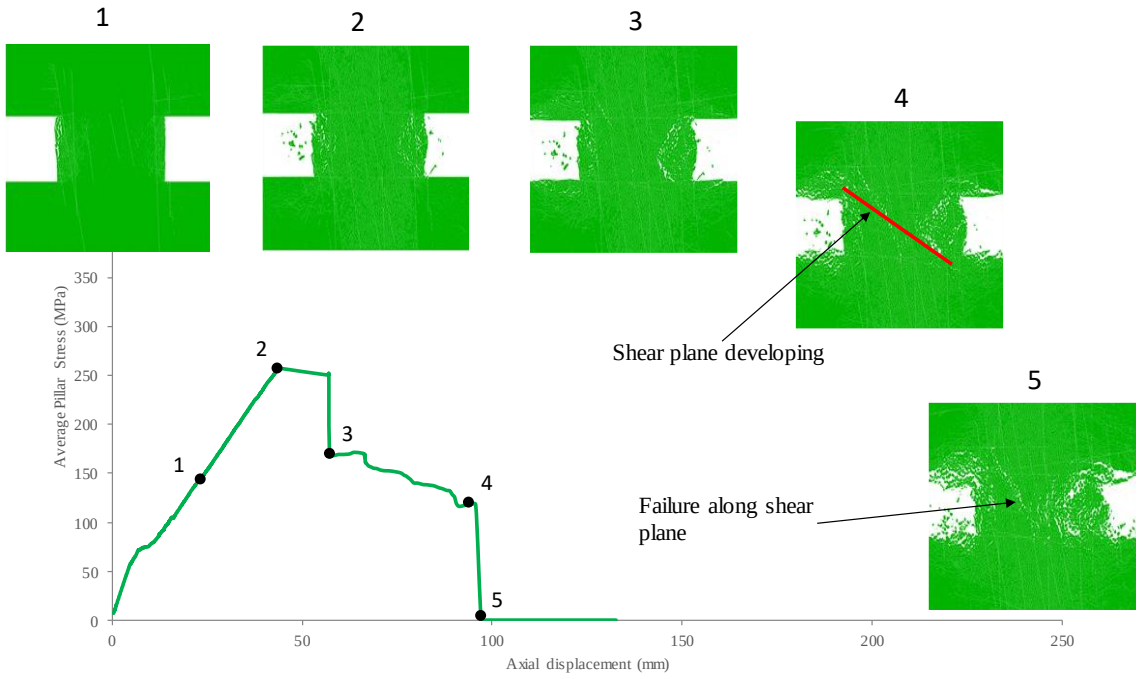


Figure 44: Average pillar stress versus axial displacement curve and associated failure mechanism for 6 m pillar for DFN 1

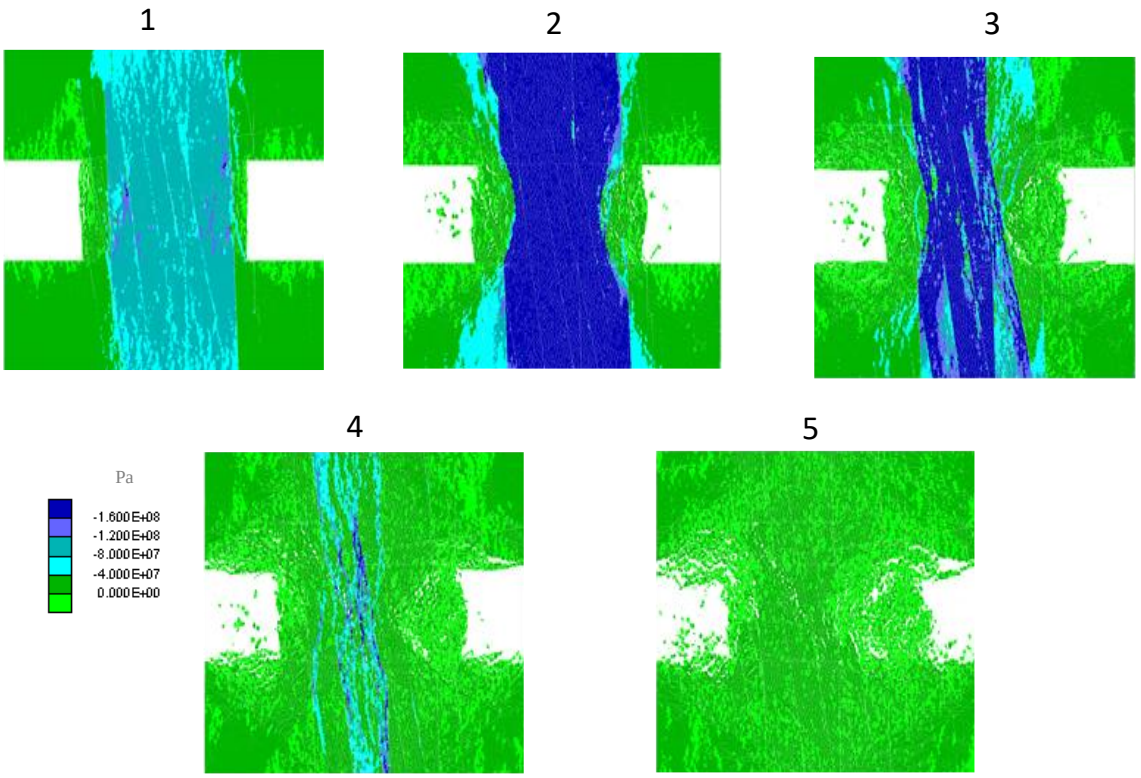


Figure 45: Progression of stresses for 6 m wide jointed pillar model for DFN 1

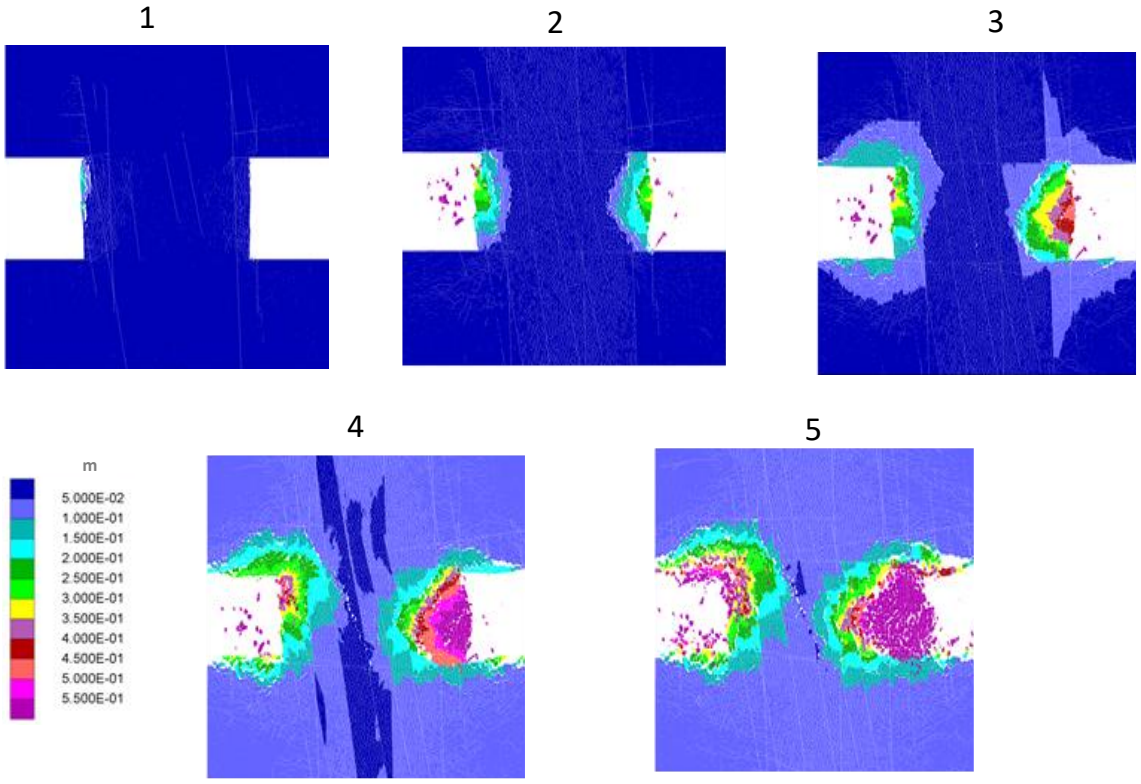


Figure 46: Progression of total displacement for 6 m wide jointed pillar model for DFN 1

4.1.3. Jointed pillar model DFN 2

Two meter pillars

The average pillar stress vs. displacement curve for a 2 m wide pillar with DFN 2 is presented in Figure 47. Fracturing within the pillar at the positions indicated on the curve is also presented. Figure 48 and Figure 49 show stress and total displacement contours, respectively.

The peak pillar strength of about 65 MPa occurs when movement along the joints within the pillar starts. The pillar strength drops as a result of this but tends to stabilize afterwards. Extensive spalling on the pillar walls and tensile fracturing in the pillar centre causes total failure of the pillar.

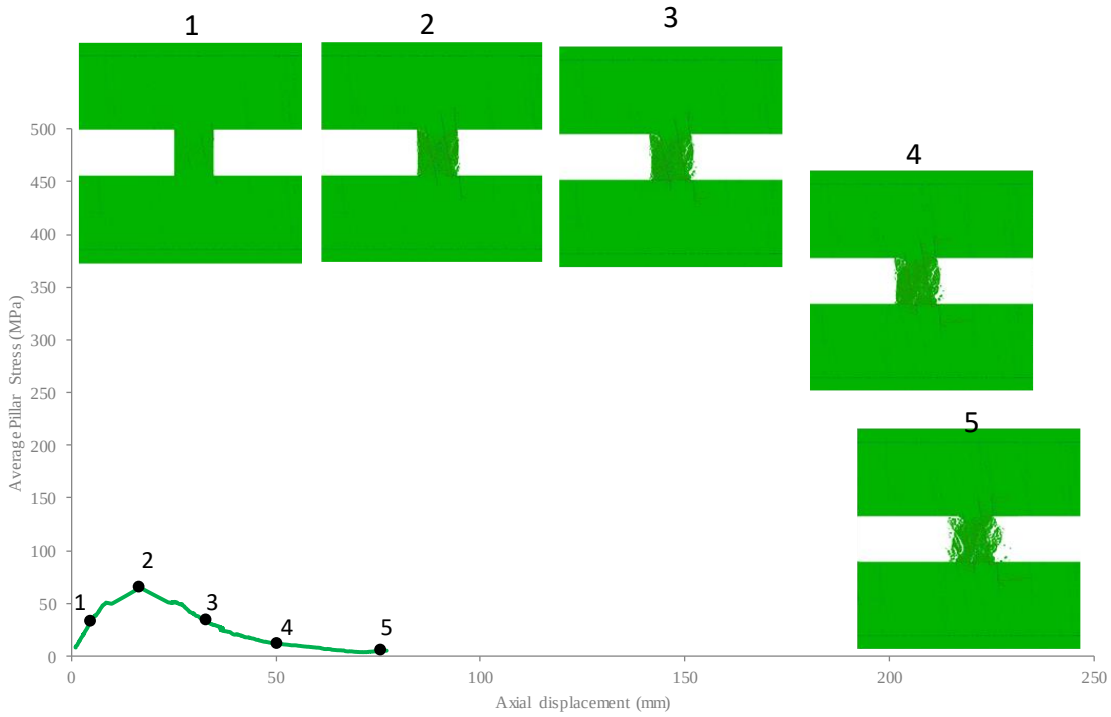


Figure 47: Average pillar stress versus axial displacement curve and associated failure mechanism for 2 m pillar for DFN 2

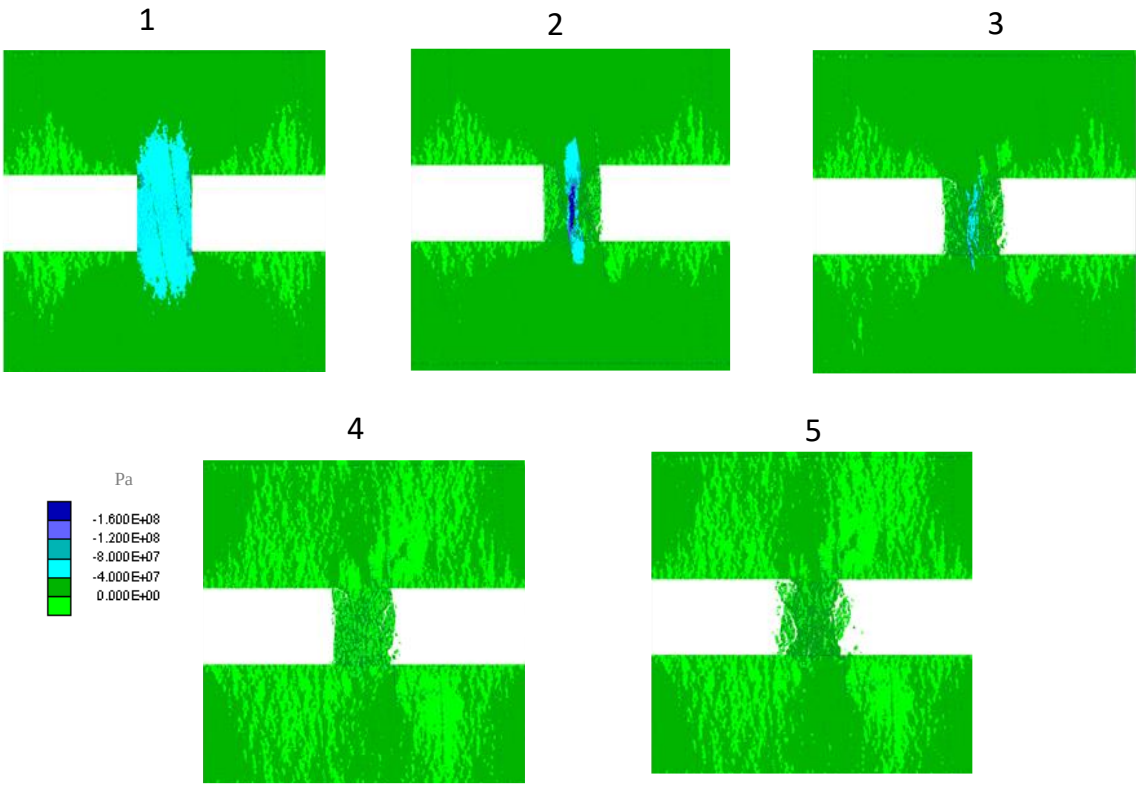


Figure 48: Progression of stresses for 2 m wide jointed pillar model for DFN 2

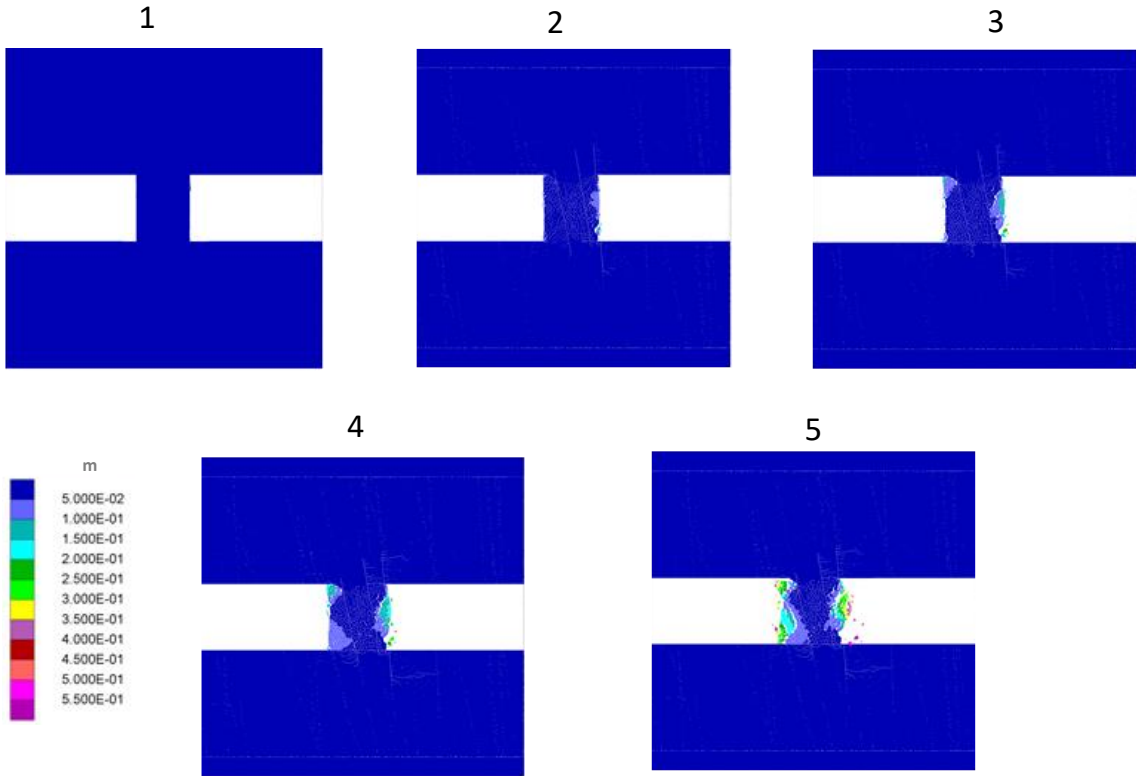


Figure 49: Progression of total displacement for 2 m wide jointed pillar model for DFN 2

Four meter pillars

The average pillar stress vs. displacement curve for a 4 m wide pillar with DFN 2 is presented in Figure 50. Fracturing within the pillar at the positions indicated on the curve is also presented. Figure 51 and Figure 52 show stress and total displacement contours, respectively.

Similar to 4 m pillars with DFN 1, slabbing starts at a pillar strength of about 65 MPa. The reduction in confinement as the pillar walls spall results in a sudden drop in pillar strength. Due to the relatively large pillar width, the pillar regains its confinement.

Pillar collapse occurs in form of shear at a pillar peak strength of 110 MPa. Slabbing continues until the pillar totally loses its strength at stage 5.

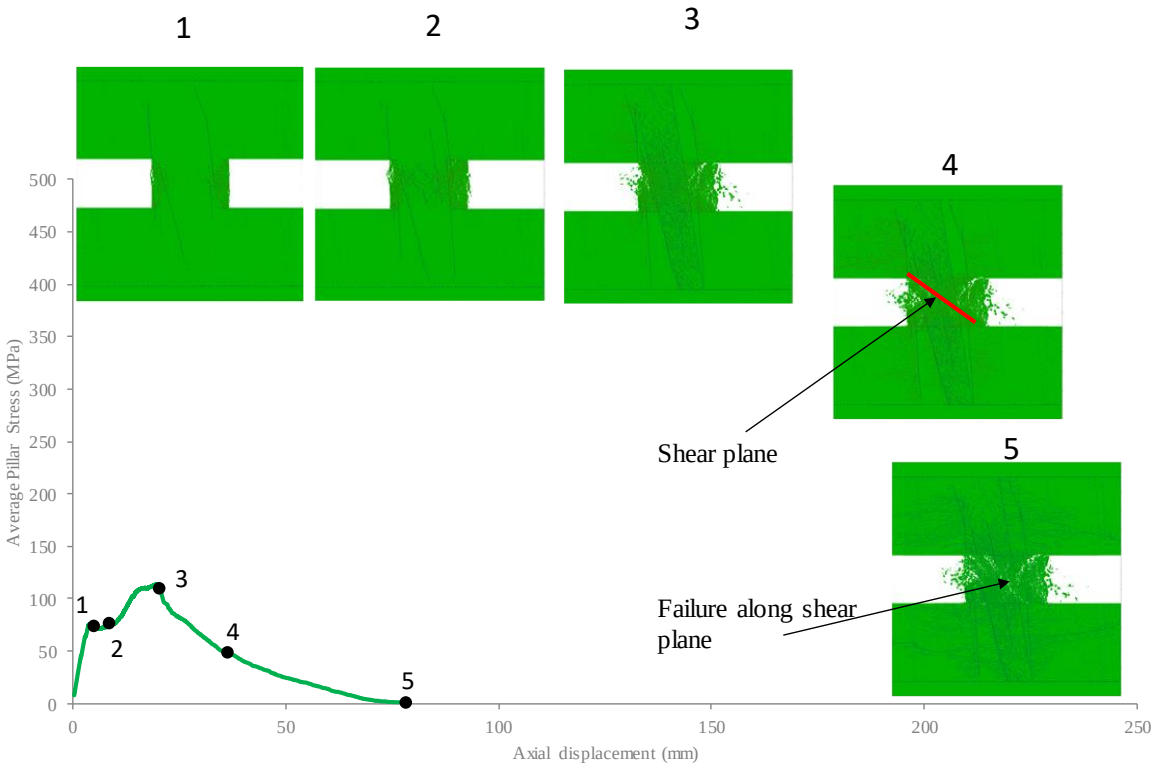


Figure 50: Average pillar stress versus axial displacement curve and associated failure mechanism for 4 m pillar for DFN 2

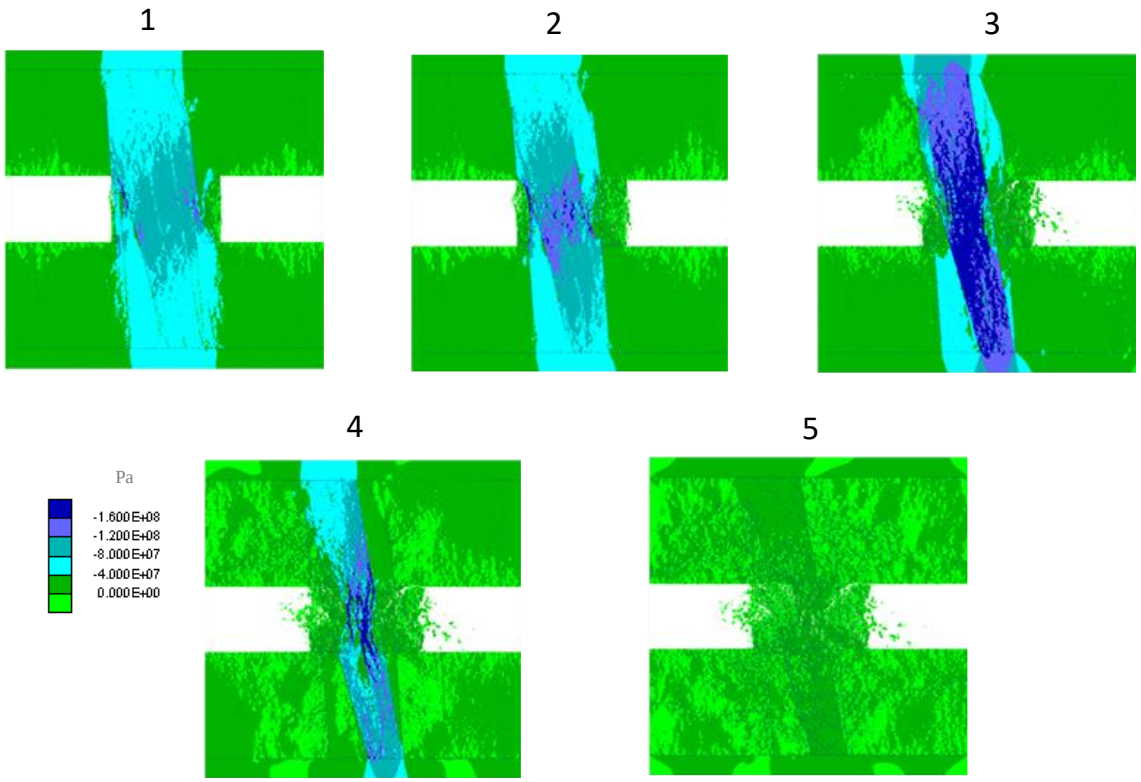


Figure 51: Progression of stresses for 4 m wide jointed pillar model for DFN 2

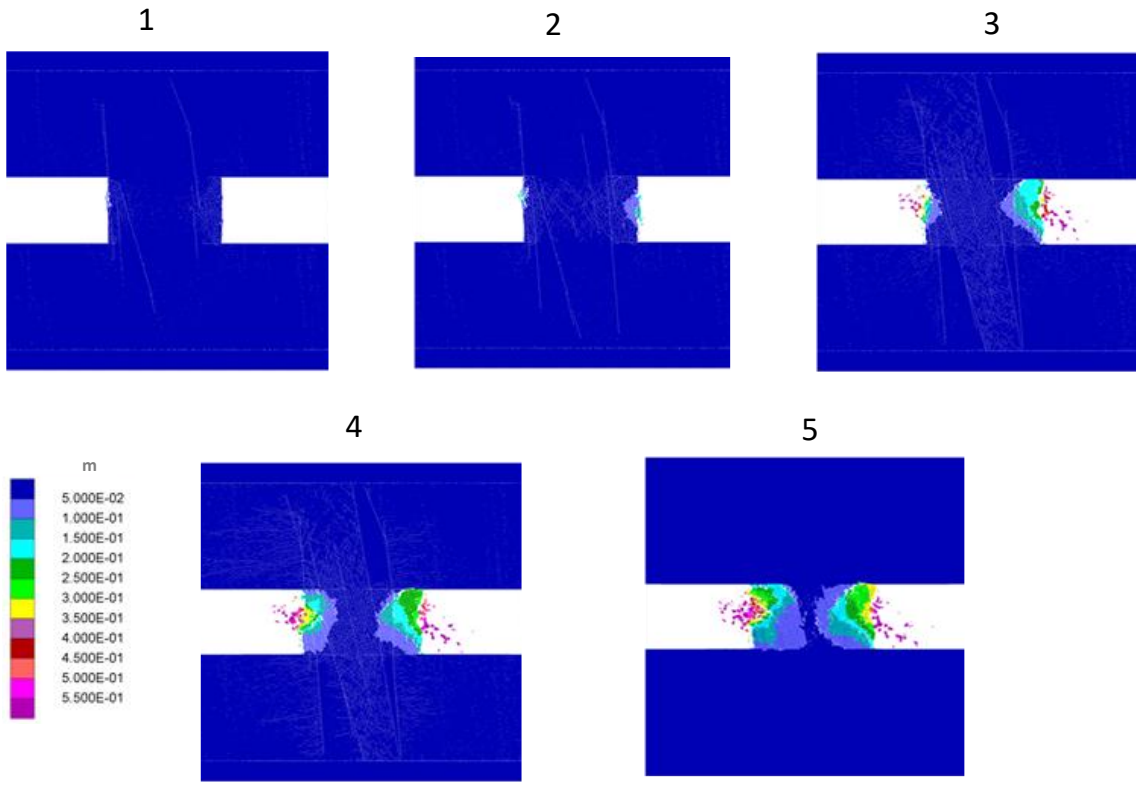


Figure 52: Progression of total displacement for 4 m wide jointed pillar model for DFN 2

Six meter pillars

The average pillar stress vs. displacement curve for a 6 m wide pillar with DFN 2 is presented in Figure 53. Fracturing within the pillar at the positions indicated on the curve is also presented. Figure 54 and Figure 55 show stress and total displacement contours, respectively.

The 6 m wide pillar has a peak strength in excess of 165 MPa. The pillar failure mechanism seems dominated by fractures, which resemble shear bands. Spalling also starts at a pillar strength of about 65 MPa. Due to the pillar width that provides relatively high confinement, the pillar strength does not drop and continues to rise up to a peak of about 170 MPa.

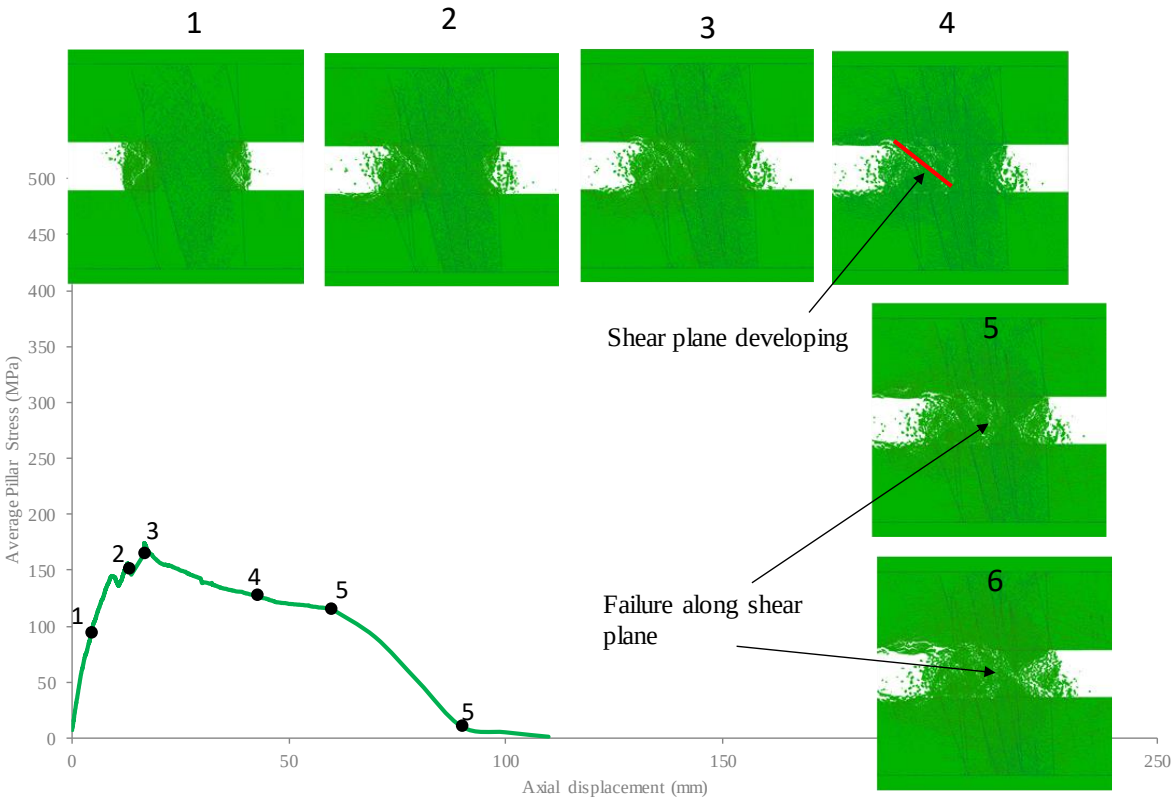


Figure 53: Average pillar stress versus axial displacement curve and associated failure mechanism for 6 m pillar for DFN 2

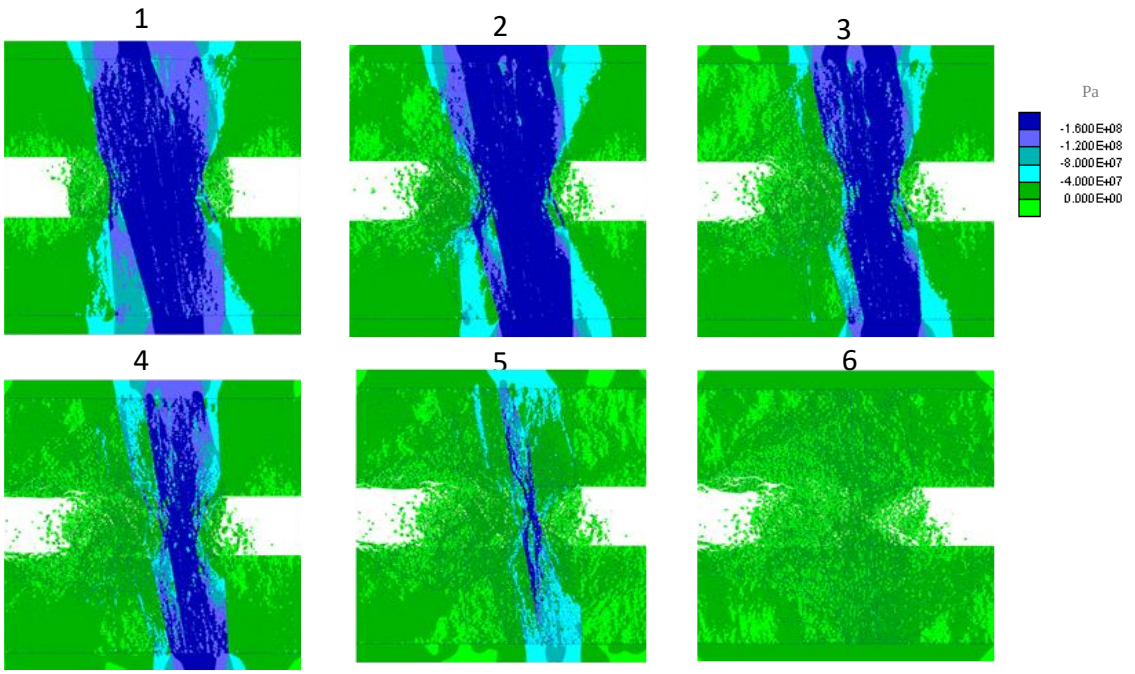


Figure 54: Progression of stresses for 6 m wide jointed pillar model for DFN 2

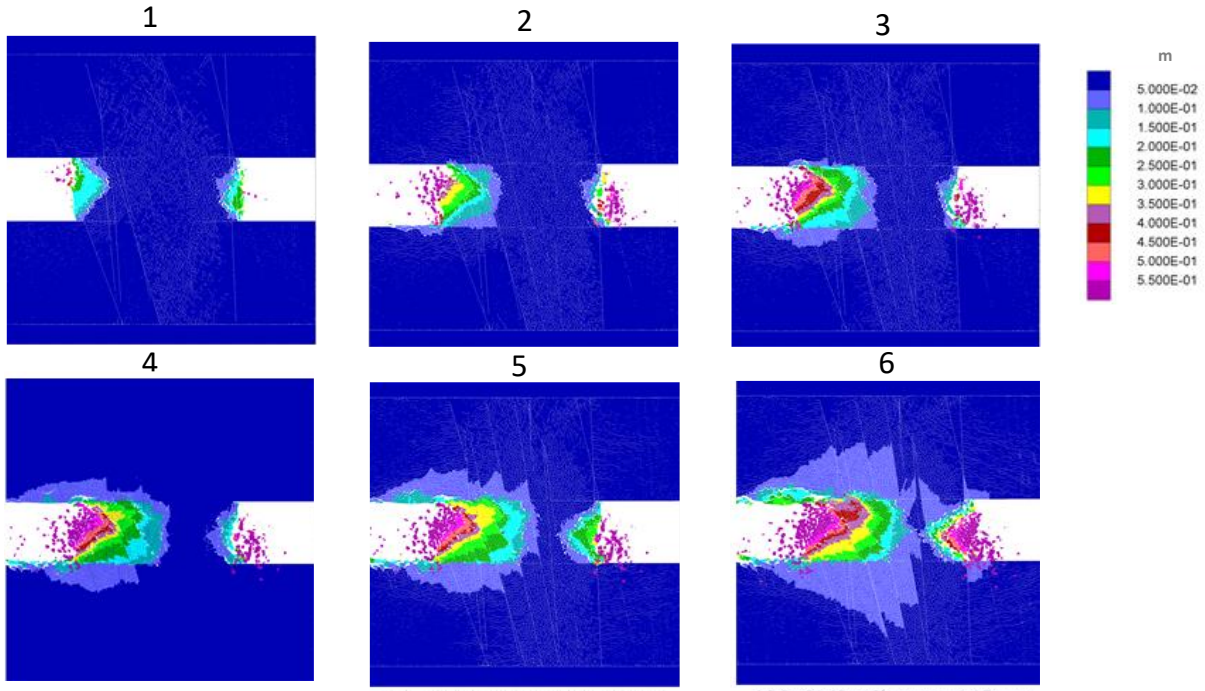


Figure 55: Progression of total displacement for 6 m wide jointed pillar model for DFN 2

4.2. Results analysis

The discussion of the results revolves around the following four fundamental questions:

- What effect does joints have on the pillar strength?
- What effect does pillar size have in a particular geotechnical domain (DFN); and
- What effect does shifting from one geotechnical domain to another (DFN 1 to DFN 2) have if the size of the pillars remains the same? It is important to remember that the difference between DFN 1 and DFN 2 is in that the former has low-angle joint, while the latter has only sub-vertical joint sets

Figure 56 shows the average pillar stress versus displacement curve for all the pillars with and without joints in the background for comparison.

The intact pillars show a very high peak strength. The presence of joints reduces the pillar strength by more than four times for each pillar size. The post peak behaviour of the 2 m pillar indicates strain hardening which is unexpected for a slender intact pillar. The average pillar stress versus displacement curve for the 6 m pillar only shows the pre peak behaviour as the model was stopped before the peak strength had been reached.

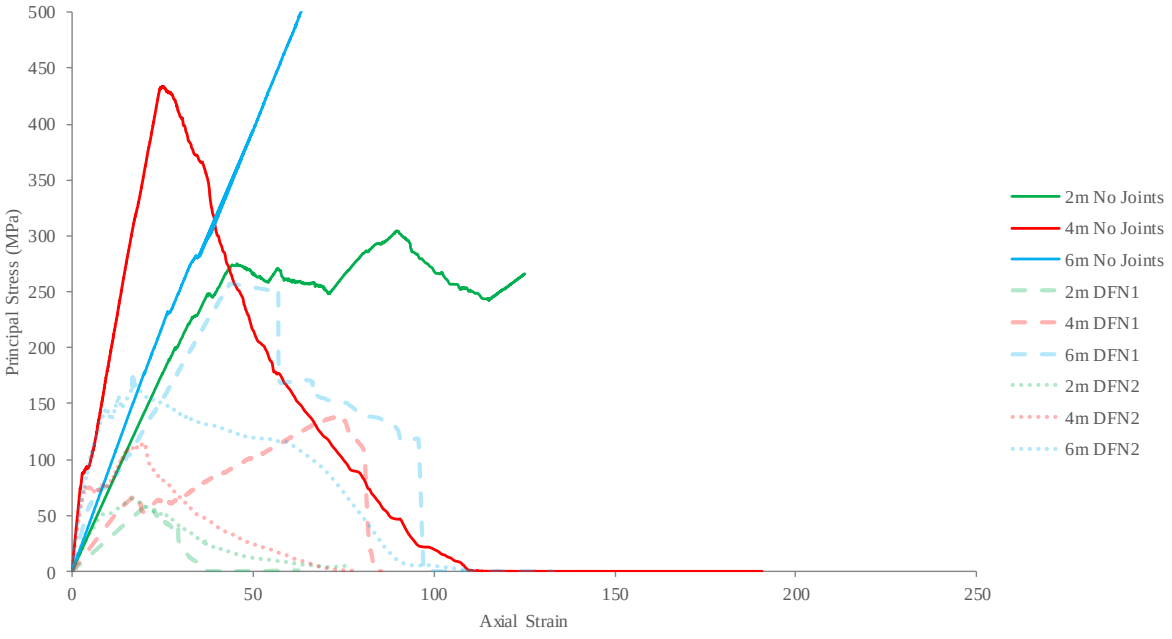


Figure 56: Average pillar stress versus axial displacement curve for intact pillars and jointed pillars results in the background

Figure 57 show the average pillar stress versus axial displacement curves for jointed pillar models, first in DFN 1 and in DFN 2. For ease of comparison, both results of DFN 1 and DFN 2 are represented together. DFN 1 results are highlighted while DFN2 results are greyed

out in the background. This representation helps draw a contrast between different pillar sizes and also different DFNs.

In DFN 1, increasing the pillar size results in an expected increase in peak pillar strength. The stiffness of the pillar also increases with the increase in pillar size. The shape of the entire post-peak stress displacement curve is different and the reason for this remains unknown.

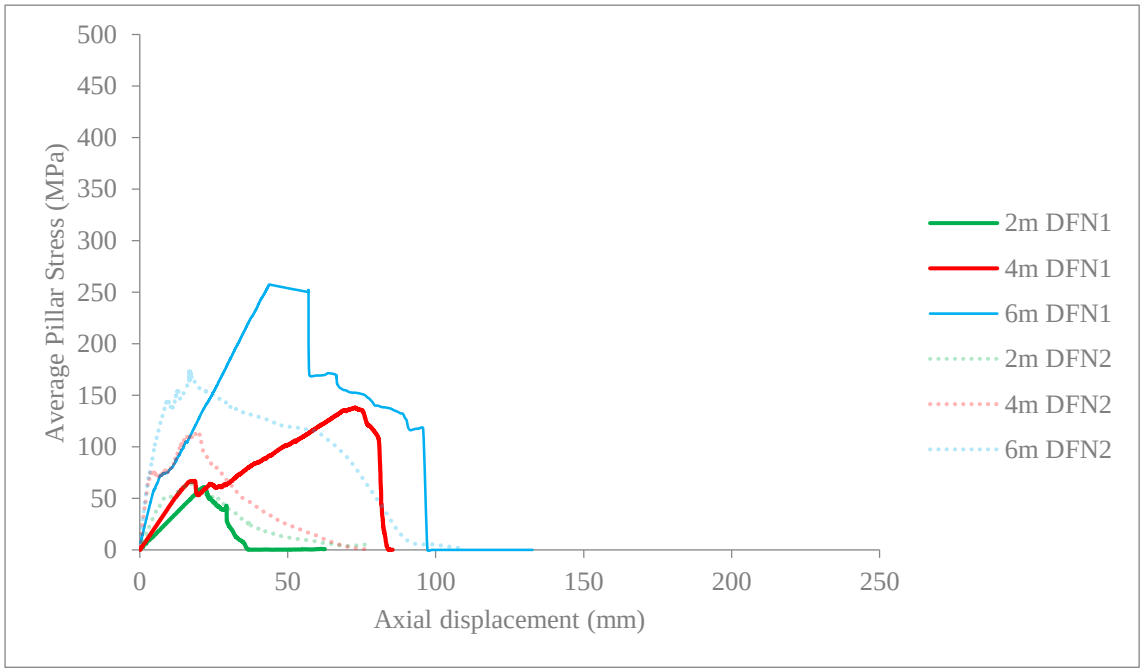


Figure 57: Average pillar stress versus axial displacement for DFN 1 and DFN 2 results in the background

In DFN 2, which is characterized by a simpler joint network comprising only sub-vertical joint sets, the response to increasing pillar size seems more intuitive. The slope of the pre-peak part of the average pillar stress versus axial displacement curves seems to be the similar for all pillar sizes. Expectedly, the pillar failure becomes less brittle and more ductile as the pillar size increases.

The 2 m wide pillars are expected to behave similarly in both geotechnical domains represented by DFN 1 and DFN 2.

When the friction angle of a joint is greater than the dip of the low angled joints, better performance is expected in the areas with low dipping joints as compared to the areas with just sub-vertical joints. The low lying joints are primarily dipping at about 5^{o} and have a

friction angle in the order of 20°. As expected, the 4 m pillars model show better performance in the areas where low angle joints are present.

For the 6 m pillars, the DFN 1 model yielded more and at a higher peak strength. Therefore, overall, it can be argued that a 6 m pillar is expected to perform better with the low angle joints.

Figure 58 shows the behaviour of a 2 m pillar in the DFN 1 and DFN 2 space.

The 2 m wide pillars are in general more brittle in the presence of low angle joints. Without the low angle joints, 2 m pillar models appear particularly ductile. All 2 m pillar models tend not to sustain a residual strength over a significant range of axial displacements

The high pillar stiffness observed especially in DFN 2 without low angle joints begs the question of whether the peak strength values recorded in these cases should be used for pillar design purposes. In fact, the hanging-wall will often deform to some extent and it is essential for the support system (pillars) to be sufficiently flexible not to snap. For this reason and the fact that the pillar residual strength values of the 2 m wide pillars is virtually nil, it is expected that such pillar size will not be utilized.

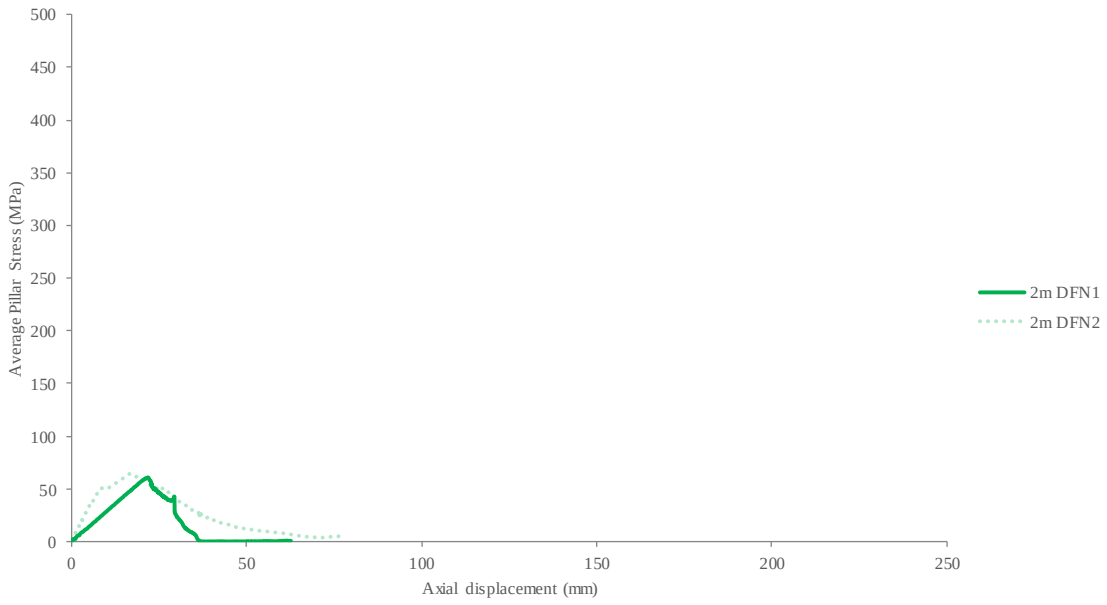


Figure 58: Pillar stress vs. axial displacement graphs of 2 m pillar models for DFN 1 with DFN 2 results in the background

The behaviour of a 4 m pillar in both geotechnical domains examined in this study is summarized in Figure 59. In DFN 1, there are low angle joints transecting the pillar, foot and hanging-walls. The 4 m model exhibits strain-hardening up to displacement of about 80 mm and then fails in a brittle manner.

Figure 59 shows how 4 m pillars behave with DFN 2 compared to DFN 1. In general, the modelled pillar with DFN 1 tend to be stiffer than those with DFN 2. Even though in both DFN 1 and DFN 2 the peak strengths are comparable, failure in simulation with DFN 1 is generally more brittle.

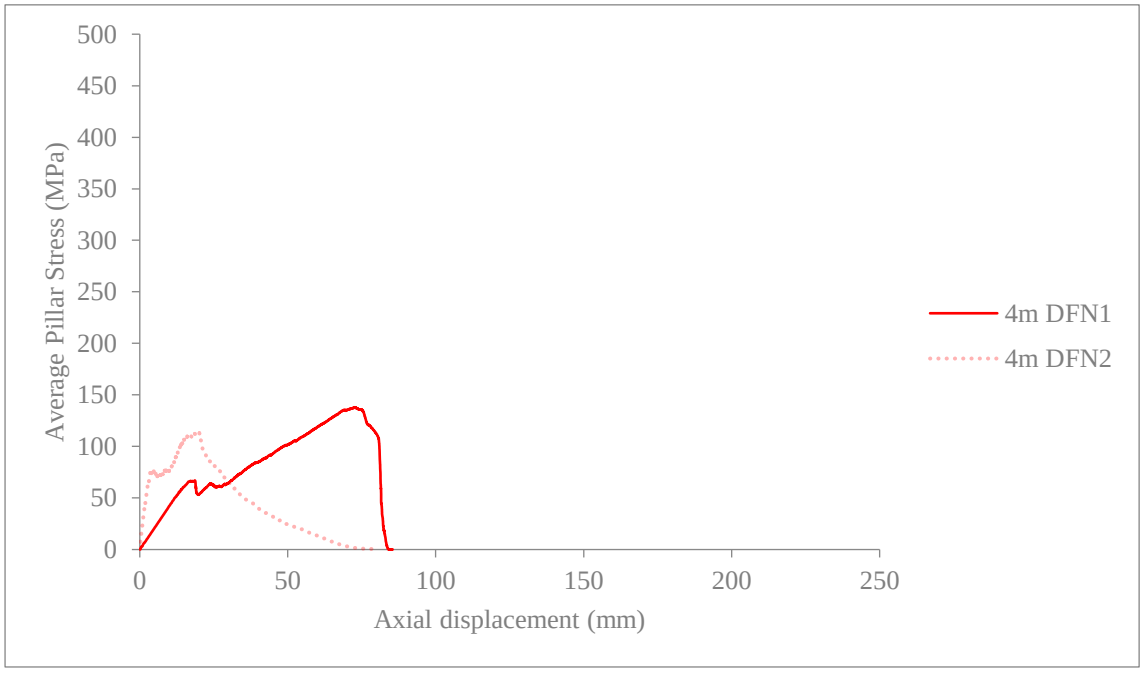


Figure 59: Pillar stress vs. axial displacement graphs of 4 m pillar models for DFN 1 with DFN 2 results in the background

Figure 60 shows the behaviour of 6 m modelled pillar in the DFN 1 geotechnical space. The responses of 6 m modelled pillars in DFN 2 are also represented for comparison.

The 6 m modelled pillar has a peak strength of about 270 MPa reached at a pillar closure of 40 mm. Beyond the peak strength, the pillar fails almost in the brittle manner.

Modelled pillars with DFN 2 tend to be stiffer in general than with DFN 1. This is primarily due to the absence of low angle joints. The peak strength for the pillar with DFN 2 is lower than that of the pillar with DFN 1 suggesting a significant effect of joint orientation on pillar strength as pillar size increases.

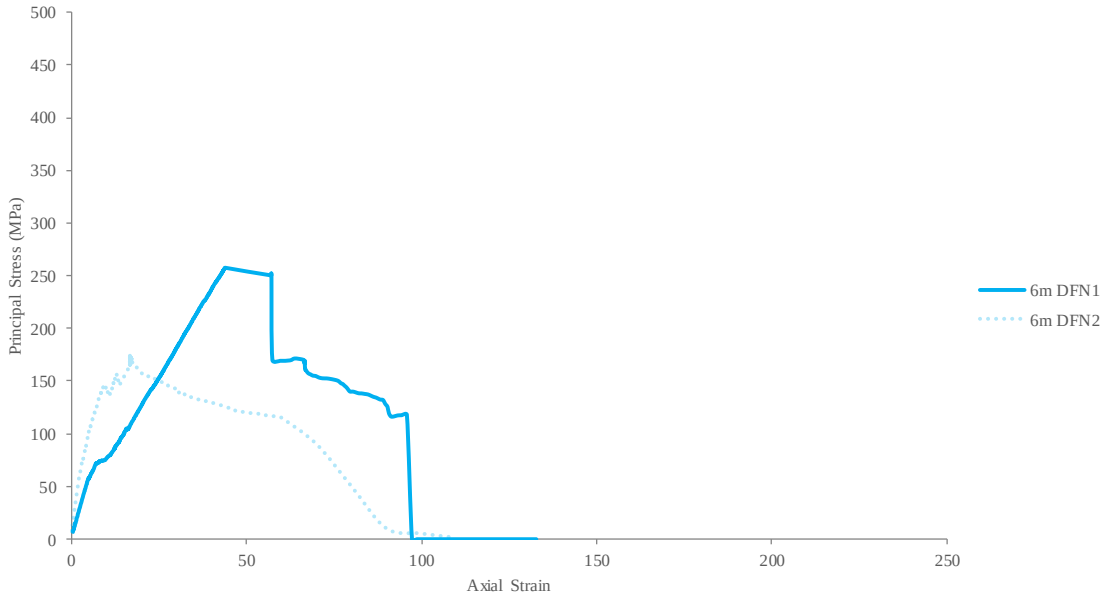


Figure 60: Pillar stress vs. axial displacement graphs of 6 m pillar model for DFN 1 with DFN 2 results in the background

4.3. Summary

Chapter 4 outlines the results obtained from the modelling process. For the purpose of understanding the effect of joints on pillars, both intact and jointed pillars were run. Two sets of jointed pillars with one set having jointing orientation representing the jointing network at different sections of the mine were studied. To understand the effect of size on pillar strength, each set was run with pillars of different widths (2 m, 4 m and 6 m) keeping the height constant.

Results obtained were analysed and there is a clear indication on the effect of joints on pillars. Pillar strength is affected by both pillar size and joint orientation. Conclusions and recommendations made following this analysis are outlined in Chapter 5.

Chapter 5: Conclusions and recommendations

The main objective of this project was to analyse the behaviour of hard rock jointed pillars in at Mine X Portal C. The Universal Discrete Element Code (UDEC) was selected to conduct the analysis as it allows for relatively large number of joints to be incorporated in the analysis, and also permits the simulation of tensile fracture development. Propagation of tensile fractures was found to be a key aspect of the pillar failure process in the model and in reality. Therefore, significant efforts have gone towards reproducing and calibrating this process based primarily on results of laboratory tests conducted on actual rock specimens collated at P_B.

The methodology proposed in this project to analyse hard rock jointed pillars using a discrete element method (DEM) combined with discrete fracture networks (DFN) has shown both its immense potential but also its limitations. Various parameters not directly related to the rock properties such as rounding and damping coefficient may yet affect the modelling results in different ways and since the technique is still being developed, there are limited guidelines for the selection of such parameters. Considerable efforts need to be made, possibly on a project to project basis, to understand the extent to which these parameters affect the modelling results and the failure mechanisms. The calibration of the model was then complex owing to the large number of unknowns.

Since average pillar stress was calculated as the average of the zones along the pillar centre line, there is a possibility of trapped zones registering high stress even after the pillar has been completely destroyed. This may explain the apparent yielding behaviour of the intact 2 m pillar in Figure 30 to Figure 33. Summing the reactions at the model boundaries where the displacement or velocity constraints are applied and dividing by the loaded area (length in 2D) is an alternative approach can be investigated.

The joint material properties were obtained from a Barton-Bandis model using results from shear box tests on open joint specimens and joint description information from previous core logging exercises at P_B. The joint normal and shear stiffness remained the major unknowns.

The representation of joints in the modelled pillars was based on a DFN approach whereby structural data from mapping is used to create stochastic representations of the rock mass. Various joint configurations within the pillar can be generated and analysed with this

approach. Two DFNs were examined as part of this project. The first DFN was selected to represent areas with low angle joints as observed in some parts of P_B, whereas the second DFN was meant to represent areas with only the sub-vertical joint sets. For each DFN, three different pillar sizes of 2 m, 4 m and 6 m were examined.

It is also important to recognise that the analysis was two dimensional (2D) assuming plane strain boundary conditions. Under plane strain conditions, the pillar is considered infinitely long in the out-of-plane dimension, which is not the case in reality. A three dimensional analysis, not covered in this project, may reproduce more realistically the actual boundary conditions, however, at the expense of an increased complexity of the model behaviour. The effective width by Wagner (1980) was proposed as an upper bound of pillar widths pending a 3D analysis. According to Wagner's effective width, the 2 m, 4 m and 6 m infinitely long pillars correspond effectively to 4 m, 8 m and 12 m square pillars, respectively. It is to be noted, however, that Wagner's effective width was derived for coal pillars and may not apply to hard rock jointed pillars. An additional 3D analysis is then necessary to determine whether the minimum width used in the 2D models should directly be used in the design or the conversion into an effective width is required.

From the 2D modelling the following conclusions can be drawn:

The models reproduced satisfactorily the pillar behaviour and mechanisms observed underground such as:

- Tensile fracturing;
- Pillar bulging;
- Sliding on joints

Opening up of tensile fractures in the central region of the 4 m and 6 m pillars (width to height ratio =1.6 and 2.4 respectively) is coincident with failure and indicates that the peak strength has been exceeded. However, in the 2 m pillars (slender pillars width to height ratio=0.8), the peak strength is reached at the onset of sliding along the pre-existing joints. In this case, spalling on the pillar walls only occurs way after the peak strength has been largely exceeded. The load carrying capacity of 2 m wide pillars is lost as soon as movement on the joints commences.

A case of significant bulging walls coincident with peak strength was observed in a 6 m. Bulging wall is due to rotation of failed rock blocks awaiting to detach and fall out. Spalling elsewhere seems to involve rather delamination and removal of successive layers of rock from the pillar edge with minimum bulking.

The average pillar strengths for DFN 1 and DFN 2 are summarised in Table 14.

Table 14: The average pillar strengths for DFN 1 and DFN 2 relative to the intact pillar

Pillar (minimum width/effective width)	2m/4m	4m/8m	6m/12m
Pillar strength (MPa)			
No Joints	270	450	750
DFN 1	55	130	265
DFN 2	65	110	170
Pillar strength ratio			
No Joints	100%	100%	100%
DFN 1	20%	29%	35%
DFN 2	24%	24%	23%

In all cases the pillar strength increases with increasing pillar width.

The pillar strength of 2 m wide pillar (4 m effective width) was found to be low considering the expected values from the theoretical calculations (see Section 2.2.3.). Pillars that small are not recommended.

In general, changing from DFN 1 to DFN 2 yields results substantially different in terms of pre- and post-peak behaviour. DFN 1, which is characterised by a low angle joint set in addition to the sub-vertical sets yielded a better pillar response overall. The contribution of the low angle joint sets translates into less stiff, more flexible and more ductile pillars.

The existence of joints reduces intact pillar strength by 70% to 80%.

Mine X is currently mining 4 m square pillars. According to the 2D numerical modelling carried out, these pillars are too small with strengths ranging between 55 MPa and 65 MPa. From the Hedley and Grant (1972) fomular used for the original pillar design, the mine is expecting pillars with average pillar strength of at least 95 MPa from the 4 m pillars. There is

need for revising the design criteria and to do a full 3D modelling to quantify the required pillar size.

Chapter 6 : References

Babcock, C. O., 1968. *Changes in breaking strength of model rock pillars resulting from end constraint,* s.l.: U.S. Bureau of Mines.

Barton, N., Lien, R. & Lunde, J., 1974. Engineering classification of rock masses for the design of tunnel support. *Rock Mechanics and Rock Engineering,* pp. 189-236.

Bieniawski, Z. T., 1989. *Engineering rock mass classifications: a complete manual.* New york, John Wiley & Sons.

Bieniawski, Z. T. & Van Heerden, W. L., 1975. The significance of in situ tests on large rock specimens.. *International Journal of Rock Mechanics and Mining Sciences,* Volume 12, pp. 101-113.

Brady, H. & Brown, E., 2004. *Rock Mechanics.* New York: Kluwer Academic Publishers.

Elmo, D., 2006. *Evaluation of a hybrid FEM/DEM approach for determination of rock mass strength using a combination of discontinuity mapping and fracture mechanics modelling, with particular emphasis on modelling of jointed pillars,* Exeter: University of Exeter.

Esterhuizen, G. S., 1998. *The effect of structural discontinuities on coal pillar strength as a basis for improving safety in the design of coal pillar systems,* Pretoria: Council for Scientific and Industrial Research.

Esterhuizen, G. S., 2000. *Jointing effects on pillar strength.* Morgantown, West Virginia University.

Esterhuizen, G. S., 2014. Extending empirical evidence through numerical modelling in rock engineering design. *Journal of the Southern African Institute of Mining and Metallurgy,* 114(10), pp. 755-764.

Esterhuizen, G. S., Dolinar, D. R. & Ellenberger, J. L., 2011. Pillar strength in underground stone mines in the United States.. *International Journal of Rock Mechanics and Mining Sciences,* Volume 48, pp. 42-50.

Gao, F., 2013. *Simulation of Failure Mechanisms around Underground Coal Mine Openings Using Discrete Element Modelling,* Vancouver: Simon Fraser University.

Ghazvinian, E., Diederichs, M. & Quey, R., 2014. 3D random voronoi grain-based models for simulation of brittle rock damage and fabric-duided micro-fracturing. *Journal of Rock Mechanics and Geotechnical Engineering,* pp. 506-521.

Hedley, D. G. & Grant, F., 1972. Stope and pillar design for the Elliot lake uranium mines. *The Canadian Mining and Metallurgical,* pp. 37-44.

Hoek, E., 2012. Evolution of the Hoek_Brown criterion and the associated Geological Strength Index (GSI) Evolution of HB criterion and GSI classification. *Second draft*, pp. 1-52.

Hoek, E. & Brown, T., 1980. *Underground Excavations in Rock.* 1st ed. London: The Institution of Mining and Metallurgy.

Hoek, E., Corkum, B. & Carranza-Torres, C., 2002. *Hoek-Brown Failure Criterion-2002 Edition.* s.l.:NARMS.

Itasca Consulting Group, Inc., 2006. *FLAC Fast Lagrangian Analysis of Continua User's Guide.* Minneapolis, Minnesota: Itasca Consulting Group, Inc..

Itasca Consulting, 2014. *UDEC User's manual,* s.l.: Itasca Consulting International.

Itasca Consulting, 2015. *3DEC User's manual - Discrete Fracture Networks in 3DEC.* s.l.:Itasca Consulting International.

Itasca Inc, 2014. *Universal Distinct Element Code (UDEC v6.0).* Minnesota, USA: Itasca Consulting Group.

Kazerani, T. & Zhao, J., 2010. Micromechanical parameters in bonded particle method for modelling of brittle material failure. *International Journal for Numerical and Analytical Methods of Geomechanics,* Issue 34, pp. 1877-1895.

Laubscher, D., 1990. A Geomechanics classification system for the rating of rock mass in mine design. *J.S Afr. Inst. Min Metall,* 90(86), pp. 257-273.

Lunder, P. J., 1994. *Hard rock pillar strength estimation an applied empirical approach,* Vancouver: University of British Columbia.

Lunder, P. J. & Pakalnis, R. C., 1997. Determination of the strength of hard-rock mine pillars. *Rock mechanics bulletin,* September, pp. 51-55.

Malan, D. F. & Napier, J. A., 2011. The design of stable pillars in the Bushveld Complex mines: a problem solved?. *The Journal of The Southern African Institute of Mining and Metallurgy,* Volume 111, pp. 821-836.

Martin, C. & Maybee, W. G., 2000. The strength of hard-rock pillars. *International Journal of Rock Mechanics & Mining Sciences,* pp. 1239-1246.

Mathey, M., 2015. *Investigation into the mechanism of strength and failure in squat coal pillars in South Africa,* Johannesburg: University of Witwatersrand.

Mine X, 2016. *Mine X Portal C Geotechnical report,* s.l.: s.n.

Portvin , Y. & Hadjigeorgiou, J., 2001. The stability graph method for open-stope design. *Underground mining methods: Engineering fundamentals and international case studies,* pp. 513-520.

Potvin, Y., Hudyma, M. R. & Miller, H. D. S., 1989. Design guidelines for open stope support. *Canadian Mining and Metallurgical Bulletin,* pp. 53-62.

Potyondy, D. O. & Cundall, P. A., 2004. A bonded-particle model for rock. *International Journal of Rock Mechanics & Mining Sciences,* Issue 41, pp. 1329-1364.

Preston, R. P., 2014. *Application of Photogrammetry to Estimates of Mine Pillar Damage and Strength,* Vancouver, Canada: Simon FRraser University.

Raffaldi, J. M., 2015. *Static and Dynamic Discrete Element Modelling of Slender Coal Pillars,* kentucky, USA: University of Kentucky.

Roberts, D. P., Roberts, M. K. C., Jager, A. J. & Coetzer, S., 2005. The determination of the residual strength of hard rock crush pillars with a width-to-height ratio of 2:1. *The Journal of The South African Institute of Mining and Metallurgy,* Volume 105, pp. 401-408.

Roberts, D. P., Yanske, T. R. & Lane, W. L., 1998. *Pillar extraction at the Doe Run company.* Victoria, s.n., pp. 223-227.

Salamon, M. D. & Munro, A. H., 1967. A study of the strength of coal pillars. *Journal of the South African Institute of Mining and Metallurgy,* pp. 55-67.

SRK Report No. 480443, 2015. *Mine X Portal B - Geotechnical Logging Report,* Johannesburg: SRK Consulting.

SRK Report No. 482668, 2014. *Site visit report - Mine X (Portal B).* Johannesburg: SRK Consulting.

Swart, A. H., Human, J. L. & Harvey, F., 2005. Rock engineering challenges. *The Journal of The South African Institute of Mining and Metallurgy*, pp. 103-106.

Wagner, H., 1980. Pillar design in coal mines. *Journal of the South African Institute of Mining and Metallurgy*, pp. 37-45.

Zhang, Y., 2014. *Modelling hard rock pillars using a synthetic rock mass approach,* Burnaby: Simon Fraser University.